University of Southampton

Faculty of Engineering and Physical Science

School of Chemistry

---

# Generation of XUV Photons and their Application in Time-Resolved Photoelectron Spectroscopy

---

*A thesis for the degree of*

*Doctor of Philosophy*

**Briony Ruth Downes-Ward**

July 2021

University of Southampton

Abstract

Faculty of Engineering and Physical Science

School of Chemistry

Doctor of Philosophy

**Generation of XUV Photons and their Application in Time-Resolved Photoelectron Spectroscopy**

by Briony Ruth Downes-Ward

To study chemical dynamics of isolated molecules in the gas phase we have used time-resolved photoelectron spectroscopy (TRPES). In the work reported in this thesis we have used both a UV and extreme ultra-violet (XUV) probe to study the photodissociation dynamics of methyl-iodide across the A-band. The thesis also discusses the work carried out to develop a semi-infinite gas cell (SIGC) for the generation of the XUV probe by high harmonic generation (HHG).

We performed two TRPES experiments on the A-band of methyl iodide, the first experiment excited using either 269 nm or 255 nm and ionised with a multiphoton probe, the second experiment used four pump wavelengths (279 nm, 269 nm 254 nm and 243 nm) and then ionised using a single XUV probe. The states that make up the A-band of methyl iodide are strongly dissociative in character. In both experiments we observe signal that is consistent with a rapid dissociation at all wavelengths except 254/255 nm. At 254/255 nm we observed surprisingly different dynamics with an extended lifetime and a second feature appearing in the photoelectron spectrum at a delay of around 100 fs associated with a shift in the photoelectron peaks to lower binding energies. The cause of the extended lifetime and more complex dynamics is unclear. We suggest the dynamics may be due to increased excitation onto the $^1Q_1$ state or vibrational excitation but the cause of the observation is still uncertain.

To generate a XUV probe for the TRPES experiments we use HHG from argon gas. The possible use of a SIGC was investigated to try and increase the photon flux of the harmonic closest to $\sim$ 20 eV. The effect of focus position, cell pressure and laser power was investigated.

# Contents

# List of Figures

# List of Tables

# Declaration of Authorship

I declare that this thesis and the work presented in it is my own and has been generated by me as the result of my own original research.
I confirm that:

1. This work was done wholly or mainly while in candidature for a research degree at this University;

2. Where any part of this thesis has previously been submitted for a degree or any other qualification at this University or any other institution, this has been clearly stated;

3. Where I have consulted the published work of others, this is always clearly attributed;

4. Where I have quoted from the work of others, the source is always given. With the exception of such quotations, this thesis is entirely my own work;

5. I have acknowledged all main sources of help;

6. Where the thesis is based on work done by myself jointly with others, I have made clear exactly what was done by others and what I have contributed myself;

7. Parts of this work have been published as:
   Emily M. Warne, Briony Downes-Ward, Joanne Woodhouse, Michael A. Parkes, Darren Bellshaw, Emma Springate, Paulina Majchrzak, Yu Zhang, Gabriel Karras, Adam S. Wyatt, Richard T. Chapman, Adam Kirrander and Russell S. Minns, *Photodissociation dynamics of $CH_3I$ probed via multiphoton ionisation photoelectron spectroscopy*, Physical Chemistry Chemical Physics, 21, 11142 (2019).
   Emily M. Warne, Briony Downes-Ward, Joanne Woodhouse, Michael A. Parkes, Emma Springate, Philip A. J. Pearcy, Yu Zhang, Gabriel Karras, Adam S. Wyatt, Richard T. Chapman and Russell S. Minns, *Photodissociation dynamics of methyl*

*iodide probed using femtosecond extreme ultraviolet photoelectron spectroscopy*, Physical Chemistry Chemical Physics, 22, 25695 (2020).

Briony Downes-Ward, Emily M. Warne, Joanne Woodhouse, Michael A. Parkes, Emma Springate, Philip A. J. Pearcy, Yu Zhang, Gabriel Karras, Adam S. Wyatt, Richard T. Chapman and Russell S. Minns, *Photodissociation dynamics of methyl iodide across the A-band probed by femtosecond extreme ultraviolet photoelectron spectroscopy*, Journal of Physics B, in press.

Signed:..... Date:.....

# Acknowledgments

I am incredibly indebted to my supervisor Russell Minns for always encouraging me and answering any of my questions, I could not have asked for a better supervisor. Thank you to the rest of the group: To Emily Warne for all her help and friendship, it has been a joy to do my PhD alongside you. To Jo Woodhouse, thank you for all your knowledge and help. To Ned Plackett and Ronnie Razmus for always being an extra body when I need you and for reading many drafts.

Thanks also must go to Bill Brocklesby and Jeremy Frey for all the useful ideas and conversations and their groups for help in labs and office and for making work an enjoyable place to be. I also wish to thank all the support staff particular Nick Gilbert who always seem to have the right tool to fix whatever problem I had.

Outside work I want to thank all the people who meant I had a work-life balance. To my housemate who kept me sane through thesis writing when we couldn't see anyone else. To my church family, particular my bible study group for all the ways you have shown and taught my Christ's love over the past few years. To all my caving friends, thank you for the wonderful community you are and for always being willing to follow me down some grotty hole and to forget all the troubles of the world above.

Although a PhD is only 4 years it also the work of many more years of education, thank you to every teacher and lecture who took their time to share their knowledge and joy with me. Thank you to my family for being there every step of the way, for constantly encouraging me.

# Chapter 1

# Introduction

Many chemical phenomena happen on very short timescales, such as molecular vibrations, and bond breakages. These processes are at the heart of chemistry and any first principle description of reactions will rely on a detailed understanding of these sub-picosecond processes[1, 2, 3]. A detailed understanding of chemical dynamics is important for many areas of chemistry. For example a detailed understanding of photostability is important for any chemical which needs to be exposed to the sun, such as chemicals used in agriculture[4, 5] or sun cream[6, 7]. While understanding the processes that lead to different products is important to help increase the useful product yield. Ideally, we want to watch these ultrafast chemical dynamics happening in real-time to observe the dynamic directly and reduce the need to extrapolate data from frequency-resolved measurements as these extrapolation will always rely on untested theoretical models. Frequency-resolved measurements can provide structural and electronic information about the starting and/or end molecules however are not able to observe any of the dynamics[8, 9, 10]. Ideally we want time-resolved measurements that are able to observe the full dynamics as in this case there is no extrapolation and we can be certain we are not missing unexpected dynamics. Unfortunately many time-resolved experiments are only able to observe some of the chemical dynamics, however this does still reduce the amount of extrapolation required and allows for some tests of theoretical

models[11, 12, 13]. Before short pulse lasers, time-resolved measurements were very difficult and often these phenomena were observed indirectly, for example measuring product formation to determine effects of conical intersection [14] or measuring accurate frequency to investigate vibrational energy redistribution [15, 16].

With the development of lasers that can generate pulses of shorter duration than the chemical phenomena being studied, the ability to measure spectroscopic changes on a sub-picosecond timescale became possible, allowing for a better understanding of the reaction process[17, 18, 19]. Many time-resolved experiment use a methodology known as pump-probe spectroscopy. A pump laser initiates some dynamics, the chemical system then evolves in time which is studied using a probe. The changing response to the probe provides information about the chemical dynamics present. The probe results in an observable which is measured and changes in the observable provide information on how the chemical system is evolving. A number of different time-resolved techniques have been developed using different probes and observables. Each technique provides a valuable tool in understanding molecular dynamics and provides a range of information such as the energy of the electrons[20, 21, 12] or nuclear arrangement[22, 23, 24] which can be combined to create a more complete picture. Some examples of observables that are measured include absorption spectra which provides information on the electronic/vibrational/rotational levels, depending on the probe wavelength [20, 25, 21] and fluorescence which predominately provides information about electronic levels but high resolution experiments can also provide information on vibrational and rotational levels [21, 26, 27]. If the probe wavelength is in the ultraviolet-visible (UV-Vis) region it will probe the electron levels of a molecule. A longer infra-red (IR) probe will provide information on the vibrational level. While microwave probes are used to investigate the rotational levels. The previous observables mentioned are spectroscopic and provide information on the energy of the electrons in the molecule. To study the positions of atoms in molecules diffraction patterns of electrons [23, 28, 29] or X-rays [24, 18, 30]

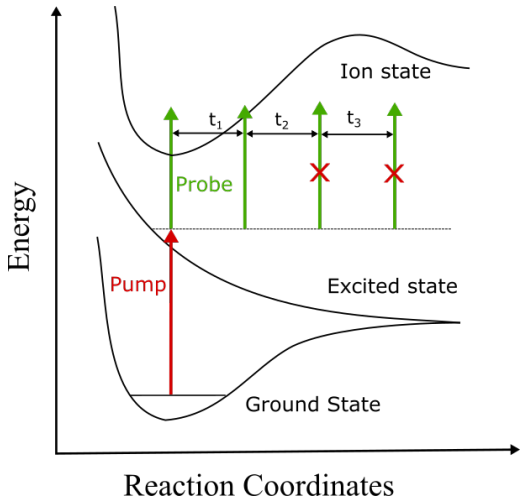


**Figure 1.1:** Schematic representing a TRPES. The pump electronically excites the molecule, then a probe laser ionises the molecule. $t_1$ and $t_2$ represents the changing in the time delay of the probe laser. After $t_1$ the probe does not have enough energy to ionise the molecule.

are useful observables to provide information on the positions of atoms in molecules.

In the experiments described in this thesis we have used a laser pulse to ionise molecules in time-resolve photoelectron spectroscopy experiments (TRPES). An example of a TRPES excitation and ionisation scheme is shown in figure 1.1. The molecule is excited from the ground state on to an electronic excited state by a pump laser, indicated by the red arrow. The molecule is then ionised by the probe laser onto the lowest lying cation state, indicated by the green arrow. At time zero, when the pump and probe arrive at the same time there is enough energy to ionise. After a time delay, $t_1$, the molecule has started to dissociate along the reaction coordinate, however there is still enough energy to ionise the molecule. After another time delay $t_2$ there is no longer enough energy to ionise the molecule and it is not possible to observe the molecules dynamics anymore. In TRPES the observable is the kinetic energies of the liberated electrons which allows the energy of the electrons before ionisation to be determined providing information about the evolution of the electronic and vibrational states.

The remainder of the thesis is organised as follows. The remainder of this chapter dis-

cusses the underlining theory used to guide our interpretation of TRPES, while chapter 2 provides a discussion of the experimental tools used to carry out XUV TRPES experiments. Chapter 3 describes experiments to optimise our high harmonic generation (HHG) source for 21 eV using a semi-infinite gas cell. Chapters 4 and 5 then compare the experimental results obtained from TRPES on $CH_3I$ using a multiphoton ionisation probe (Chapter 4) in a photoelectron imaging experiment and using an XUV probe (Chapter 5) in a photoelectron spectroscopy experiment. In chapter 6 the key results from this thesis are summarised.

## 1.1 Chemical Dynamics

### 1.1.1 Born-Oppenheimer Approximation

To understand how molecules evolve in time, calculated potential energy surfaces are useful and provide a helpful framework for interpreting experimental results. The potential energy surface of an isolated molecule can be perfectly described by the Schrödinger equation,

$$\left[\hat{T}_N + \hat{T}_e + \hat{V}\right] \Psi^{total} = E\Psi^{total} \tag{1.1}$$

where $\hat{T_N}$ and $\hat{T_e}$ are the kinetic energy operators for the nucleus and electrons respectively. $V$ is the potential energy of all the particles, $\Psi^{total}$ is the wavefunction of the whole system and $E$ is the energy of the system. Unfortunately, beyond simple two-body problems, this is impossible to solve exactly. Therefore approximations are used to extract useful information. The first approximation that is usually applied is the Born-Oppenheimer/adiabatic approximation. Since the mass of an atom's nucleus is significantly larger than the mass of the electrons, the electrons move a lot faster than the nucleus, therefore, it is possible to consider the electron instantaneously rearranging to changes in nuclear configurations. This means the wavefunction can be split into an electronic ($\Psi^e$) and nuclear component ($\Psi^N$) such that $\Psi^{total} = \Psi^N\Psi^e$. This

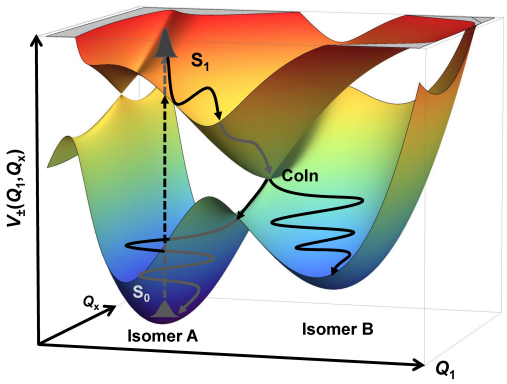


**Figure 1.2:** Two hypothetical 2D potential energy surfaces of a molecule with a conical intersection (CoIn). $Q_1$ and $Q_x$ indicate the two coordinates of the molecule, these are often a bond length or bond angle. The figure shows two potential energy surfaces, the ground state labeled with $S_0$ and an excited state $S_1$. The black dashed line represents an excitation from the global minimum to the excited state ($S_1$). The solid black line represents a possible trajectory of the molecule following excitation to the CoIn and then two possible trajectories from the CoIn to either the global minimum (isomer A) or a local minimum (isomer B). Figure reproduced from [31] with permission.

results in different eigenvalues at each nuclear configuration, producing the adiabatic potential energy surfaces such as the one shown in figure 1.2. Figure 1.2 shows two potential energy surfaces, the ground state ($S_0$) and the first excited state ($S_1$). At each coordinate($Q_1$,$Q_x$) an approximation of the Schrödinger equation is solved to give the potential energy $V$ to create the three dimensional potential energy surface. These potential energy surfaces show the location of global and local minimums. They also show the forces acting on the molecule at different geometries, given by the gradient of the potential energy surfaces. In this example we see two ground state isomers, A and B. These surfaces are useful for interpreting TRPES experiments as they provide information on the geometry of the molecule when excited and the subsequent dynamics as the force on the molecule is given by the gradient of the surface. The dynamics of the molecule on the potential energy surface are described in more detail in later sections.

### 1.1.2 Franck-Condon Principle

The first step of TRPES usually involves the excitation of a wavepacket onto higher lying potential energy surfaces. How the wavepacket is projected onto the higher state is governed by selection rules and the Franck-Condon factor. The Franck-Condon principle relies on the Born-Oppenheimer approximation, which allows separation of nuclear and electronic wavefunctions. The probability $P$, of an electronic transition between the initial state ($\psi$) and the final state ($\psi'$) is given by

$$P = |\langle \psi' | \boldsymbol{\mu} | \psi \rangle|^2 \tag{1.2}$$

where $\boldsymbol{\mu}$ is the dipole operator. For this to be non-zero the overall symmetry of the wavefunctions and dipole operator must be totally symmetric. In the case where there is a change in both the electronic and vibrational states, the dipole operator is given by,

$$\boldsymbol{\mu} = \boldsymbol{\mu_e} + \boldsymbol{\mu_N}. \tag{1.3}$$

where $\boldsymbol{\mu_e}$ and $\boldsymbol{\mu_N}$ are the electronic and nuclear dipole moments respectively. The wavefunctions can be separated into electronic ($\psi_e$) and vibrational ($\psi_v$) wavefunction (ignoring rotations and spin) using the Born-Oppenheimer approximation which allows separation of nuclei and electrons motion to give,

$$P = |\langle \psi'_e \psi'_v | \boldsymbol{\mu} | \psi_e \psi_v \rangle|^2. \tag{1.4}$$

Inserting equation 1.3 for the dipole moment gives,

$$\langle \psi'_e \psi'_v | \boldsymbol{\mu} | \psi_e \psi_v \rangle = \langle \psi'_e | \boldsymbol{\mu_e} | \psi_e \rangle \langle \psi'_v | \psi_v \rangle + \langle \psi'_v | \boldsymbol{\mu_N} | \psi_v \rangle \langle \psi'_e | \psi_e \rangle. \tag{1.5}$$

The second term is zero as $\langle \psi'_e | \psi_e \rangle$ is zero, because electronic states are orthogonal, whereas the first term is non-zero as the vibrational states in different electronic states

are not orthogonal. This means the overall transition probability can be written as,

$$P = |\langle\psi'|\boldsymbol{\mu}|\psi\rangle|^2 = |\langle\psi'_e|\boldsymbol{\mu_e}|\psi_e\rangle\langle\psi'_v|\psi_v\rangle|^2. \tag{1.6}$$

The first integral gives the electronic selection rules; the probability of transition is only non-zero if the product of the initial and final electronic wavefunction and the dipole moment symmetry is totally symmetric. This means the transition has to be resonant, therefore the energy of the photon driving the transition has to be equal to the energy gap of the two states. The square of the second integral is the Franck-Condon factor. The larger the overlap between the initial and final states the more intense the transition is [32]. Therefore, the more similar the shape of the two electronic states are, the greater the overlap between the same vibration. If the excited electronic wavefunction has a similar shape to the initial wavefunction, transitions with $\Delta$V=0 will have the largest Franck-Condon factor. As the two electronic states are very close to identical, a number of vibrational states will have non-zero Franck-Condon factors and therefore if the light pulse driving the transition has a broad bandwidth a number of states will often be excited creating a superposition of eigenstates. This superposition is known as a wavepacket. The initial electronic ground state of an ensemble of molecules will have a number of different ro-vibrational states that are excited. The distribution of these states is governed by the Maxwell-Boltzmann distribution which is dependent on the temperature of the system. Which state is initially excited will be effect the wavepacket that is produced.

### 1.1.3 Wavepacket Dynamics on excitation.

The wavepacket will evolve in time. The evolution of the wavepacket is governed by the molecule's potential energy surfaces. To allow for calculations and models these energy surfaces are simplified to the adiabatic potential energy surfaces produced by the Born-Oppenheimer approximation.

The time-dependent Schrödinger equation is

$$i\hbar\frac{\partial|\psi(t)\rangle}{\partial t} = \hat{H}|\psi(t)\rangle \tag{1.7}$$

where $\hat{H}$ is the Hamiltonian. Therefore the time evolution of a wavepacket when differentiated with respect to $t$ must result in itself with a factor of $i\hbar$. This criterion is satisfied by the function

$$e^{iE_N t/\hbar}, \tag{1.8}$$

where $E_N$ is the energy eigenvalue and $t$ is time. This is the time/phase evolution of an eigenstate. This changes the phase of the wavefunction in the complex plane but has no effect on observables hence eigenstates are referred to as stationary states. However, for a superposition of states, the case is different as a different phase factor is required for each eigenstate. When exciting a molecule using a short pulse multiple eigenstates are excited due to the bandwidth of the laser pulse. A superposition of vibrational eigenstates can be written as,

$$|\Psi(t)\rangle = \sum_N A_N|\psi_N(t)\rangle e^{-iE_N t/\hbar}, \tag{1.9}$$

where $A_N$ is the amplitude of each molecular vibrational eigenstate. The different time evolution for each state results in interference between the eigenstates. Hence the wavepacket is not stationary but evolves as a function of time on the potential energy surface. Figure 1.3 shows an example of how a superposition evolves in a harmonic oscillator. The harmonic oscillator is a simplified model of the vibrations in a diatomic model, where there is only one dimension (bond length). The first panel shows the probability distribution function (red) of the electron at time zero of the superposition $\Psi = (\psi_0 + \psi_1)/\sqrt{2}$, where $\Psi_n$ is the vibrational eigenfunction with $n$ excitation. The harmonic potential is shown by the black curve. At time zero the probability is predominantly on the right corresponding to an extended bond. In the middle panel, at

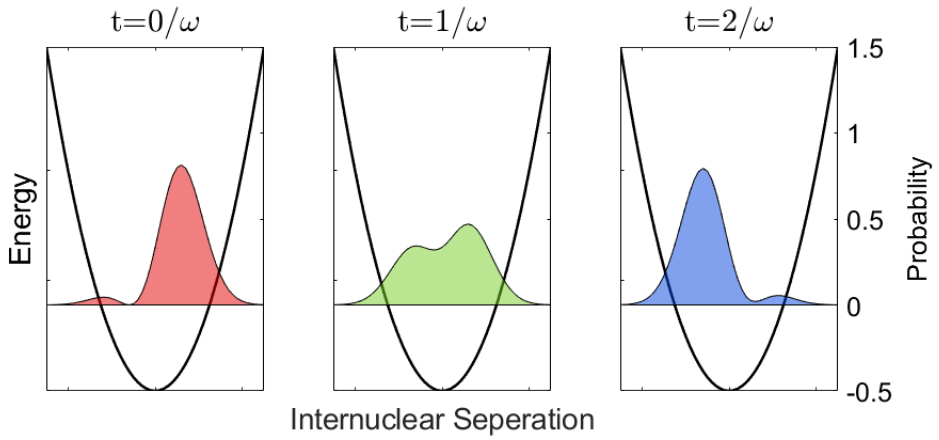


**Figure 1.3:** The calculated time evolution of probability distribution function for an electron in a superposition. The solid black line shows the harmonic potential of a diatomic molecule. The red probability curve shows the starting probability distribution at t=0 for a superposition of equal contribution from the first and second vibrational eigenstates of the harmonic oscillator potential shown. The green probability curve is the same superposition after time $1/\omega$ where $\omega$ is the natural frequency of the oscillator. And the blue probability curve shows the same superposition after $2/\omega$.

time=$1/\omega$, where $\omega$ is the natural frequency of the harmonic oscillator, the wavepacket has evolved and the probability (green) is more spread out and centred nearer the minimum of the potential energy curve. The right hand panel shows the probability curve (blue) at time $= 2/\omega$ which has evolved again and is predominantly at the left side of the potential energy curve corresponding to a short bond length. This is similar to a classical description of a molecular vibration, with the bond oscillating between a compressed and stretched bond. As more eigenstates are populated the wavepacket becomes more localised and behaviours more like a classical vibration.

As the number of atoms increases the number of dimensions increases leading to an increase of complexity of the potential energy surfaces. Often an intuitive idea of the behaviour of the wavepackets on the excited state potential energy curve is obtained by thinking of it as evolving classically, under Newtonian physics on a 1D or 2D surface. The number of dimensions for a non-linear molecule is given by $3N - 6$, meaning it is not possible to visualise the complete surfaces of most molecules and to include higher

dimensions computers are required.

Considering the potential energy surfaces in figure 1.2, we would expect excitation of isomer A on to the $S_1$ state (indicated by the dashed arrow) to result in the wavepacket moving toward higher $Q_1$ values as it "rolls" down the $S_1$ surface to the conical intersection (CoIn in the diagram). A conical intersection is a point in space where two different electronic states are degenerate allowing for the transfer of the wavepacket between the two electronic states. At the conical intersection we then expect some molecules to continue on their trajectories and relax to a local minimum at isomer B. While the other molecules will continue on the $S_1$ before rolling back and then passing through the conical intersection and relaxing back to the global minimum as isomer A.

### 1.1.4 Non-Adiabatic Dynamics

All the previous sections have assumed the Born-Oppenheimer approximation holds however, this breaks down when potential energy surface are close together allowing for more complex dynamics and transfer of population between the adiabatic potential energy surfaces. When two surfaces of the same symmetry approach they mix to produce two surfaces which are described as a superposition of the diabatic states. Diabatic states

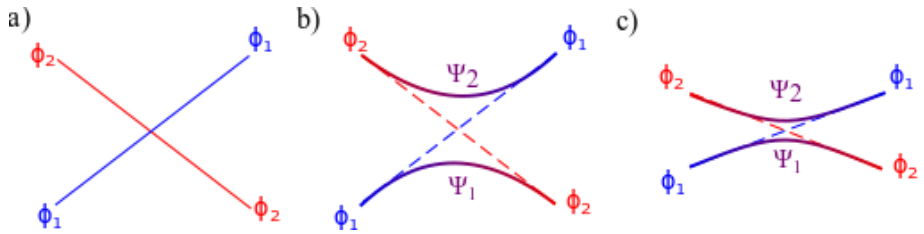


**Figure 1.4:** $\phi_1$ and $\phi_2$ are the two diabatic surfaces. $\Psi_1$ and $\Psi_2$ are adiabatic surfaces that result from the mixing of the diabatic surfaces such that $\Psi_1 = C_1\phi_1 + C_2\phi_2$ and $\Psi_2 = C_2\phi_1 + C_1\phi_2$ where $C_1$ and $C_2$ are fractions. a) No mixing of states is present due to spin and symmetry restrictions strictly forbidding transition between the states. b) Mixing between the diabatic states $\phi_1$ and $\phi_2$ indicated by the dashed line resulting the adiabatic surfaces $\Psi_1$ and $\Psi_2$. c) similar to b) but diabatic surfaces closer in gradient resulting in adiabatic surface deviating less from the diabatic surfaces

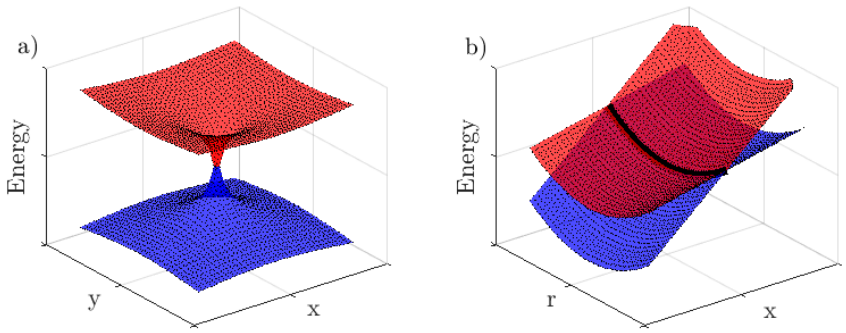


**Figure 1.5:** The conical intersection of two electronic surfaces viewed as a function of different coordinates. The red surface is the higher energy surface while the blue is the lower energy surface. a) Conical intersection view in branching coordinates x and y. b) Conical intersection view as a function of branching coordinate x and seam coordinate r. The seam is indicated by the black line, this is a line where the degeneracy of the two electronic states is retained.

have the same electronic structure/ character at all geometries. As shown in figure 1.4, $\Psi_1 = C_1(r)\phi_1 + C_2(r)\phi_2$ where the coefficients are geometry dependent. Far away from the crossing, the diabatic states $\phi_1$ and $\phi_2$ are a good description of the true adiabatic states $\Psi_1$ and $\Psi_2$. For two symmetric surfaces to be degenerate they must satisfy the secular determinant,

$$\begin{bmatrix} \hat{H}_{11} - E & \hat{H}_{12} \\ \hat{H}_{21} & \hat{H}_{22} - E \end{bmatrix} \begin{bmatrix} C_1 \\ C_2 \end{bmatrix} = 0 \tag{1.10}$$

This requires $\hat{H}_{11} = \hat{H}_{22}$ and $\hat{H}_{12} = \hat{H}_{21} = 0$ which can only be satisfied with two independent degrees of freedom. Therefore in diatomic molecules, this leads to the non-crossing rule, which states the potential energy surface of the same symmetry may not cross. In polyatomics, it is possible to satisfy the condition of degeneracy which leads to the potential energy surfaces crossing. The subspace where the degeneracy is lifted linearly is referred to as the branching spacing and conical intersection looks similar to that of figure 1.5 a) while in the other 3N-8 dimensions the conical intersection forms seams similar to that of figure 1.5 b). This is seam space which is orthogonal to the branching space [33].

Where potential energy surfaces of the same symmetry are close the Born-Oppenheimer approximation breaks down and the nuclear and electronic motion couple. This can be thought of as the time-dependent electric field from the nuclear vibrations driving transitions between electronic states. As the nuclear motion due to vibrations in a molecule is slow the frequency of the electric field oscillations are small and hence usually do not induce electric transition. The probability of a transition between states is given by,

$$P = exp\left(-\frac{\pi}{2\hbar}\frac{\Delta E^2}{\upsilon \Delta S}\right) \tag{1.11}$$

where $\Delta E$ is the energy separation between the two electronic states, $\upsilon$ is the velocity of the nuclear configuration along the reaction coordinate and $\Delta S$ is the gradient difference of the diabatic potentials. The smaller the gradient difference the closer the character of the diabatic states so the wavepacket is more likely to stay on the adiabatic state as shown in figure 1.4.

Avoided crossings and conical intersections provide a non-radiative transition to different electron states. Conical intersections are important in understanding chemical dynamics as they are geometry specific and are a route for photostability which is especially important in molecules of biological relevance[34].

### 1.1.5 Photoionisation

To investigate the time evolution of a wavepacket of the potential energy surface we use a photon to ionises the molecule. This means the wavepacket is projected on to the cation state after a time delay by a probe laser pulse. The resulting signal is given by,

$$\begin{aligned} S_f(t) &= |\langle \Psi_f | \boldsymbol{\epsilon}_{probe} \cdot \boldsymbol{\mu} \, |\Psi(t)\rangle|^2 \\ &= \left| \sum_N A_N \langle \Psi_f | \boldsymbol{\epsilon}_{probe} \cdot \boldsymbol{\mu} \, |\psi_N(t)\rangle e^{-iE_N t/\hbar} \right|^2 \end{aligned} \tag{1.12}$$

Where $\boldsymbol{\epsilon}_{probe}$ is the electric field of the probe laser and $\Psi_f$ is the final state which is consists of the final cation state ($\psi_c$) and the photoelectron ($\psi_{fe}$). Theses are assumed to be separable such that $\Psi_f = \psi_c\psi_{fe}$. All other terms have the same meaning as previously described. Again there will be a number of cation states with non-zero overlap and hence the wavepacket can be ionised into multiple final states.

The selection rules that govern absorption and fluorescence are relaxed in photoionisation due to the outgoing electron. As the out going electron carries symmetry, such that the transition dipole moment, from the neutral to the cationic state, $\langle\psi'_e|\boldsymbol{\mu}|\psi_e\rangle$, from equation 1.6, no longer has to be totally symmetric for the transition to be allowed.

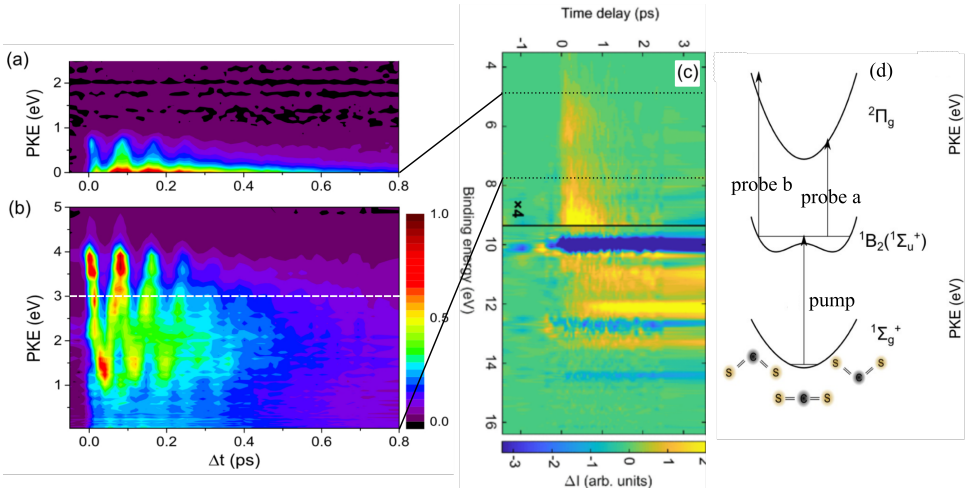


**Figure 1.6:** The time-resolved photoelectron spectra of $CS_2$ probed by three different probe energies following excitation by 200 nm. a) is ionisation by a 4.8 eV probe, b) a 7.8 eV probe and c) a 21.5 eV probe. a) and b) are plotted as a function of electron kinetic energy while c) as a function of binding energy. The dashed black lines on c) show the location of the zero electron kinetic energy in b) and c). While the dashed white line on b) is the location of zero kinetic energy for a). d) a schematic potential energy diagram of $CS_2$, probe a is the probe used for the spectrum in a) and probe b is the probe used for spectrum in b). Higher kinetic energy corresponds to lower binding energy. a), b) and d) are reproduced from [11] with permission from the Optical Society of America and c) is reproduced from [35] with permission from the American Physical Society.

### 1.1.6 Time-Resolved Photoelectron Spectroscopy

In time-resolved photoelectron spectroscopy (TRPES), the measured response is ionisation, the kinetic energy of photoelectrons are recorded as a function of pump-probe delay to produce time dependent photoelectron spectra. This thesis is focused on using TRPES to study isolated molecules. Initially the molecule is in a stationary ground state, it is then excited into a state which evolves with time. This state is then studied with the probe laser which ionises the molecule, projecting the state onto the cation potential energy surface. The majority of TRPES experiments to date have used a UV ($<$ 6 eV) probe. This limits the region in which the chemical dynamics can be studied as it is below the ionisation potential (IP) of many molecules as shown in figure 1.1, meaning the full chemical pathway can not be studied. Using higher energy photons increase this window, with photons around 20 eV it is possible to observe the full reaction dynamics, as 20 eV is above the IP of all atoms/molecules except helium. Helium has the largest IP at 24.6 eV, therefore will not be ionised meaning the molecule of interest can be seeded into helium gas. This means XUV photons can act as a universal probe as it is always possible to ionise meaning the molecule always has a response to the probe. Figure 1.6 shows three photoelectron spectra following excitation of $CS_2$ by a 200 nm pump with increasing probe wavelength to demonstrate the increased observation window with increasing probe wavelength. Excitation by 200 nm created a vibrational wavepacket on the $^1B_2$ state as shown in d) [11, 35]. In a) $CS_2$ is ionised by a 4.8 eV probe which means only part of the vibrational wavepacket dynamics can be observed as represented by the "probe a" arrow in d). It is only possible to ionise $CS_2$ in its linear geometry due to the low probe energy. In b) the probe energy is increased to 7.8 eV meaning it is possible to ionise $CS_2$ in its bent geometry as well as shown by the "probe b" arrow in d) allowing the full vibrational wavepacket to be observed. The previous experiment could only observe the dynamics above 3 eV kinetic energy as indicated by the white dashed line. In c) a 21.5 eV probe allows the full dissociation dynamics of $CS_2$ to be mapped along with

ionisation from other electronic states and the ground state depletion and the formation of the products. The previous two probes could only observe binding energy lower than 4.8 eV and 7.8 eV respectively. While the higher energy probe allows the full dynamics to be observed the oscillation at lower binding energy that were observed in the other two experiments are not observed. This is due to the difference in pulse length, the two lower energy probe experiments used sub-20 fs pulse while the XUV probe experiment measured the cross-correlation of the two pulses to be 180 fs, the lower time resolution means the oscillation can not be observed.

Although the 21.5 eV probe means the full reaction path of $CS_2$ can be mapped there are a number of disadvantages over the lower energy probe. The major disadvantage is low intensity of lab based source of XUV photons which along with the lower cross-section of absorption for the XUV photons results in a worse signal to noise ratio. Cross-section is a measurement of the probability that the molecule will absorb the photon. Another disadvantage is the large range of kinetic energy of the photoelectrons being collected often results in a lower energy resolution.

### 1.1.7 Advancement in Time-Resolved Photoelectron Spectroscopy

TRPES has been around for nearly 40 years [36, 37] and over that time there have been many advances to increase the versatility and amount of information which can be extracted about the ionisation process. A natural improvement is to also collect the ions by placing a time-of-flight spectrometer opposite the electron detector. This allows for the detection of the changes in ion yield and the kinetic energy of the fragments. If the laser intensity and/or gas pressure is lowered so that the probability of photoionisation is less than one per a laser pulse it is possible to disentangle the photoelectron spectra from different chemicals[38, 39]. This is known as photoelectron-photoion coincidence spectroscopy (PEPICO). This is particularly helpful when reactants and/or products have similar photoelectron spectra or when ionisation from different states results in differ-

ent fragmentation's [40, 41, 42]. An example of an experiment where PEPICO was important to understand the chemical dynamics is Maierhofer *et al.*[40] investigation of the relaxation channels following excitation of acetone. They were able to distinguish between two of the channels only due to the coincidence measurements as both channels contributed a parent ion and have the same time constant however one channel resulted in fragmentation after the ionising probe meaning it was also present in the daughter fragment photoelectron spectrum. It would not have been possible to separate the photoelectron spectra from the parent and daughter fragments without coincidence measurement. A major problem with PEPICO is the required low signal levels which results in a long collection time and requires high repetition rate lasers.

Another useful addition to TRPES is the ability to record the angular distribution the electrons are emitted at. Velocity map imaging (VMI) is a technique that produces an electric field that results in electrons of the same velocity being focused to the same position on a detector as described in section 2.3.3.2. This produces a photoelectron angular distribution (PAD), which provides information about the angular distribution of the emitted electrons. When used with a pump-probe measurement, VMI is known as time-resolved photoelectron imaging (TRPEI) This provides information on the orbital the electron was in before it was ionised. As the electrons are spread out over a detector, imaging also increases the collection time however it does not require less than one molecule per a pulse like PEPICO. It is also possible to combine this with fragments detection or PEPICO by imaging the electron, fragments or both. Photoelectron imaging and PEPICO have been combined to study the molecular dynamics in butadiene, with a 1KHz laser this required a collection time of about 100 hours[43]. TRPEI has been applied to study the rotational dynamics of molecules such as pyrazine [44] and $C_2^-$[45] as PADs are sensitive to any alignment caused by the pump laser it is possible to follow any induced rotation in the molecules. For example if there is some parallel alignment (to the probe laser) in the molecule ensemble a photoelectron feature due to a parallel

transition would be more intense as well as producing a more parallel PAD. After some time the molecules dephases and have some perpendicular alignment. In this situation the photoelectron feature would reduce in intensity and the PAD would be more perpendicular. The molecule will continue rotating and become parallel. An example of an experiment where TRPEI has been helpful in understanding the chemical dynamics is Lecointre *et al.*[46] study of the relaxation of the 7,7,8,8-tetracyanoquinodimethane (TCNQ) anion. In this experiment the photodetachment from the excited state and the ground state were isoenergetic so were not distinguishable in the photoelectron spectrum however as the symmetry of the two states was different it was possible to follow the relaxations from the excited state to the ground state using the changes in the angular distribution of the photoelectrons using PADS.

Another key area of advancement is the alignment of molecules before exciting and ionising them[47, 48]. Without molecular alignment, a lot of information is averaged out in the imaging techniques due to the random orientation of the gas molecules and the resulting images are in the lab frame. By aligning molecules using a non-resonant laser pulse before the experiment the measurement approaches the molecular frame and information about the effect of molecular alignment on the interaction with light is obtained. Figure 1.7 shows the PADs from $CS_2$ following excitation by 200 nm and ionisation by 256 nm for aligned (top) and unaligned (bottom) $CS_2$. $CS_2$ was aligned with a 805 nm nonresonant pulse 73.5 ps before the pump pulse. In the PADs from the alignment there is clear oscillations in the angular distribution. This is a result of the vibrational excitation. In the linear geometry the excited state has $\sigma^*$ geometry however when the molecule bends this state mixes with a state with $\pi^*$ geometry changing the character of the state which the electron is ionised from and hence resulting in changes to the angular distribution of the emitted photoelectrons. It is not possible to observe this oscillation in the unaligned results.

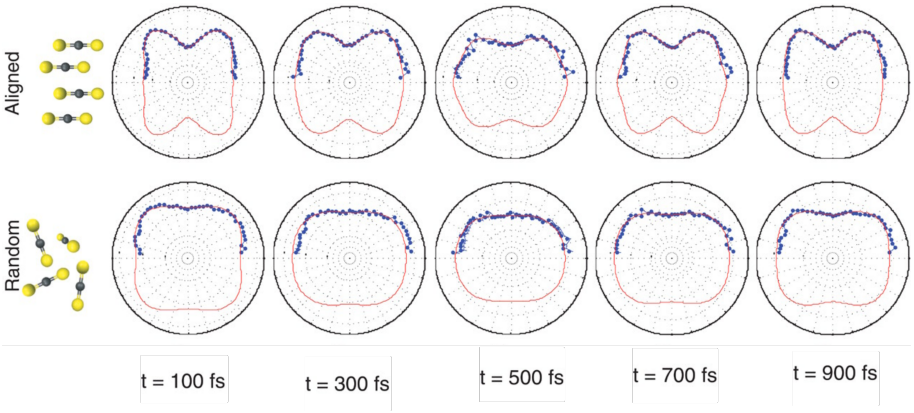


**Figure 1.7:** The time-resolved photoelectron angle distribution (PAD) following excitation by 200 nm and ionisation by 256 nm for aligned (top) and unaligned (bottom) $CS_2$. The aligned PADS show oscillations not observed in the randomly orientated PADS. Reproduced from [47] with permission from the American Association for the Advancement of Science.

Each of the techniques described in this section increases the information that can be recorded from TRPES to provide a more complete picture of the chemical dynamical processes being studied. However they also increase the complexity of the experiments making them challenging experiments to perform. These techniques currently use UV probes ($<$4.66 eV) meaning that they are not able to fully map the chemical dynamics. The lower flux from lab based source of XUV and the increased number of accessible cation states results in lower signal levels means a XUV probe has not been combined with the other techniques yet.

### 1.1.8 Alternatives to TRPES

Although TRPES is the technique used in the work described in this thesis and hence has been the focus of this chapter there are a wide variety of other techniques. A handful of alternative techniques which can provide a universal probe to study gas phase dynamics are discussed here.

As well as being able to ionise molecules, photons are also absorbed when exciting different levels within the molecule. This absorption is characteristic of the molecule,

therefore the absorption of photons can also be used as a probe to chemical dynamics, this is known as transient absorption spectroscopy (TAS). When the molecule has been excited by a pump laser, absorption due to the ground state will be depleted and there will be new absorption due to the excited state. There are a number of challenges when applying TAS to the study of gas phase dynamics. The simplest techniques use a single wavelength for the probe pulse and measure the absorption of the pulse [13, 49]. Due to pulse to pulse variation from lasers TAS usually requires a higher concentration of molecules than that presented in the collisionless molecular beams commonly used in TRPES, with gas cells often operating around 2 mbar [50]. It is possible to reduce the concentration required for TAS by splitting the pulse to allow both the pulse with and without absorption to be measured at the same time, this allowed Chen *et al.* to use a pressure of 0.1 mbar in their gas cell [20], which increases the complexity of the experiment apparatus and requires another detector. Another challenge with TAS is when using a single wavelength the molecule will move out of resonance with the wavelength, so a large amount of dynamics will not be observed. It is possible to use a number of single wavelength measurements to track the dynamics however this will increase the overall collection time [51, 52]. A solution to this is to generate a continuum of wavelengths meaning the absorption of the molecule at a wide range of wavelengths is measured simultaneously [53, 54]. Another significant issue is the absorption of UV and longer wavelengths is governed by selection rules which means there are dark states which cannot be observed. Using an X-ray continuum probe can overcome all these issues making it a universal probe for studying chemical dynamics in the gas phase, similarly to XUV TRPES [55, 56, 57]. These X-ray continuum are often generated using HHG. The large cross-section of the X-ray means the low concentration is less of an issue.

An alternative structural dynamics probe is a high intensity laser pulse. If the probe laser pulse is sufficiently intense the molecule will be multiply ionised. The result is positively charged fragments that repel each other, this is known as Coulomb explosion[58]. As

it is always possible to induce multiple ionisations, Coulomb explosion can also act as a universal probe. The kinetic energy and angular distribution of the fragments are then recorded. This gives a great amount of detail about the nuclear arrangement during the dynamics as the kinetic energy release will depend on how close the fragments are together. The close together, the greater the Coulombic repulsion and the greater the velocity of the fragments. However this doesn't provide information on the electronic structure [58, 59, 22]. Coulomb explosion imaging (CEI) required the dynamics during ionisation to be well understood as geometry change may occur during the ionisation step. Another issue with CEI is that the electric field produced by ions is large enough to distort the molecular potential energy surfaces. Applying this technique to larger molecules will be challenging as a large number of different fragments will be produced. CEI has successfully been applied to large molecules with more than 20 atoms and a number of fragmentation paths [60, 61]. However time-resolved CEI has only applied to small molecules up to substituted benzene ring [62]. These typically only have one fragmentation pathway and are two body fragmentation simplifying the analysis. Matsuda *et al.* have reported a time-resolve CEI experiment on the deuterated acetylene dication which results in both three and four body fragmentation [63].

Diffraction patterns from high energy electrons and X-rays also provide information about the nuclear structure and are a universal probe. A beam of electrons or X-rays are scattered of a gas sample, the resulting diffraction pattern is then recorded on a position sensitive detector. Interpreting these images can be challenging and often relies on theoretical models. Electrons have a higher scattering intensity by five to six orders of magnitude compared to X-rays[64] however X-rays can have higher flux sources and shorter pulses. Using MeV electrons, diffraction patterns that can provide sub-angstrom (0.6 Å) information with a temporal resolution of 150 fs have been measured [65]. However, the charged nature of electrons provides a number of difficulties, most significantly the space-charge temporal boarding [64, 66]. Recently the use of electric fields which de-

celerate the leading edge of the electron pulse and accelerates the trailing edge has been demonstrated to produce shorter pulses and overcome the space-charge effect[67, 68]. The electron probe is also sensitive to the small amount of cations often produced as by-products of the experiments [69]. X-ray diffraction experiments often use photon of about 9.5 keV [24, 70, 71] and have been able to achieve better time and spacial resolution (0.3 Å, 30 fs) than an electron beam[72].

Each of these techniques provides different information and combining multiple techniques is important to gain a more complete understanding of the chemical dynamics occurring.

## 1.2 Non-linear Optics

To electronically excite molecules with a single photon we need wavelengths shorter than those often produced by lasers and ideally be able to tune the wavelength to study different molecules. Fortunately, the development of lasers and in particular pulsed lasers opened up the field of non-linear optics which allows for frequency doubling and mixing to generate a large range of wavelengths. The ability to tune the wavelength of the laser pulse makes it possible to study a range of molecules with a single laser system and allows for control over the wavepacket excited by the pump laser.

At extremely high intensities it is possible to generate very high-order harmonic making it possible to convert infrared wavelength to wavelength as short as X-rays. This process is knows as HHG. Therefore it is possible to use HHG to generate high energy probes which are capable of ionise over the full reaction dynamics.

The rest of this chapter discusses how non-linear optics are used to generate the pump and probe laser pulses require for TRPES.

### 1.2.1 Non-Linear Optics

A high intensity laser will induce a non-linear polarisation, $P(\mathbf{t})$, in a material which can be described by an infinite series as given by,

$$P(\mathbf{t}) = \epsilon_0 \sum_{n=1}^{\infty} \chi^n E^n(\mathbf{t}) \tag{1.13}$$

where $\epsilon_0$ is the vacuum permittivity, $\chi^n$ is the $n$-the order dielectric susceptibility and $E$ is the electric field of the laser pulse. The electric field of the laser is modelled as a sinusoidal wave. Therefore we use the substitute $E(\mathbf{t}) = Ee^{-i\omega t}$ which lead to,

$$E^n = \left[Ee^{-i\omega t}\right]^n = E^n e^{-in\omega t}. \tag{1.14}$$

Hence there is a component of the polarization that has frequency $n\omega$ meaning there is a component of the electron cloud of the material that oscillates at $n\omega$ frequency generating light with a frequency of $n\omega$. In non-centrosymmetric systems all even terms are non-zero. Usually, the laser field is small compared to the molecular field so the laser can be considered as a perturbation and only two or three terms are required in the expansion given by equation 1.13. There are a number of crystals used for generating low order harmonics, which crystal is suitable depends on the wavelength of the driving laser. The crystal most frequently used with in the work presented in this thesis is $\beta$-$BaB_2O_4$ (BBO), a non-centrosymmetric crystal that is commonly used for frequency doubling of 800 nm to generate 400 nm light.

If two electric field with frequency $\omega_1$ and $\omega_2$ present in the crystal, the second order term becomes,

$$\begin{aligned} P^{(2)}(t) &= \epsilon_0 \chi^{(2)} E^2(t) \\ &= \epsilon_0 \chi^{(2)} \left[ E_1 e^{-i\omega_1 t} + E_1^* e^{i\omega_1 t} + E_2 e^{-i\omega_2 t} + E_2 e^{i\omega_2 t} \right]^2 \\ &= \epsilon_0 \chi^{(2)} \left[ 2E_1 E_1^* + 2E_2 E_2^* + \left( E_1^2 e^{-i2\omega_1 t} + E_2^2 e^{-i2\omega_2 t} \right.\right. \\ &\left.\left. + 2E_1 E_2 e^{-i(\omega_1+\omega_2)t} + 2E_1^* E_2 e^{-i(\omega_1-\omega_2)t} + c.c \right) \right] \end{aligned} \tag{1.15}$$

where $c.c$ is the complex conjugate. The third terms shows, light with frequency $\omega_1 + \omega_2$ is generated, this is known as sum frequency generation (SFG). The fourth term means that light of frequency $\omega_1 - \omega_2$ is also generated, this is known as difference frequency generation (DFG). This effect is used in an optical parameter amplifier (OPA) to produce a large range of wavelengths as described in more detail in 2.3.2. In this case, a white light source, which has a very broad bandwidth is used along with a pump wavelength (often 800 nm).

To generate a significant amount of a particular frequency, constructive interference between photons generated earlier in the crystal and those currently being generated is required. To achieve this constructive interference we need phase matching. For SFG ($\omega_3 = \omega_1 + \omega_2$) the phase matching condition is,

$$\boldsymbol{k_3} = \boldsymbol{k_1} + \boldsymbol{k_2} \tag{1.16}$$

where $\boldsymbol{k_n}$ is the wave vector for light with frequency $\omega_n$ and is given by,

$$\boldsymbol{k_n} = \frac{\omega_n n\left(\omega_n\right)}{c} \tag{1.17}$$

where $n\left(\omega_n\right)$ is the refractive index on the crystal at frequency $\omega_n$ and $c$ is the speed of light in a vacuum.

In most transparent materials the refractive index increases with frequency in the frequency range we are interested in. This means the phase matching condition in equation 1.16 can not be met, however in birefringent material the refractive indices are different along different axes making phase matching possible. This allows us to produce a wide range of wavelengths however to produce higher order of harmonics we need to increase the laser intensity such that we can no longer truncate equation 1.13. subsectionHigh Harmonic Generation To produce a probe that is high enough to ionise every atom/molecule (except helium) we use HHG. HHG is an extremely non-linear process, where the electric field of the laser is on the order of the atom/molecules electric field and hence perturbation theory breaks down and the high order terms become significant. HHG leads to the production of high energy photons which are capable of ionising from all states in a molecule. This is often desirable for a probe as it allows the full dynamics of the molecule to be observed. HHG is understood either through a semi-classical three-step model [73] which treats the electron as a point charge or a fully quantum mechanical model using the time-dependent Schrödinger equation [74]. The Semi-classical approach is able to make accurate predictions about the HHG process. The quantum approach is required to explain the electron recombination and quantum interference of electron trajectories in HHG.

#### 1.2.1.1 Semi-Classical Model

The three-step model is broken into three stages, ionisation, acceleration and recombination as shown in figure 1.8. In the first step, the intense laser field distorts the potential well of the electron enough to form a potential barrier allowing the electron to tunnel out, forming an ion. In an electric field, ionisation can occur either by tunnel ionisation or multiphoton ionisation. Which process dominates is calculated using the

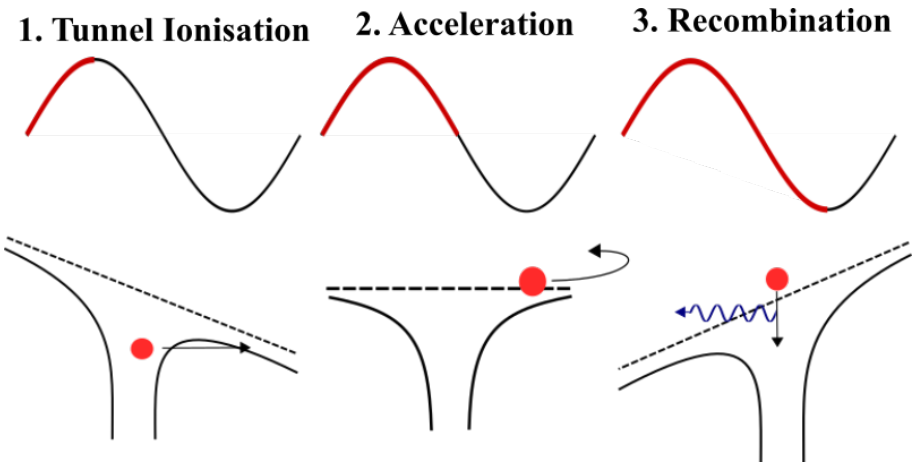


**Figure 1.8:** The three-steps in the three-step model of high harmonic generation. The top panel shows the electric field, with the red line showing the electric field. The bottom panel shows the electric field of an atom and the position of the electron. 1, the laser distorts the potential well so the electron tunnels out. 2, the electron is then accelerated. 3, the electron recombine to produce a photon indicated by the oscillating blue line.

Keldysh parameter which is given by,

$$K = \sqrt{\frac{I_p}{2U_p}}, \tag{1.18}$$

where $K$ is the keldysh parameter, $I_P$ is the ionisation potential. $U_p$ is the pondermotive energy of the electron and is given the equation,

$$U_p = \frac{e^2 E_0^2}{4\omega^2 m}. \tag{1.19}$$

where $E_0$ is the magnitude of the electric field, $\omega$ is the angular frequency and $m$ is the mass of an electron. Physically $K$ is the ratio of the time required to tunnel through the barrier compared to the period of the laser field. If $K > 1$ multiphoton ionisation is said to dominate, if $K < 1$ tunnel ionisation is said to dominate. HHG requires tunnel ionisation so $K$ needs to be less than 1.

The probability of tunnel ionisation can be calculated using the ADK tunnelling formula[75,

76],

$$W(t) = \omega_p |C_{n^*l^*}|^2 G_{lm} \left(\frac{4\omega_p}{\omega_T}\right)^{2n^*-m-1} exp\left[\frac{4\omega_p}{3\omega_T}\right] \tag{1.20}$$

where

$$\begin{gathered} f\omega_p = \frac{I_p}{\hbar}, \;\; \omega_T = \frac{eE(t)}{2m_e I_p}^{1/2}, \;\; n^* = \left(\frac{I_p^H}{I_p}\right)^{1/2}, \\ |C_{n^*l^*}|^2 = 2^{2n^*} \left[n^* \Gamma(n^* + l^* + 1)\Gamma(n^* - l^*)\right]^{-1}, \\ G_{lm} = \frac{(2l+1)(l+|m|)!}{2^{|m|}|m|!(l-|m|)!}. \end{gathered} \tag{1.21}$$

In these equations, $I_p$ is the ionisation potential of the atom and $I_H^P$ is the ionisation potential of atomic hydrogen. $e$ and $m_e$ are the charge and mass of the electron respectively. $l$, and $m$ are orbital angular momentum and magnetic quantum number respectively, $E(t)$ is the electric field amplitude. The effective quantum number $l^*$ is given by $l^* = 0$ for $l < n$ and $l^* = n^* - 1$ otherwise ($n$ is the principle quantum number). The probability of ionisation occurring during time interval $dt$ is given by,

$$P(t) = W\left[E(t)\right] dt. \tag{1.22}$$

When the laser intensity reaches the critical intensity $I_c$ the potential barrier is completely removed and over-the-barrier ionisation occurs at which point the tunnelling formula breaks down. $I_c$ can be obtained by equating the maximum that can be induced by the electric field to the ionisation potential[77],

$$I_c = 4 \times 10^9 (I_p\,[\text{eV}])^4 Z_R^2\, W cm^{-2} \tag{1.23}$$

where $Z_R$ is the residual charge.

ADK uses a quasistatic barrier model which is strictly only valid in the limit of $K \ll 1$, it also ignores the effect of multiphoton ionisation which is still occurring except in the limit of $K \ll 1$. Other ionisation models such as the Yudin-Ivanov (YI)[78] have been

demonstrated to produce more accurate results[79]. However the ADK model is still commonly used to calculate ionisation rate as it is computationally convenient and has been shown to be reasonably accurate when averaged over multiple laser cycles[80].

In the second step, the electron in the continuum is accelerated by the electric field of the laser. The laser field is modelled by

$$E = E_0 \sin(\omega t) \tag{1.24}$$

where $t$ is time, the acceleration is then given by,

$$a = \frac{eE_0}{m}(\sin(\omega t)). \tag{1.25}$$

Assuming the electron has zero kinetic energy and position at $t = t_0$, time of electron release we obtain equations for velocity and position of the electron once it is released from the atom.

$$v = \frac{eE_0}{m\omega}(\cos(\omega t_0) - \cos(\omega t)), \tag{1.26}$$

$$x = \frac{eE_0}{m\omega}\left(\frac{1}{\omega}(\sin(\omega t_0) - \sin(\omega t)) + (t - t_0)\cos(\omega t_0)\right), \tag{1.27}$$

The assumption that the electron has zero kinetic energy and position has been justified in the long wavelength limit [81], however the electron will not be produced at a small distance away from the nucleus with a small amount of kinetic energy as it requires motion to tunnel out of the barrier. If it had zero kinetic energy the probability of recombination would be large.

Figure 1.9 shows the trajectories of electrons released at different points in the electric field cycle. The graph shows only electrons released at certain times during the laser cycle will return to the atom leading to a burst in high harmonics every half cycle. Here

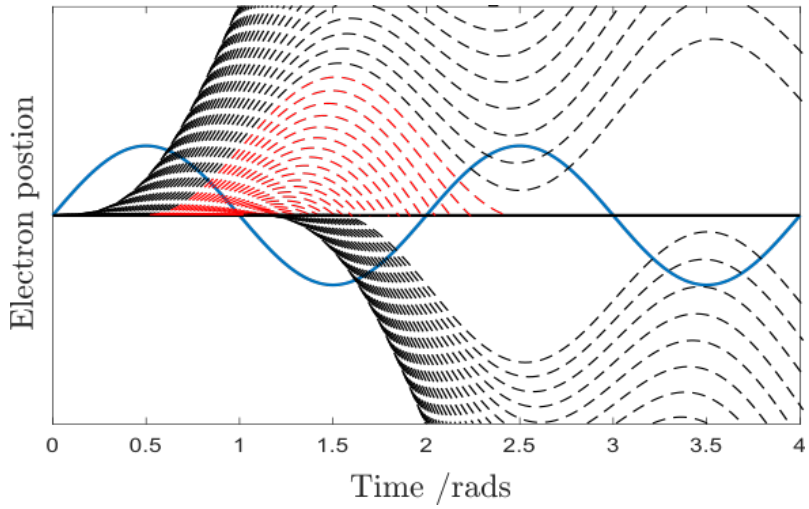


**Figure 1.9:** The solid blue line represents the driving laser electric field and the solid black line the nuclear position. The dotted lines show the trajectories of electrons released at different time during the laser cycle. The red lines represent the electrons which return to the nucleus and the black line the electrons which don't return in this 1D model.

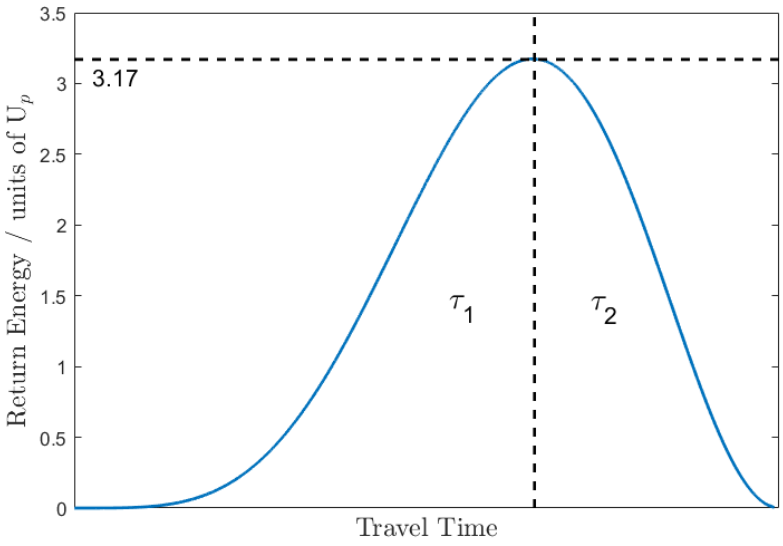


**Figure 1.10:** The return energy of the electron as a function the time spend in the continuum. The maximum gain energy is 3.17 $U_p$. Short trajectories are those on the left side of the horizontail line given by $\tau_1$ and the long trajectories are given by $\tau_2$.

it's important to point out the electron only returns if the light is linearly polarised. Circular polarization can be written as two linearly polarization electric fields which are perpendicular and have a $\pi/2$ phase difference, hence one component will bring the electron back to the parent atom but the other component will shift the electron laterally. The gain in energy of the electron when they return to the initial location is shown in figure 1.10. Apart from the maximum energy, there are two travelling times which have the same energy gain. One is the short trajectory ($\tau_1$) and the other is the long trajectory ($\tau_2$).The maximum energy is 3.17 $U_p$ where $U_p$ is the ponderomotive energy of the electron and is given by equation 1.19. This means the maximum energy of the emitted photon is,

$$E_{cutoff} = I_p + 3.17U_p. \tag{1.28}$$

This implies maximum energy increases indefinitely with laser intensity. This is not actually the case. Once the laser intensity is high enough the electron plasma reaches a critical density and becomes opaque to the fundamental driving frequency. Also once the laser intensity reaches $\sim 10^{17}$ Wcm$^{-2}$ the magnetic field is no longer negligible and will prevent recombination.

When we consider the ensemble of gas particles this process gives rise to harmonics which can be explained using the justification in section 1.2.1. At the high laser intensities used for HHG it is no longer possible to truncate equation 1.13 and perturbation theory no longer applies so the harmonic intensity no longer decreases as a power law. In a system with spherical symmetry, such as the ensemble of gas phase atoms used in our HHG experiments, a further symmetry constraint is that $P(E) = -P(-E)$. This means all even $\chi n$ have to be zero, hence only odd order harmonics are produced. Spherical symmetry is present in gas unless the molecules have been aligned breaking the symmetry and allowing even harmonics to be observed [82].

A typical HHG spectrum has three different sections, the perturbation region, plateau

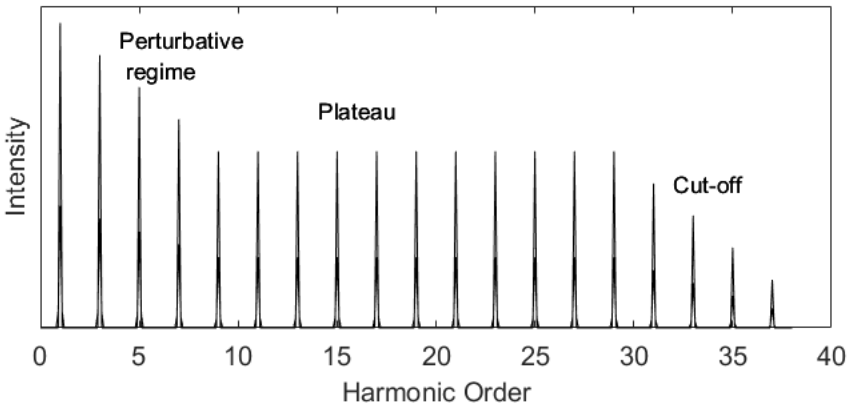


**Figure 1.11:** A typical HHG spectrum, with harmonics produced for odd orders only. Three regions are observe. The perturbative region when the intensity of the harmonics decrease with harmonic order. The Plateau region where the harmonic intensity is constant. And the cut-off region where the harmonics stop being produced.

region and cut-off region as shown in figure 1.11. The lower order harmonics ($< 9^{th}$) are produced at the leading and trailing edge of the laser pulse and larger radii of the laser spot where the intensity is lower and therefore can be described by perturbation theory. The harmonic intensity in this region decrease as a power law of the harmonic order. The higher harmonics are generated at higher laser intensity where the electric field of the laser is comparable to the atomic electric field and the harmonic intensity in this region is fairly constant. In this region there are two electron trajectories contributing the harmonic $\tau_1$ and $\tau_2$ as shown in figure 1.10. Within the plateau region there is an equal probability that an electron will return with any of the energies within the region and therefore the intensity of the harmonics are constant. The final region is the cutoff region. The cutoff photon energy is determined by equation 1.28.

#### 1.2.1.2 Quantum Model

The semi-classical model predicts a cutoff energy which is lower than the observed cutoff, it is also unable to explain the characteristics of the plateau region. To deal with this a full quantum model is required. This involves solving the time dependent Schrödinger

equation

$$i\hbar\frac{\partial}{\partial t}|\Psi(x,t)\rangle = \left[-\frac{\hbar^2}{2m_e}\nabla^2 + V(x) - E\cos(t)x\right]|\Psi(x,t)\rangle \tag{1.29}$$

where $|\Psi(x,t)\rangle$ is the electronic wavefunction, and $V(x)$ is the Coulomb potential which is often approximated using a soft Coulomb potential,

$$V(x) = -\frac{1}{4\pi\epsilon_0}\frac{e^2}{(a_0^2 + x^2)^{1/2}} \tag{1.30}$$

where $\epsilon_0$ is the permittivity of free space, $e$ the electronic charge and $a_0$ the Bohr radius. The soft Coulomb potential is a mathematical requirement to avoid singularities. Lewenstein et al.[74] solved equation 1.29 numerically using a truncated harmonic oscillator potential and three assumptions:

1. Contribution to the evolution of the system from all bound states except the ground state can be ignored.

2. The depletion of the ground state can be ignored.

3. In the continuum the electron can be treated as a free particle moving in the electric field.

Assumption 2) is only valid when the laser intensity is smaller than the critical intensity ($I_c$) when the potential barrier is completely removed. Both 1) and 3) are usually valid for small Keldysh parameters ($K$) when the ionisation is not through multi-photon ionisation. Assumption 3) implies that when the electron appears in the continuum it is under a strong electric field and when it returns to the nucleus it has a larger enough kinetic energy that the atomic potential force can be ignored. Obviously this is not true for the lower energy electrons which produce the lower harmonics.

This model showed that the phase of the dipole moment depends on the laser intensity.

It also predicts a cutoff energy,

$$E_{cutoff} = I_p F + 3.17 U_p \tag{1.31}$$

where $F$ is a function of $I_p/U_p$ and equals $1.32$ when $I_p \ll U_p$ and decreases as $I_p/U_p$ increase. This cutoff energy is larger than predicted by the classical model in equation 1.28 and better matches experimental results. The reason for this is that electron cannot appear at the origin as it must tunnel out, it, therefore, can gain additional kinetic energy on the way back to the origin however the electron diffuses, which tends to an average and decrease the additional energy gain for large $I_p$[74].

#### 1.2.1.3 Phase Matching

Similar to the SFG and the lower order harmonic generated in non-linear crystals, we want to phase match the harmonic being generated by HHG. This means the harmonic generated must have the same phase as those generated earlier in the medium so they constructively interfere. For this, the phase of the driving laser at the moment of generation must be the same as the phase of the harmonics that have already been produced. The distance over which the fundamental and harmonics become out of phase is called the coherence length.

$$L_{coh} = \frac{\pi}{\Delta k} \tag{1.32}$$

where $\Delta k$ is the phase mismatch. For phase matching $\Delta k = q k_0 - k_q = 0$, where $q$ is the harmonic order $k_q$ the harmonic wavevector and $k_0$ the fundamental wavevector. In HHG there are four components that lead to phase mismatch and a reduction in harmonic intensity. [83, 84]. A geometric term $\Delta k_{geo}$, a neutral atom term $\Delta k_{na}$, a free electron term $\Delta k_{fe}$ and an atomic phase term $\Delta k_{at}$ that combine additively.

$$\Delta k = \Delta k_{geo} + \Delta k_{na} + \Delta k_{fe} + \Delta k_{at} \tag{1.33}$$

In a gas cell or jet, $\Delta k_{geo}$ is from the Gouy phase shift as a result of focusing the fundamental [85]. The Gouy phase shift is given by,

$$\phi_{Gouy}(z) = \tan^{-1}\frac{z}{z_0} \tag{1.34}$$

where $z_0$ is the Rayleigh length and $z$ is the longitudinal distance. The derivative of equation 1.34 is the prorogation vector and therefore the phase mismatch from the Gouy phase shift and is given by,

$$\Delta k_{geo} = \frac{qz_0}{z^2 + q^2 z_0^2} - \frac{qz_0}{z^2 + z_0^2}. \tag{1.35}$$

This phase mismatch depends on the generation location relative to the focus position, hence the position of the gas relative to the focus is important. The further from the focus the larger the coherence length. It is always positive and in an idealist system is symmetric in the laser propagation axis around the focus. However experimental the focus is rarely symmetry, especial when ionisation has occurred changing the refractive index.

The neutral atom term is a result of the different refractive indexes for different wavelengths. This means the fundamental and harmonics travel at different speeds in the neutral gas. The phase mismatch is given by,

$$\Delta k_{na} = \frac{2\pi q}{\lambda_f} p(\Delta n + n_2)(1 - \eta), \tag{1.36}$$

where $\lambda_f$ is the wavelength of the fundamental. $p$ is the gas pressure (in atm), $\Delta n$ is the difference in the refractive index between the fundamental and the harmonic ($n_f - n_q$). $n_2$ is the non-linear refractive index for the fundamental and $\eta$ is the ionisation fraction which is the fraction of the atoms which have been ionised. The fundamental refractive index is always smaller than the harmonic refractive index so $\Delta n$ is always negative.

The free electron term is a result of the refractive index of the liberated electrons (plasma) which are present in the gas. The refractive index of plasma is,

$$n_p(\omega_0) = \sqrt{1 - \frac{\omega_P^2}{\omega_0^2}} \approx 1 - \frac{\omega_P^2}{2\omega_0^2} \tag{1.37}$$

The approximation is valid when $\omega_P^2 \ll \omega_0^2$. Where $\omega_0$ is the laser frequency and $\omega_p$ is the plasma frequency given by,

$$\omega_p = e\sqrt{N_e \epsilon_0 m_e} \tag{1.38}$$

where $\epsilon_0$ is vacuum permittivity, and $N_e$ is the density of free electrons given by,

$$N_e = \eta p N_{atm} \tag{1.39}$$

where $N_{atm}$ is the atomic number density at 1 atm. This means the phase mismatch due to free electron can be written as,

$$\begin{aligned} \Delta k_{fe} &= \frac{2\pi q}{\lambda_f} \left[ n_p(\omega_0) - n_p(q\omega_0) \right] \\ &= \frac{N_e e^2 \lambda_f}{4\pi \epsilon_0 m_e c^2} \left( q - \frac{1}{q} \right) \\ &= \eta p N_{atm} r_e \lambda_f \left( q - \frac{1}{q} \right) \end{aligned} \tag{1.40}$$

where $r_e$ is the classical electron radius given by,

$$r_e = \frac{e^2}{4\pi \epsilon_0 m_e c^2} \tag{1.41}$$

This equation is often simplified using the assumption $q \gg 1$. It is possible to balance the effect of the medium dispersion and the plasma dispersion when $\eta$ is less than one. At the critical ionisation fraction it is no longer possible to balance the medium and plasma terms. For argon this is about 5% [86].

The final term is the atomic phase term which is due to the intrinsic phase of the harmonics caused by the time delay between ionisation and recombination. The phase mismatch is given by,

$$\Delta k_{at} = \alpha_q \frac{\partial I}{\partial z}, \tag{1.42}$$

where $\alpha_q$ is a coefficient related to the electron trajectories and $I$ is laser intensity. $\alpha_q$ is $\approx$ 1-5$\times 10^{-14}$ cm$^2$W$^{-1}$ for short trajectories and $\approx$ 20-25$\times 10^{-14}$ cm$^2$W$^{-1}$ for long trajectories [86]. The longer the electron are in the continuum the larger the time difference between ionisation and recombination. For a Gaussian beam equation 1.42 becomes,

$$\Delta k_{at} = \frac{8 z \alpha_q I_0}{z_0^2 \left[1 + \left(\frac{2z}{z_0}\right)^2\right]^2}, \tag{1.43}$$

where $I_0$ is the peak intensity. As the laser intensity varies radially so will the atom phase term. This term is often ignored as it is negligible over short interaction ranges, however, a SIGC has a long interaction region so this term cannot be ignored. It may be possible to find situations where $\Delta k_{at}$ reduces the effect of $\Delta k_{geo}$ to improve overall phase matching as shown in a theoratical study by Saliéres *et al.* [87].

The intensity $I_q$ of the $q^{th}$ harmonic after travelling a distance of $L$ through a medium, ignoring absorption is proportional to,

$$I_q \propto \frac{L^2 \sin^2(\Delta k_q l/2)}{(\Delta k_q l/2)^2} \tag{1.44}$$

If phase mismatch is zero, the harmonic intensity increase quadratically, otherwise the intensity oscillates with a period of twice the coherence length.

#### 1.2.1.4 Absorption

When completely phase matched the harmonic intensity increase with interaction length and gas pressure. However, the absorption of harmonic also increases with length and

gas pressure. Constant *et al.* [88] performed an analysis of the time-dependent factors that affect the harmonic intensity. They found the overall of optimum conditions to be,

$$L > 3L_{abs} \text{ and } L_{coh} > 5L_{abs} \tag{1.45}$$

where $L_{abs}$ is the absorption length, given by

$$L_{abs} = \frac{1}{\beta(\omega)k(\omega)} \tag{1.46}$$

where $\beta(\omega)$ is the attenuation coefficient. Through out the work in this thesis we have used argon gas. For argon at 1 atm at 21 eV $\beta$=4.63x10$^{-4}$ which gives an absorption length of 20 $\mu$m [89]. As absorption scales linearly with pressure, the absorption length at 10 mbar is 2.0 mm.

#### 1.2.1.5 Wavelength Dependence

From equation 1.28 and 1.19 we see that increasing the driving wavelength extends the cut-off limit. However as the wavelength increases the harmonic yield decrease. Single atom response calculations obtain the yield power law $\propto \lambda^{-x}$ with $5 \lesssim x \lesssim 6$[90]. An experiment which studied the harmonic generation in xenon and krypton at four driving laser wavelengths across the range 800 nm-1850 nm and measured $x$=6.3$\pm$1.1 and $x$=6.5$\pm$1.1 for xenon and krypton respectively [91]. A significant increase in harmonic intensity when doubling the driving laser from 800 nm to 400 nm has also been observed in argon [92]. This power law appears to be caused by two effects, the increased time spent in the continuum by the electron results in greater spreading of the wavepacket, reducing the probability of recommendation. This gives $x \approx 3$ for the overall harmonic yield. The second effect is the increased spectral range of the harmonics as the cutoff energy increase leading to more harmonics being generated resulting in a decrease of $x \approx 2$ in a fixed window of the spectrum [90].

#### 1.2.1.6 Experimental Sources of XUV Photons

Generation of XUV photons from HHG in a gases medium was first observed over three decades ago [93] and has since become a common source of lab-based XUV photons. A decade ago HHG was also observed from a solid source [94]. Interestingly generation from solids required much lower intensities [95]. HHG has been shown to be possible in liquids too, but due to a number of difficulties this has remained uncommon [96, 97]. Throughout this thesis we generate from gas sources and therefore is limited the discussion to HHG in gases, a review of HHG in solids can be found in reference [95].

Noble gases are usually used as the interaction medium. This is due to the high ionisation potentials (IP) of these atoms which increases the cut off energy of the harmonics. Lighter noble gases have higher IP but are also smaller so the probability of recombination is reduced, reducing the conversion efficiency. These two effects have to be balanced [98]. Throughout this thesis we have used argon which has an IP of 15.8 eV [99]. This is a good balance of the two effects and also on a practical consideration argon is a relatively cheap gas meaning it is possible to perform longer experiments. Molecules such as $O_2$ and $N_2$ have also been used for HHG as they also have large IP's and are larger however they often have lower efficiency [100, 101, 102]. This is due to effects of dynamics caused by the laser field which can reduce recombination efficiency such as alignment.

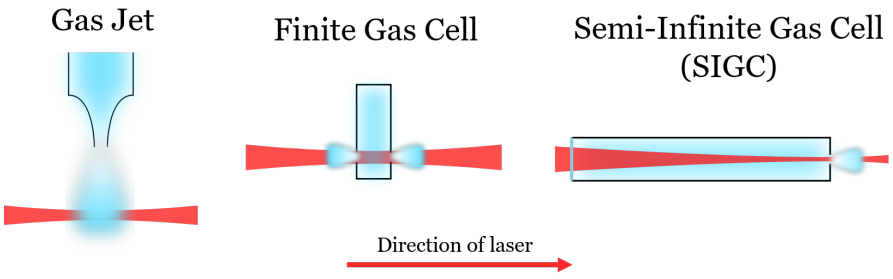


**Figure 1.12:** Three experimental geometries used for high harmonic generation from gases.The blue indicate the location of the gas and the red line is showing the location of the laser focus relative to the gas. The images are not to scale.

A number of geometries to generate high harmonics have been employed to generate high harmonics to try to increase the amount of flux (photons $s^{-1}$) of the sources. The three common geometries are shown in figure 1.12 One of the earlier sources used was a gas jet. The efficiency of a gas jet is determined by the phase matching conditions as the gas pressure is too low for the absorption to be significant. The interaction region is small leading to low conversion efficiencies. In gas cells, re-absorption of harmonics also plays an important role in the conversion efficiencies. A finite gas cell has a length on the order of the Rayleigh length of the driving laser, usually less than 1 cm. The Rayleigh length is the distance along the propagating axis between the beam focus to where the beam width is a factor of $\sqrt{2}$ larger than at the focus. The length of SIGC is significantly larger than the Rayleigh length, usually greater than $\sim 30$ cm. The highest efficiencies have been achieved with a SIGC. Brichta *et. al*[103] measured the conversion efficiency of a SIGC as about $10^{-4}$, roughly 100 times more efficient than their gas jet and double the efficiency of the finite gas cell. Their set-up optimises for the total harmonic output but for the 13th harmonic of 800 nm, the harmonic of interest within the research present in this thesis, the SIGC has a conversion efficiency about 10 times greater than the FGC and 20 times greater than the gas jet. A detailed study of the phase matching of harmonics in a SIGC can be found in reference [104].

An XUV photon source that is suitable for TRPES has to be able to produce a coherent femtosecond pulse with a photon energy around 20 eV. Other than HHG the only other suitable XUV photon source is free electron lasers (FELs). A FEL uses a beam of electrons accelerated to relativistic speeds and using a set of magnets with alternating pole wiggles the beam perpendicular to its direction of travel. This results in synchrotron radiation. The radiation provides a ponderomotive force that causes the bunching of electrons which leads to the FEL output being pulsed. FELs can produce a wide range of photon energy with a range of (at different facilities) from radio waves to X-rays (0.75 meV-20 keV, 1.5 m-0.6Å). X-ray FELs currently provide pulse lengths between a

few hundred femtoseconds to sub fs. The disadvantage of FELs is they require large and expensive user facilities which have limited access. There are a number of different FELs across the globe that provide a wide range of different capabilities, a summary of the different FELs currently operational can be found in reference [105]. Both Flash 2 in Germany and Fermi 1 in Italy are capable of producing photons around 20 eV. Flash 2 produces photons in the range 14-310 eV with pulse length in the range of 10-200 fs (estimated). While Fermi 1 produces photons in the range 12.3-65 eV with a pulse length in the range 50-100 fs.

sectionSummary To study the wide array of chemical dynamics which can be initiated with laser pulses, a wide range of experimental techniques are required to provide different information. TRPES can be particularly useful as it allows changes in electronic structure to be mapped as a function of time. Also ionisation is always possible from any state given enough energy meaning there are no dark states which can not be observed. TRPES has already been employed to study a number of different dynamic process such as dissociation [106, 107, 17], relaxation [108, 109, 110] and ring dynamics [111, 112, 113]. Some of these experiments [106, 107, 110, 111, 112] have made use of a high energy probe which means the ionisation step can always occur and hence is a universal probe and allows the complete dynamics to be observed. Such a probe is created using either a free electron laser or HHG. The advantage of HHG is that it is a table-top method and hence suitable for many labs.

# Chapter 2

# Experimental

In chapter 1 we considered the theoretical foundations of both HHG and TRPES experiments, now we turn our attention to the practical considerations of carrying out such experiments. The characterisation of the SIGC presented in chapter 3 was carried out using the Laser system at Southampton. The photoelectron spectroscopy of methyl iodide presented in chapter 4 and 5 was carried out using the Artemis Laser system at the Central Laser Facility. In this chapter both laser systems will be discussed in detail as well as the beam paths and the vacuum chambers.

## 2.1 Introduction

In lasers, light is amplified through stimulated emission. This requires a larger population in the upper lasing state than the lower state. To achieve this non-Boltzmann distribution the laser medium is often pumped via a diode or another laser of short wavelength to a higher state which then relaxes quickly to the upper lasing state. A diagram of this is shown in figure 2.1a). Figure 2.1a) is a 4-level lasing system, this produces continuous light at a specific wavelength.

The light is trapped in a cavity. Figure 2.1b) shows a simplified example of a cavity

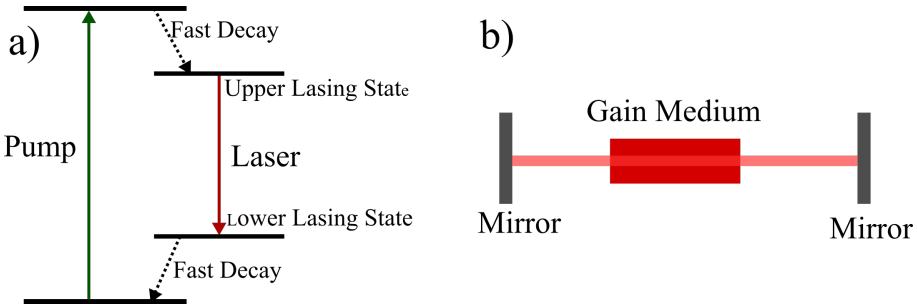


**Figure 2.1:** a) shows the simplified energy levels in a four level lasing system which would produce monochromatic light. The horizontal lines represent the electronic level and the arrows show the direction of electron transitions. b) shows the simplest form of a laser cavity. Two mirrors trap light in the cavity with a lasing gain medium.

where the laser bounce between two mirrors with the gain medium in between. The laser is amplified in the gain medium. To form a standing wave in the cavity the length of the round trip must be an integer number of wavelengths. Wavelengths that fit the criteria are known as cavity modes.

To produce nanosecond laser pulses, Q-switching is used. The laser is stopped from working by preventing a cavity from forming, often this involves blocking one of the cavity mirrors. This is usually done by some sort of shutter, for example, a Pockels cell combined with a polariser. This results in a build up of the upper lasing state population. At a set point, the shutter is turned off allowing the cavity to lase. This results in a rapid build up of the laser light resulting in a short pulse. Once the pulse has happened and population inversion is lost, the shutter is turned back on, preventing the laser lasing again. This allows for population inversion to occur again.

To produce shorter pulses a lasing medium with a large gain bandwidth is required. The bandwidth arises from having a large number of states in the upper lasing level. The requirement for a large bandwidth is due to the uncertainty principle, which it can be

shown for a Gaussian shaped pulse to be,

$$\Delta t \Delta \nu \geq 0.441 \tag{2.1}$$

where $\Delta t$ is the pulse length and the $\Delta \nu$ is the frequency spectral width. Titanium-doped Sapphire (Ti:sapph) has the required bandwidth to produce femtosecond laser pulses and is the most commonly used gain medium to produce ultrashort laser pulses. Ti:sapph has a bandwidth of about 200 nm. The pulses produced by Ti:sapph are centred around 800 nm. The large bandwidth of Ti:sapph means a large number of laser modes can be supported in the cavity. Over 100,000 modes interfere to produce a femtosecond pulse[114]. Figure 2.2 shows how coherently adding more lasing modes can produce short pulses. Initially, in the laser cavity each modes' phase is completely random, however, to produce short pulses the relative phase relationship between the modes must be fixed. Figure 2.3 shows the effect of all modes a having fixed phase relationship in blue and those same modes having a random phase relationship in red. The phase relationship is fixed through a process called mode-locking. Passive mode-locking relies on fluctuations in the laser intensity which allows for a high intensity fluctuation to then be amplified

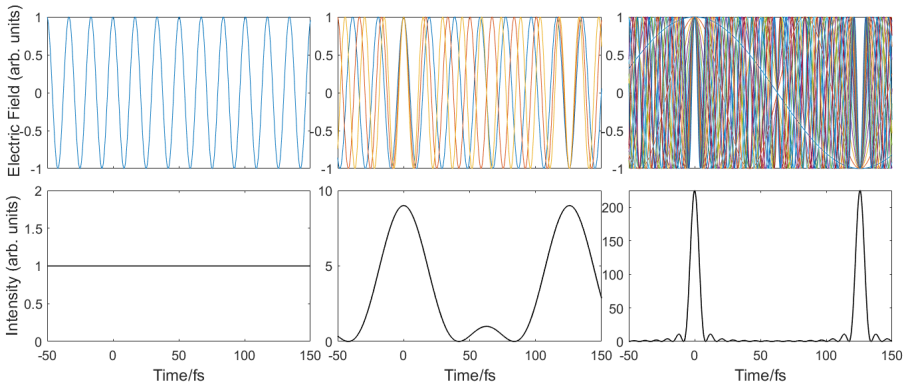


**Figure 2.2:** The left panel shows the electric field and intensity from a single mode at 800 nm, The middle show the same information but for 3 modes centred at 800 nm and the right panel shows the electric fields and intensity for 15 modes. All the modes have the same phase factor. As modes are added the laser pulses become shorter

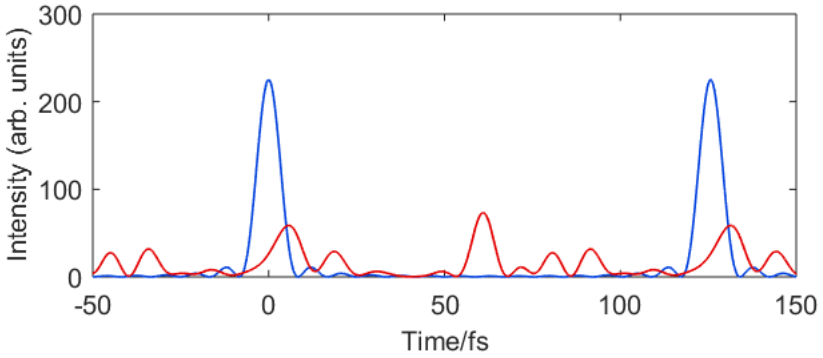


**Figure 2.3:** The blue line is the laser intensity for 15 modes with the same phase factor, the same as the bottom right graph is figure 2.2. The red lines are the same 15 modes but each with random static phase factors, demonstrating the requirement of the same phase factors to produce laser pulses.

and compressed using a positive feedback. The fluctuation may be due to laser noise or be caused actively such as knocking a cavity mirror. An example of passive mode-locking is Kerr lens mode-locking. Active mode-locking uses periodic reduction in the laser Q-factor to force mode-locking. The Q-factor is a measurement of the "quality" of the cavity and is inversely proportional to the rate of energy loss from the cavity. This shutter opens once a round trip, an acousto-optic modulator (AOM) is often used for this.

## 2.2 Southampton Experimental Set-up

### 2.2.1 Laser System

The production of high energy femtosecond laser pulses requires multiple stages, a schematic of the laser system used is shown in figure 2.4. The system comprises of a Spectra Physics Tsunami Ti:sapph oscillator which is pumped by a Spectra Physics Millennia. The Oscillator pulse is amplified by a Spectra Physics Spitfire Pro Chirped Pulse Amplifier (CPA), which is pumped by Positive Light Evolution 20.

The Millennia pump laser outputs continuous wave (CW) green light at 532 nm with

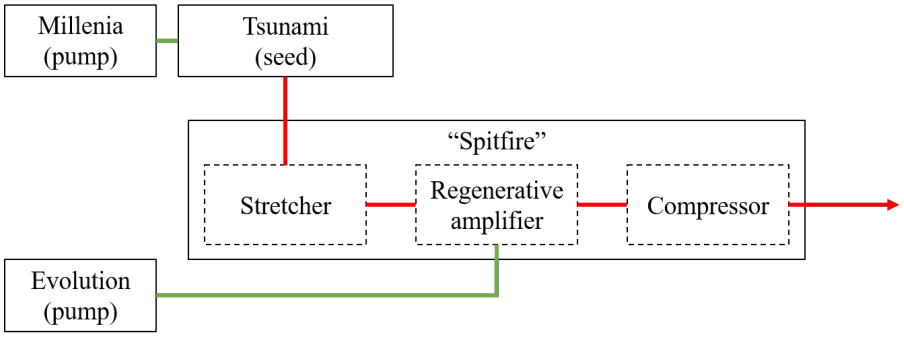


**Figure 2.4:** A schematic of the femtosecond laser system in Southampton. The green lines represent the pump lasers, the red line represents the output from the oscillator and amplifier. There is three stages in the the Spitfire, together these stages are known as chirp pulse amplification.

an output power of 3.8 W. This is achieved by using an Nd:$YVO_4$ (neodymium-doped yttrium orthovanadate) gain medium to produce 1064 nm light which is then frequency doubled to 532 nm by a lithium borate doubling crystal (LBO) inside the cavity.

The Millennia output pumps the Tsunami Ti:sapph oscillator. The mode-locked Tsunami produces a $\sim$ 40 fs pulse centred around 800 nm and a bandwidth of around 50 nm, with a repetition rate of 82 MHz and an average power of 300 mW. A schematic of the optics inside the Tsunami is shown in figure 2.5. The Tsunami is initially mode-locked using an AOM. An AOM is a crystal with a piezoelectric transducer attached to produce

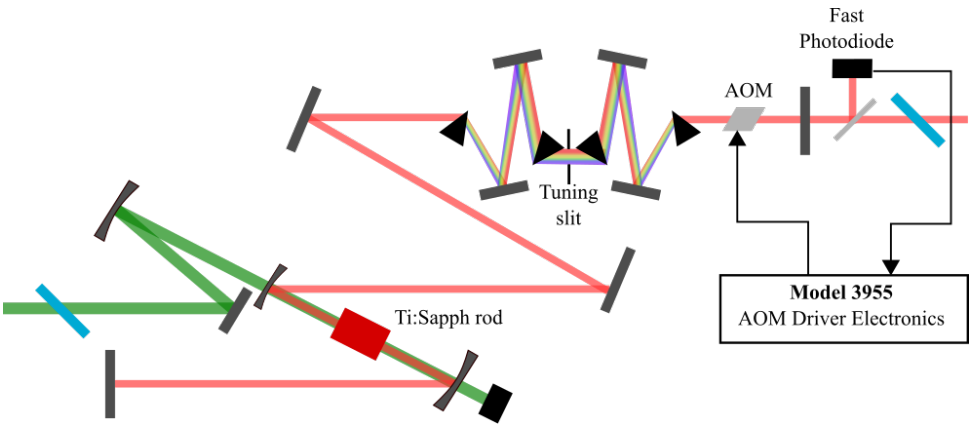


**Figure 2.5:** The beam path of both the pump and seed beam through the Tsunami laser. The green line indicates the pump path while the red is the seed path. The rainbow indicates the spatial separation of frequencies by the prism of the seed beam. Mirrors are indicated by gray rectangles while Brewster windows are shown as blue rectangles. AOM is acousto-optic modulator.

an acoustic standing wave in the crystal. This changes the crystal refractive index to create a diffraction grating. Once per a round trip the amplitude of the standing wave goes to zero, effectively turning the grating off and the incident light passes through, however the rest of the time some of the incident light is diffracted out of the cavity inducing cavity loss, reducing the cavity Q-factor. This results in the formation of a single pulse which reaches the AOM when the grating is off. Once the Tsunami is producing laser pulses the AOM is turned off to allow the spectrum to broaden around a central wavelength of 800 nm. The four prisms in the laser control the group velocity dispersion (GVD). The first prism angularly disperses the beam, the second collimates and then the third and fourth reverse the process, meaning short wavelengths travel shorter distances through the prism. This compensates for positive GVD (red edge leading the pulse) which occurs in the Ti:Sapph rod and other components in the cavity. Positive GVD occurs in the gain medium due to the Kerr effect which results in the refractive index varying with the laser field as $\Delta n = n_2 E^2$. The tuning slit can also be moved to change the central wavelength. The width of the slit affects the spectral width.

A small fraction of the laser exits through the final mirror after each round trip. A round trip is about 12.2 ns, leading to 82 MHz repetition rate. The output from the Tsunami passes into the Spitfire chirped pulse amplifier. A schematic of the optical layout in the Spitfire is shown in figure 2.6. The Spitfire is pumped by a Q-switched, diode-pumped Evolution Laser.

The Evolution produces green light at 527 nm using a Nd:YLF (neodymium-doped lithium yttrium fluoride) gain medium to produce 1053 nm light which is frequency doubled with a LBO crystal inside the cavity. The Q-switching is achieved by two AOMs in series. This significantly reduces the cavity Q-factor so that lasing is unable to occur. This means that no stimulated emission can occur but the pump laser is still exciting the crystal meaning that a higher population inversion occurs than in a continuously lasing system. Nd:YLF has a long excited state lifetime (470 $\mu$s) which allows for excited state

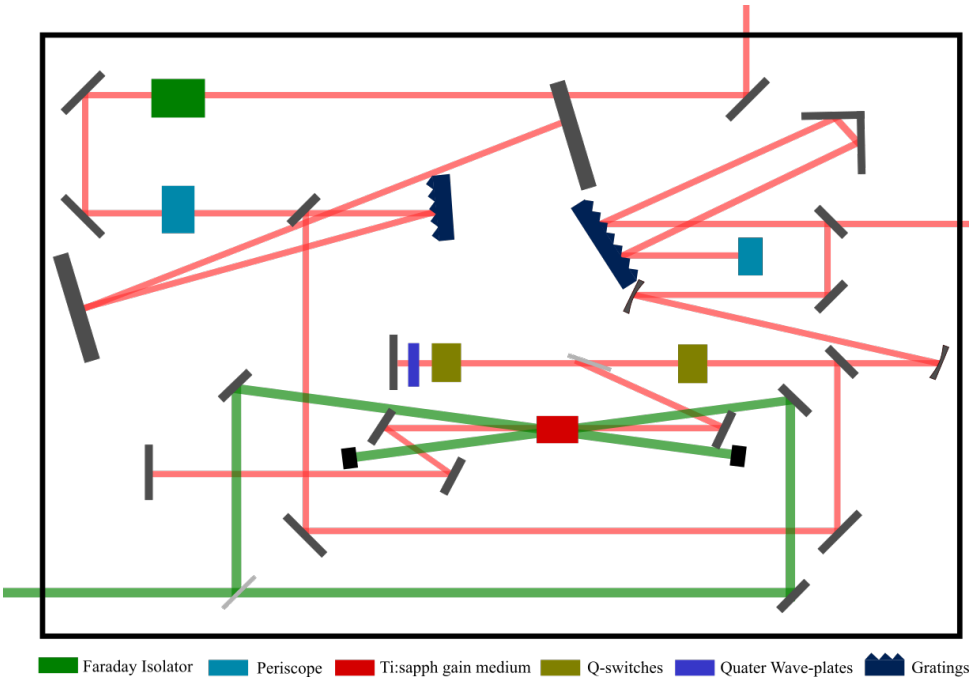


**Figure 2.6:** The seed path through the Spitfire amplifier, shown with red line and the pump shown by the green line. The key for the different optics is shown at the bottom of the figure.

build up. The AOMs are then turned off to allow lasing to occur again. This results in a 10 ns, 27 mJ laser pulse at 527 nm. The greater population inversion results in a large amplification of the light through the crystal giving a pulse. Once the pulse exits the laser the AOMs are turned back on and the process starts again. This happens 1000 times a second, producing a 1 KHz laser output.

When a pulse from the Tsunami initially enters the Spitfire it passes through a Faraday isolator, which only allows light to travel one way through it, therefore it stops any unwanted back reflections. The Spitfire uses a process known as chirp pulse amplification (CPA) which stretched the pulse before amplification and then recompresses the pulse after. The pulse is then stretched using a grating. As different wavelengths of light diffract at different angles this results in a spectral spread of the laser pulse and as different wavelengths now have different path lengths the pulse is also spread in time. The pulse makes four passes of the grating. This reduces the peak power to help prevent

optical damage during the amplification process, while ideally the overall power of the laser pulse says the same. However gratings have about 10%, as the pulse makes four passes this results in about a third of the laser power being lost, this is a bigger problem for the compressor[115, 116]. A seed pulse is then selected by a synchronisation and delay generator (SDG), this reduces the repetition rate to 1 KHz. The chosen pulse passes through the first Pockels cell (PC) (right on figure 2.6) while a voltage is applied across the PC. This voltage causes the PC to act as a quarter waveplate (QWP) and hence the pulses polarisation changes from linear to circular. The thin film polariser (TFP) transmits the vertical component of the pulse into the cavity, while the horizontal component is reflected into a beam dump. The second PC is off so that the pulse is only affected by the QWP. As the pulse passes through the QWP twice the polarisation is changed to horizontal meaning it is now reflected by the TFP which now forms part of the laser cavity. The second PC is now turned on so that with the QWP it acts as a full waveplate and the pulse polarisation doesn't change. This pulse is amplified by passing through a Ti:Sapph crystal in an optical cavity about 13 times. A cavity round trip may be added or removed to maximum the output power as this depends on the alignment of the laser. This amplifies the pulse energy by a factor of approximately $10^6$ times, to a pulse energy of $\sim$ 3 mJ. Once the gain has been saturated the pulse is coupled out of the laser cavity by turning off the second PC so that the polarisation is changed to vertical and then is transmitted by the TFP. The gain saturation is the point when the 800 nm pulse is intense enough that it depopulates the upper lasing state reducing the stimulate emission such that absorption of the pulse is more significant and the pulse intensity starts to decrease. Finally the pulse is then recompressed back down to about 50 fs, again by four passes of a grating which reverse the chirp introduced by the stretcher so that the final pulse is unchirped and original pulse length. The resulting pulse is centred at 790 nm, with a power of $\sim$3 mJ and a repetition rate of 1KHz. The pulse length can be as short as 40 fs however a more typical value is about 50 fs.

### 2.2.2 Laser Diagnostics

To check the laser is working as expected a number of diagnostic tools are used. The power, spectrum and beam profile are measured after the Tsunami. The power is measured with a thermal power meter and is typically around 300 mW. The beam spot is measured using a complementary metal-oxide-semiconductor (CMOS) camera. This allows us to check for clipping of the beam as well as changes in alignment through the Tsunami. The spectrum is recorded here with a fibre optic coupled with an Ocean optics HR200 CG-UV-NIR spectrometer. This is done to check the central wavelength that enters the spitfire is consistent and to maximise the bandwidth of the spectrum produced when the Tsunami is mode-locked.

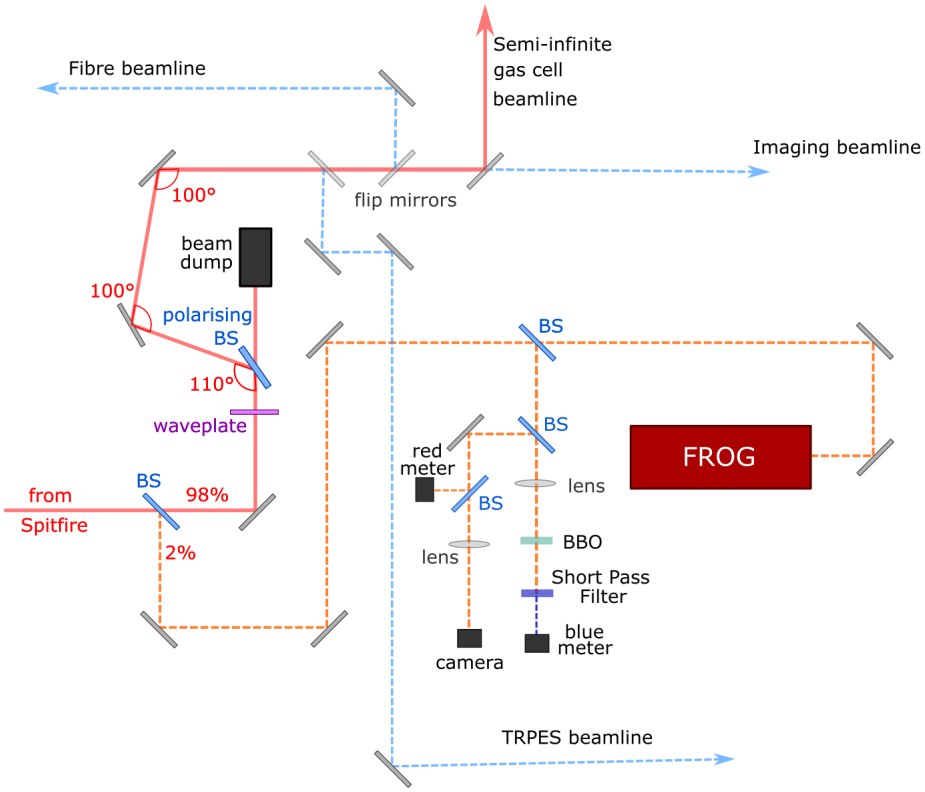


**Figure 2.7:** The beam path out of the spitfire. The solid red line is the path to the semi-infinite gas cell experiment. The dashed blue lines show the laser path to other experiments around the lab. The orange dashed line as the beam path to the laser diagnostics. Figure adapted from [117] with permission.

After exiting the spitfire 2% of the beam is split to go to a number of diagnostics as shown in figure 2.7. A thermal power meter is used before the waveplate to measure the power of the main beam. An optimal power is about 2.8 W. The spectrum of the beam is also occasionally measured here too. Again a CMOS camera is used to image the beam profile. We have a red-blue meter that measures the ratio of the fundamental laser to the second harmonic. The more second harmonic generated the shorter the pulse allowing for pulse compression to be optimised. The does not provide a measurement of the pulse length but allows us to track drifts in compression. We also have Frequency-Resolved Optical Grating (FROG) to optimise and measure the pulse length of the laser pulse.

Due to the short pulse length, femtosecond pulses have to be measured against themselves. As any detector is slow compared with the laser pulse we have to use a non-linear measurement. In Southampton we use a Swamp Optics GRENOUILLE FROG. In a FROG the pulse is split into two and one pulse is delayed with respect to the other, before being focused through a non-linear crystal. In a traditional FROG this is done with

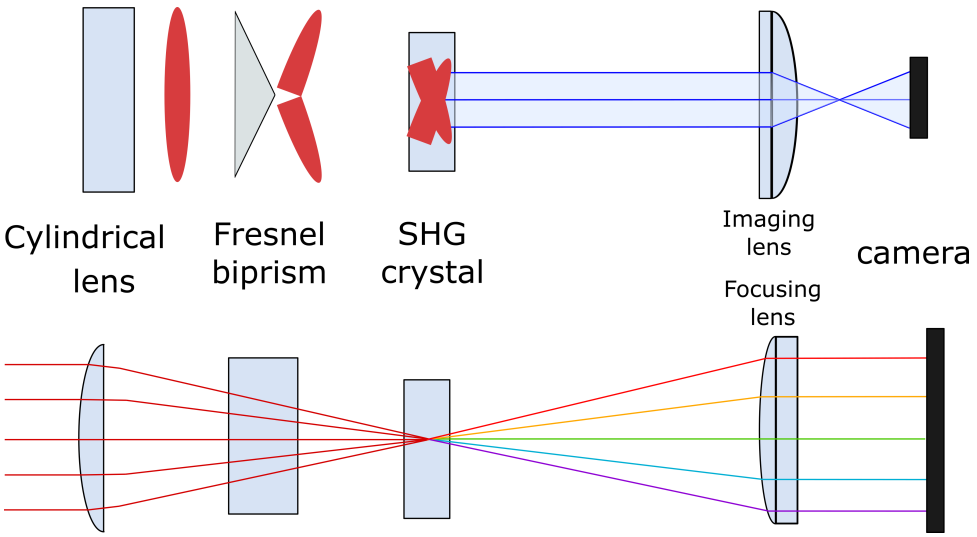


**Figure 2.8:** The optics for a GRENOUILLE FROG from two perpendicular directions. The top panel shows how the time resolution is obtained. The red oval indicates the laser pulse while the blue lines shows the second harmonic light generated in the crystal. The bottom plane shows how spectral resolution is achieved. Figure adapted from [117] with permission.

a delay stage. However in the GRENOUILLE this is achieved using a Fresnel biprism. This simplifies the system and removes the need for moving parts. The optic setup for a GRENOUILLE is shown in figure 2.8. The Fresnel prism is positioned before a non-linear crystal and after a cylindrical lens which focuses the laser vertically into the crystal. The Fresnel biprism splits the pulse into two. Each half has a delay that varies with horizontal position due to the changing thickness of the biprism. This means the horizontal axis of the image from the camera after the crystal corresponds to time. The vertical axis corresponds to frequency. This is due to each frequency phase matching in the crystal at different incident angles, as the laser is focused vertically into the crystal we achieve a range of angles each causing SHG at different frequencies. To get significant separations of frequency a thick crystal is required. An iterative Fourier phase retrieval algorithm is then used to recover the phase of the pulse. Our system also split a small amount of the laser towards a camera before it enters the optics for the FROG, this beam is used to align the FROG.

### 2.2.3 SIGC Experimental Apparatus

As shown in figure 2.7 after the beam splitter for the diagnostics, there is a waveplate followed by a polarising beam splitter. The incident light hits the beamsplitter at $55^o$ which is the Brewster angle. In this case the Brewster angle is the angle at which P-polarised light is transmitted. The S-polarised (polarised perpendicular to the plane of incidence) component is reflected. By rotating the waveplate we change the ratio of S and P polaristion of the laser allowing for the amount of the laser power reflected to be controlled. After the beam splitter there is a number of flip mirrors to allow the laser beam to be reflected to the different experiments around the lab. The beam path specifically for the SIGC is shown in figure 2.9. The optics with dash lines are those which are added to switch the beamline from 800 nm to 400 nm. The optics can be quickly put into place so that it is quick to change between the wavelengths. The beam passes through a focusing lens with a focal length of 75 cm just before the entrance

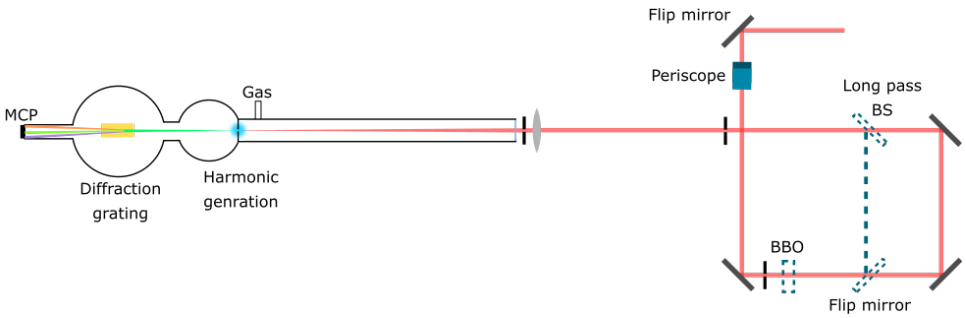


**Figure 2.9:** The beam path used to investigate the production of high harmonics in a semi-infinite gas cell. The dashed blue lines show the optics which are added to change the beam path from 800 nm to 400 nm. In this case a beam block is also added between the right most mirrors to block the 800 nm. The black lines across the beam path indicated the location of the irises. The blue circle indicates the location of the harmonic production. The red line indicates the path of the driving laser, the green line is the high harmonics which are then separated according to wavelength by the diffraction grating.

window to the SIGC which is filled with argon. The lens was made from N-BK7 when using 800 nm but was changed to a UV fused silica lens for the 400 nm experiment. At 800 nm, 13% of the laser power is lost passing through both the lens and window, at 400 nm it is 16%. To separate the SIGC from the vacuum outside, copper tape is placed over a 1.5 mm pinhole. The laser then burns a hole on the order of ∼100 $\mu$m through the tape.

The power after the final mirror is around 1.7 W, this means the pulse energy is 1.7 mJ, each pulse is $\sim$ 50 fs. This means the peak power $P$ is,

$$P = \frac{\text{pulse energy}}{\text{pulse duration}} = \frac{1.7 \times 10^{-3}\,\text{J}}{45 \times 10^{-15}\,\text{s}} = 3.4 \times 10^{10}\,\text{W}. \tag{2.2}$$

From images of the focused beam taken using a CMOS camera, as discussed in section 3.4, we know the focus spot size $\omega_0$ (not to be confused with $\omega$ used for frequency) is $\sim$ 30 $\mu$ m, corresponding to the standard deviation of the Gaussian intensity profile. The intensity at the focus is, therefore,

$$I = \frac{P}{\pi\omega_0^2} = \frac{3.4 \times 10^{10}\,\text{W}}{\pi \times (3 \times 10^{-3}\,\text{cm})^2} = 1.2 \times 10^{15}\,\text{Wcm}^{-2} \tag{2.3}$$

A laser intensity of around $10^{14}$ Wcm$^{-2}$ is required for HHG [118], meaning we have enough intensity to achieve HHG.

For 400 nm we had a laser power of about 0.5 W and a pulse length of $\sim$ 50 fs, which gives a power of $1.0 \times 10^{10}$ W. As the wavelength is half of 800 nm we expect the focal spot to also be half the size. Using equation 2.3 we get an intensity of $1.4 \times 10^{15}$ Wcm$^{-2}$ which is again high enough for HHG.

A schematic of the vacuum chambers is shown in figure 2.10. The SIGC is 63 cm with a flange near the entrance window which a roughing pump can be connected to, to pump out the cell quickly. The argon enters the cell through a 4 mm diameter pipe near the exit of the cell. The exit of the cell is a solid O-ring with a 1.5 mm hole that is covered with copper tape. A diagram of the exit hole is shown in figure 2.11. The next chamber has two 350 L/s turbos, which are backed by the same roughing pump to rapidly pump away the gas escaping from the SIGC. This is done to reduce the absorption of the harmonics in the gas. This chamber has a base pressure of about 2x10$^{-5}$ mbar and a operating pressure on the order of $10^{-3}$ mbar. The chamber is then connected to the detection chamber as shown in figure 2.10, where the harmonics and the fundamental are separated by a Hitachi 0266 focusing grating. Before the beam enters the chamber there

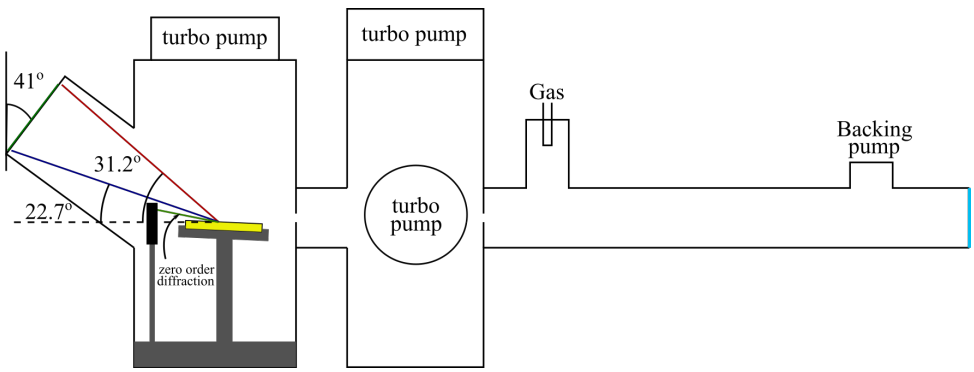


**Figure 2.10:** A schematic of the vacuum chambers required for generation and detection of the harmonics. The red ad blue lines indicate the maximum and minimum angles which would still hit the MCP respectively.

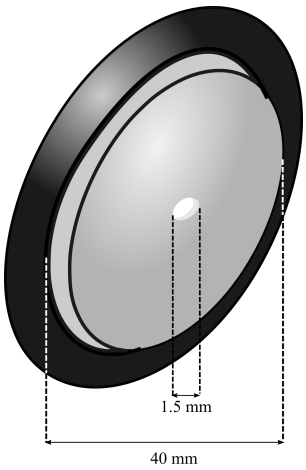


**Figure 2.11:** A diagram of the O-ring exit hole of the semi-infinite gas cell. The black ring is the rubber o-ring which has a inner diameter of 400 mm. In the centre there is a 1.5 mm hole which is covered with copper tape.

is a 1 mm pinhole to select the centre of the beam to provide good spatial resolution of the harmonic. Another iris is placed after the grating to block the 800 nm. The harmonics pass over the top of the iris and are detected on position-sensitive microchannel plates (MCP). When a photon hits the MCP it causes a cascade of electrons, amplifying the signal. The MCP has a phosphor screen behind it and the electrons cause the screen to fluoresce. This is captured via an AVT-Manta-G-235 camera which has a CMOS chip and a pixel size of 5.86 $mu$m. A birds-eye picture of the detection chamber is shown in figure 2.12, along with two tin filters used to calibrate the spectrometer.

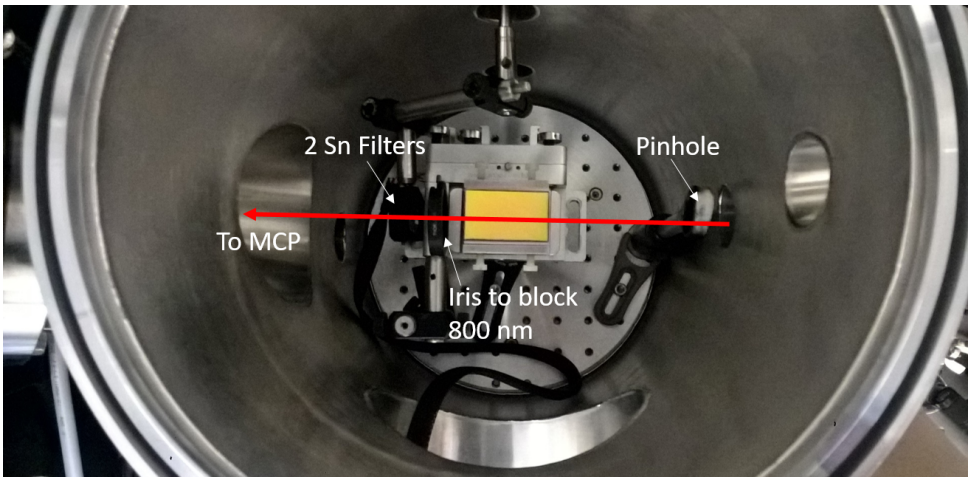


**Figure 2.12:** An image looking down into the flat field chamber. The red line shows the path of the harmonics. A mount with tin filters is sometimes added for calibration of the spectrometer. The precise angle of the grating can be changed but is about $5^o$. Angles are defined either parallel or perpendicular to the laser table as indicated by the diagram.

This chamber has a single 300 L/s magnetic turbo which is backed by a roughing pump. This keeps the chamber below 5x10$^{-5}$ mbar. The detector is at 41 degrees relative to the vertical as this results in all the harmonics on the detector being close to their focus. The grating is mounted on a goniometer stage to allow movement of the grating angle. For best focusing conditions an angle of 5.75$^{o}$ is required. More detail on the chamber design can be found in reference [77]

#### 2.2.3.1 Microchannel plates

To detect photons and photoelectrons micro-channel plates (MCP) are used. Each plate is a matrix of tiny (4-25 $\mu$m) glass capillaries. A voltage is applied over the plate so that when a particle or photon hits the channel wall secondary electrons are produced. The channels are angled slightly away from perpendicular (typically 4$^{o}$-12$^{o}$) to maximise electrons colliding with the channel walls. Each plate can increase the signal by as much as $10^4$. Often MCPs are stacked to create a chevron stack comprising of two (or more) plates with the channels having slightly different angles to increase signal amplification, a diagram is shown in figure 2.13. The cascade of electrons can be detected by an anode at the back of the MCP, and the resulting current is measured or, when information about the position of the hitting photons/electron is important, a phosphor screen can be placed behind the MCP. The cascading electrons causes the screen to fluoresce and the resulting image is then recorded with a camera.

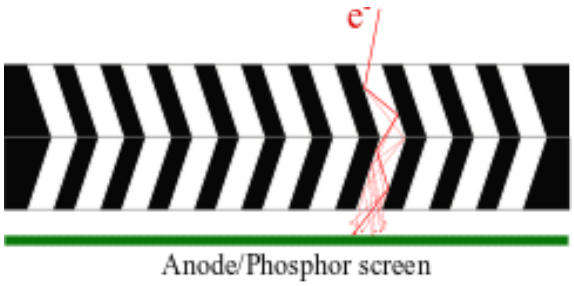


**Figure 2.13:** Schematic of an MCP chevron stack used to detect electrons and photons. The thick red line indicated the path of the initial electron which the thinner lines indicate the cascading electrons.

## 2.3 Artemis Experimental Set-up

To perform the TRPES experiments presented in chapter 4 and 5 we used the Artemis laser system at the Central Laser Facility. The Artemis facility produces 790 nm, laser pulses at 1 KHz repetition rate with a maximum output of 12 W. The laser can then also be combined with XUV generation and/or an optical parametric amplifier (OPA) to generate a tunable wavelength across the IR to UV range. The laser pulse can be combined with a number of end stations to perform several different types of experiments. We used the Atomic Molecular Optical (AMO) end station which was configured with two different detectors, the time-of-flight (TOF) and the velocity map imaging (VMI) spectrometers.

### 2.3.1 Laser System

The laser system is a RedDragon Ti:Sapph chirped pulse amplifier (CPA) from KM Labs. This laser system uses two stage amplification with both Ti:Sapph crystals cryogenically cooled to about 50 K using helium gas. The amplifier uses a standard multi-pass bow tie configuration as shown in figure 2.14. The laser path from the amplifier to the end stations is shown in figure 2.15. First, the output is split into two separate compressors so that the compression and chirp of the probe and pump laser pulses can be optimised separately. The resulting pulses have a length of about 30 fs. The output from compressor one is used to create a UV pump pulse using a HE-TOPAS as described in section 2.3.2. Around 8 W of 790 nm generates a few mW of UV. There is also a

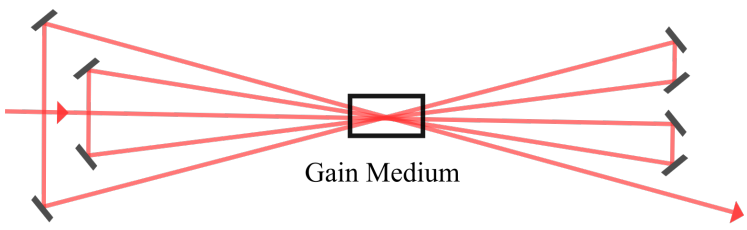


**Figure 2.14:** Diagram of the beam path of a multi pass amplifer in the bow-tie configuration

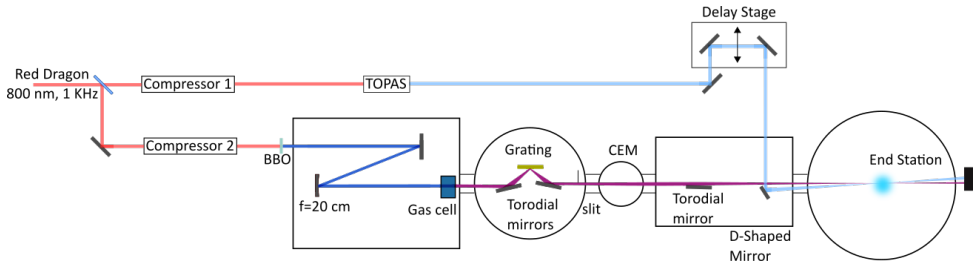


**Figure 2.15:** A diagram of the laser path at Artemis from output of the red dragon to the interaction region. The red line indicates the 790 nm laser. Light blue is the UV pump. Dark blue is the 395 nm light and the purple is the XUV beam. The blue circle represents the sample gas and the interaction region.

delay stage in the pump beam line to change the time delay between the pump and probe pulses. The pump beam is then focused into the interaction region using a 1 m convex mirror. A D-shaped mirror is used to direct the beam into the end station as this allows for a small angle between the two laser pulses and hence a greater overlap volume.

The output from compressor 2 forms the probe pulse. The first step is to use a BBO to convert $\sim$ 4 W of 790 nm to $\sim$ 500 mW of 395 nm. An XUV pulse is generated by HHG in a 2.5 mm long finite gas cell. The gas cell is enclosed in a cube that has apertures for the light to enter and exit. The cube is pumped by a high throughput IGX vacuum pump to remove as much gas as possible. The vacuum chamber itself has a large turbo pump which is backed by a roughing pump. The large pump capacity means that a high flow rate in the gas cell can be used while still maintaining a working pressure of $10^{-4}$ within the vacuum chamber while harmonics are being generated. Before the gas cell, there is a 20 cm focusing mirror. The mirror is within the vacuum chamber to avoid burning the entrance window which would reduce power and lead to odd phase matching conditions which are important for harmonic generation efficiency. A short focusing length leads to a small focus spot size and hence high laser intensities. The gas cell has a 100 $\mu m$ aperture which is covered by copper tape which the beam burns through creating a hole to enter and exit the cell. The cell is filled with argon to generate harmonics using a mass flow controller from Bronkhorst. The meter can be set between 0 and 200 SCCM

(standard cubic centimetres per minute).

To isolate the desired harmonic energy a time preserving monochromator is used. This consists of a toroidal mirror that focuses the light onto a diffraction grating to select the desired wavelength. The grating lines are, unusually, parallel to the laser beam as this has been found to be better to maintain temporal coherence while maintaining high diffraction efficiency. A second toroidal mirror then recollimates the beam after the grating. The monochromator has five different diffraction gratings on a translating stage so that they can be individually selected depending on which wavelength is required. This means the monochromator can cover a range of 12-120 eV. After the monochromator there is an adjustable slit that controls the frequency resolution and the power of the XUV pulse.

Between the monochromator and the next vacuum chamber there is a channel electron multiplier (CEM) which can be lowered into the beam path to measure the harmonic count and spectrum. A CEM works similarly to an MCP as described in section 2.2.3.1 however it is a single glass capillary instead of a matrix. A spectrum is produced by scanning the angle of the monochromator. This allows the harmonic intensity to be optimised and check the correct harmonic is being used. An example of the spectrum produced is in figure 2.16 which show two peak corresponding to the 5th and 7th harmonic of the 395 nm driving light. The energy calibration is a rough internal calibration between the angle of the monochromator and photon energy. Changes in alignment mean it is not precise. The photon flux is measured as the current from the cascading electrons in the glass capillary.

Finally, another toroidal mirror with a 1 m focal length focuses the beam into the detection chamber. The toroidal mirror is positioned just before the D-shape mirror for the pump beam. Both mirrors are mounted on movable stages to give some control over both beams as they enter the end stations and therefore can be optimised on the

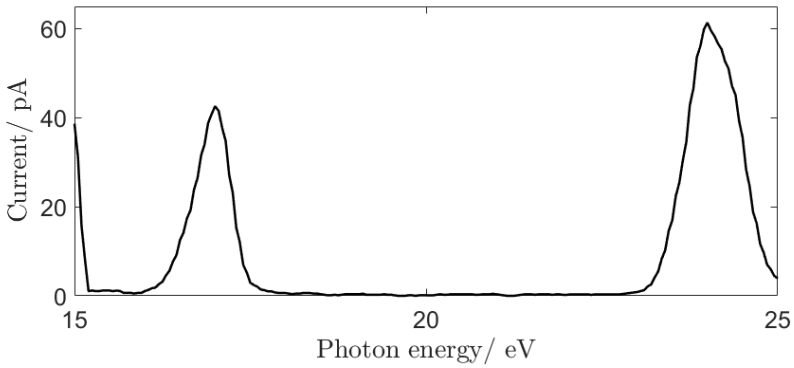


**Figure 2.16:** Spectrum obtained using the CEM of the harmonics produced by the 395 nm driving laser. The energy calibration is a rough internal calibration between the angle of the monochromator and photon energy. It is not very precise due to changes in alignment. The photon flux is measured as the current from the cascading electrons in the glass capillary.

centre of the interaction region. This is particularly important for the XUV beam as although the experiment can be aligned with the 395 nm light there always will be some variation in the position with the XUV beam. The spatial overlap of the two beams can be monitored by inserting a Lutetium Aluminium Garnet (LuAG:Ce) scintillator crystal into the overlap region. The angle of overlap between the pump and probe is about $3^o$

Alternatively, the 395 nm pulse can itself be used as the probe by removing the gas cell, setting the monochromator to the zero order, allowing all the incident light to pass through. The slit is also opened to its maximum distance to avoid damage to the slit.

### 2.3.2 Optical Parametric Amplifier

The OPA at Artemis is a HE-TOPAS from Light Conversion. An OPA uses non-linear optics to generate a range of wavelengths, the theoretical underpinnings of processes used in the OPA have been described in section 1.2.1. An OPA uses a pump beam and a signal beam with frequencies $\omega_p$ and $\omega_s$ respectively. The beams are overlapped and phase matched in a non-linear crystal. This depletes the pump, amplifies the signal and

produces a third frequency $\omega_i$ called the idler, with frequency defined by

$$\omega_i = \omega_p - \omega_s. \tag{2.4}$$

This process is shown schematically in figure 2.17.

By using a white light source for the signal input, there is a range of wavelengths that can be produced or amplified. A white light source is generated by focusing a faction of the pump wavelength into a dielectric medium which displays third order non-linearity leading to the formation of a filament and significant spectral broadening. The desired wavelength is varied by chirping the white light in a thick crystal and then changing the delay between the white light the 800 nm laser to temporal overlap with different wavelengths of the white light. The output power is optimised by rotating the crystal to change the angle between the polarisation of the beam and the crystal's optic axis to improve phase matching. This allows the HE-TOPAS to output to range from 1.1-1.5 $\mu$m for the signal and 1.5-2.5 $\mu$m for the idler beam.

To produce shorter wavelengths of light the output of the OPA can pass through a series of non-linear optics to drive second harmonic generation (SHG) and sum frequency

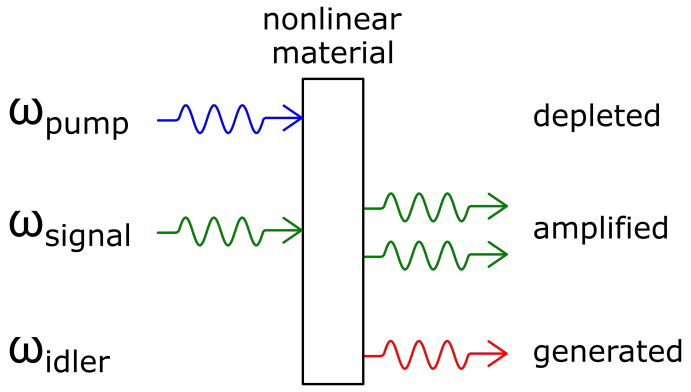


**Figure 2.17:** A digram of the process of an OPA. A pump and signal light is mixed in a non-linear crystal so that a pump photon is coveted to a signal and idler photon. This depletes the pump, amplifies the signal and created a new wavelength. Figure reproduced from [117] with permission.

generation (SFG) processes. Figure 2.18a shows the different ways the pump, idler and signal can be combined using SHG and SFG to produce wavelengths covering the complete range from 235-1100 nm. Figure 2.18 b) shows which wavelengths are produced for different configurations and the maximum energy which can be produced for each wavelength. As you can see there is a large range of maximum power that can be produced for different wavelengths.

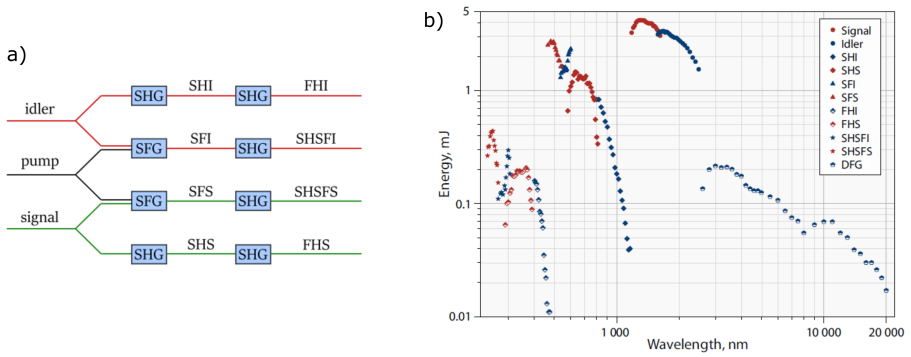


**Figure 2.18:** a) shows the different processes that can be used to generate a wide range of wavelengths using three different wavelengths given by the idler, pump and signal. The initials used are as followed: SH= second harmonic, FH= fourth harmonic, SF = sum frequency, SHSF = second harmonic of sum frequency, I = idler, S = Signal. b) shows how it is possible to combine these processes in a HE-TOPAS along with the signal and idler and those longer wavelengths generated by difference frequency generation to provide a tunable source from 235 nm-2.5 $\mu$m. The driving energy for the pump is about 8 W. Figure a) reproduced from [117] with permission and figure b) is reproduced from [119] with permission.

### 2.3.3 End Stations

At the end station, the laser beams and molecular samples are overlapped and the produced photoelectrons are detected. For the experiments we carried out the photoelectron spectra were recorded using electron TOF or VMI. At Artemis the AMO end station can be configured to have either detectors. The lasers are overlapped using a scintillator crystal.

The sample can be introduced by using 1 KHz Amsterdam Cantilever nozzle with 100 $\mu$m aperture to create a molecular beam. A skimmer with a 1 mm hole is placed about 10

mm away from the skimmer to select the coldest, densest part of the molecular beam. The bottom section has two large turbo pumps so that a fairly high gas pressure can be used to create the molecular beam whilst having the required low pressure to safely operate a MCP. This means the chamber has a base pressure of 1x10$^{-7}$ mbar and a working pressure of 1x10$^{-3}$ mbar when the molecular beam is being formed.

However a number of things can go wrong with a pulse nozzle and it may not be possible to use the pulse nozzle with the desired molecule, for example if it is corrosive to the o-rings in the nozzle. In these cases a diffuse beam can be created using an aperture of about 100 $\mu$m, as this is simpler. As the beam is diffuse it is created closer to the interaction region than the molecular beam only a few centimetres away.

A molecular beam is more dense and also colder than a diffuse beam which is often useful. However they are also more complex with more parts that can be damaged/broken and require more precise overlapping especially when pulsing the nozzle as this will require time as well as spatial overlap.

#### 2.3.3.1 Time of Flight (TOF)

Electron TOFs are often used to record the kinetic energy of photoelectrons. The concept is simple, electrons with higher kinetic move faster so by recording the time it takes to hit a detector the kinetic energy can be calculated. The equation for the kinetic energy of the electron is given by:

$$E_{KE} = \frac{1}{2} m_e \nu^2 = \frac{1}{2} m_e \left(\frac{d}{t}\right)^2 \tag{2.5}$$

where $m_e$ is the mass of the electron, $d$ the distance travelled and $t$ is the time of flight. The further away the detector is from the interaction region the better the energy resolution, however, as the electrons are emitted in all directions this reduces the collection efficiency. To increase collection efficiency charged cones are used at the

entrance of the flight tube. However, these must be weak to avoid significant changes in the kinetic energy of the electrons.

The electron TOF at Artemis is the commercially available ETF11 from Kaesdorf. The spectrometer is designed to be 3 mm from the interaction region for maximum collection efficiency. The entrance of the spectrometer is an electrostatic cone with a 3 mm aperture. With the lens activated the acceptance volume is 200 $\mu$m. We found the optimal voltage for the cone to be 100 V. After the cone there is a drift tube with $\mu$-metal shield to prevent any stray magnetic field affecting the spectrometer.$\mu$-metal is a ferromagnetic alloy with a very high magnetic permeability, this provides a low reluctance path for the magnetic field meaning that inside of a $\mu$-metal casing is shielded from magnetic fields. A voltage can be applied to the drift tube to accelerate or decelerate the electrons depending on the polarity of the voltage. We found not applying a voltage on the drift tube to be best. The length of the drift tube and cone together is 350 mm. Then there is 111 mm long region that accelerates electrons by 1 keV before hitting the detector. This is done to minimise the effect of the earth's magnetic field which may penetrate through the back of the spectrometer. The acceleration in this region is high enough that the time spend by the electron here is negligible compared to the time of flight. The spectrometer has a resolution of $\frac{T}{\Delta T} \sim 100$ which means for an electron with energy on the order of 10 eV the resolution of the spectrometer is on the order of 0.1 eV. The detector is a 40 mm MCP and the spectrometer is differentially pumped to keep the MCP at a low pressure.

#### 2.3.3.2 Velocity Map Imaging (VMI)

A VMI not only records the electrons' kinetic energies but also their angler distribution. A schematic of how this is achieved is shown in figure 2.19 and is based on the design of Eppink and Parker [120]. When the laser has irradiated the molecular beam, a spherical distribution of photoelectrons known as a Newton sphere is created. A number

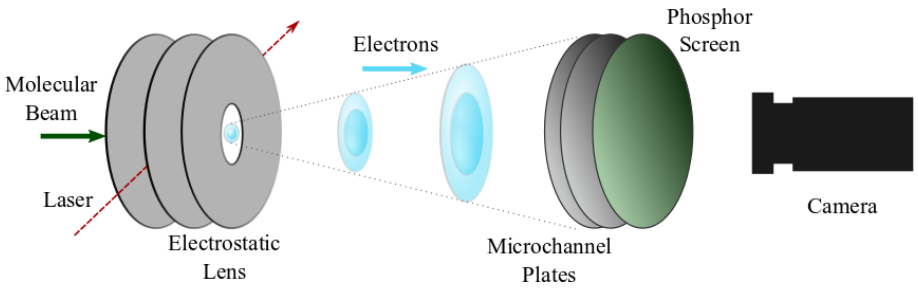


**Figure 2.19:** Schematic diagram of velocity map imaging (VMI) spectrometer with 3 electrostatic plates accelerating the newton sphere shown by the blue circles towards and MCP with a phosphor screen. The laser and the molecular beam interact between the back and middle electrostatic lens.

of shells are created with different electron kinetic energies. These Newton spheres are accelerated via the electrostatic lens towards a position sensitive detector. The lens means that photoelectrons of the same momentum produced at different parts of the interaction region are focused to the same point on the detector. The electrostatic lenses are usually comprised of three electrostatic plates. The plate behind the source is known as the repeller the second plate is the extractor and the third is the ground. The electrons are produced in between the repeller and extractor plates. The voltage on the extractor is approximately 70% of that of the repeller voltage. The ratio of the voltages are adjusted to achieve optimal focusing. An example of the electric field that is produced from three electrostatic lenses is shown in figure 2.20. The electric field resembles an optic lens and it may be helpful to think of this as working similar to an optic lens.

The VMI at Artemis is the standard 3 plate design from Eppink and Parker. The molecular beam enters via a 2 mm hole in the repeller plate. Having a small hole helps maintain a flat field behind the molecules. The extractor and ground have a larger hole of 10 mm. All the plates have a diameter of 70 mm and are separated by 10 mm between each plate. The MCP is 30 cm behind the ground plate and is also 70 mm in diameter. Again there is $\mu$-metal shielding the spectrometer from stray magnetic fields. The images of the phosphor screen behind the MCP are taken using a scientific CMOS (sCMOS) camera (PCO Gold Edge 5.5). As long as cylindrical symmetry is present it is

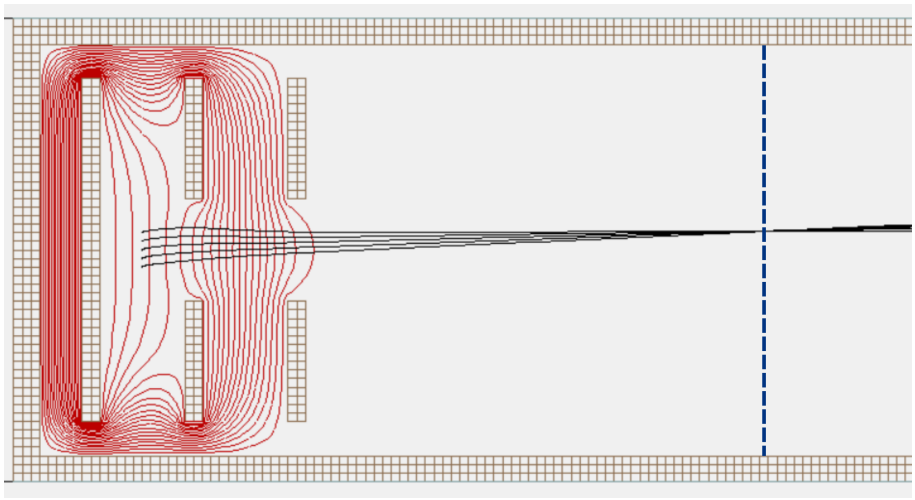

**Figure 2.20:** An illustration of the electric field from a generic three plate VMI to show how particles are focused. The electric field from the VMI (red lines) with example particle flights with the same momentum (black lines). The blue dashed line indicates the focal plane. Figure produced using SIMION version 8.1.

possible to retrieve the 3D distribution using an Abel transform. There are a number of methods to achieve this which are discussed in more detail in section 4.3

## 2.4 Summary

In this chapter we described the experimental set-up used at Southampton to study HHG generation from a SIGC. We also discussed the experimental set-up at the Artemis laser facility for UV and XUV time-resolved photoelectron spectroscopy. We looked at the different laser systems used, the various vacuum system and detector methods for electrons and photons.

The SIGC system is discussed in more detail in chapter 3 which presents results investigating the harmonic flux from the SIGC. The Artemis system is used in chapters 4 and 5 to perform studies on the dissociation of methyl iodide.

# Chapter 3

# Optimisation of High Harmonic Generation from a Semi-Infinite Gas Cell

This chapter discusses the optimal conditions for the highest photon flux of the XUV harmonic closest to 20 eV, looking at the effect of gas pressure, laser power and focal position. The optimisation has focused on the harmonic closest to 20 eV as this is the harmonic used in our TRPES experiments. These experiments are carried out using the laser and vacuum chambers at Southampton which were described in section 2.2. The results can be interpreted using the theory explained in section 1.2.1

## 3.1 Experimental

The spectrometer used for the optimisation of the SIGC is described in greater detail in section 2.2. Briefly, it consists of a 63 cm long SIGC attached to an intermediate pumping chamber and then the detector chamber as shown in figure 3.1. The detector chamber contains a diffraction grating which separates the harmonics onto a position sensitive MCP. Behind the detector is a CMOS camera that records images of the MCP.

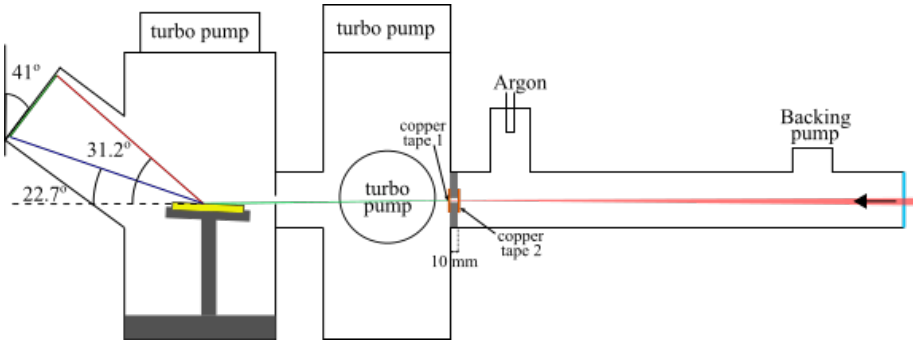


**Figure 3.1:** A schematic of the semi-infinite gas cell and vacuum chambers used to detect the harmonic wavelengths generated. The red line represents the driving laser which is focused a the exit of the cell. The green line represents the high harmonics. The two angles indicated are the minimum and maximum angles which will hit the MCP detector.

The exit aperture of the SIGC has a finite length of 10 mm. Copper tape is always placed on the final exit as indicated by the label "copper tape 1" in figure 3.1. Copper tape is sometimes placed on both sides of the hole, the secondary location is shown also shown in figure 3.1. As the lens is moved, the exact position of the laser on the copper tape changes slightly, which causes the hole to increase in size, thus increasing the pressure in the chambers outside the SIGC. Having two pieces of copper tape reduces this problem allowing for more adjustment of the lens before the copper tape needs to be replaced and a lower working pressure in the middle and detector chamber.

Unless otherwise stated the results have been recorded with an MCP voltage of $-1.28$ kV and phosphor voltage of $+3.17$ kV. These voltages were used as they did not saturate the detector at the highest photon flux measured while still being sensitive enough to detect low harmonic flux. The camera had an exposure of 2.5 s and with no gain. Gain is the amount of amplification the camera applies to the signal, it is a logarithmic scale. Each result is the sum of two images. The intensity of results with the same detector and camera settings can be compared; where the standard settings are not used this should not be done. Unfortunately these results were taken while the FROG to measure the pulse length was broken. The pulse length was optimised on harmonic intensity as

the shortest pulse will result in the greatest amount of harmonics. The laser reliably produces pulses of ∼50 fs. For the application of the XUV photons in TRPES the temporal width of the pulse is important. As the harmonics are only produced during the intense part of the laser pulse the resulting harmonic will have a shorter pulse than the driving laser as demonstrated later in the chapter by figure 3.10 where a 45 fs pulse results in a ∼15 fs harmonic pulse. This means the temporal width of the harmonic is not a concern as it is sufficient for our purpose. This also means the shortest pulses are produced with the shortest driving laser and hence when the harmonics are most intense.

## 3.2 Data Analysis

Figure 3.2 a) shows a typical image which is recorded. This image was taken with a cell pressure of 24.9 mbar and laser power of 1.7 W at the optimal focus position. As the camera is mounted with a small rotation the image is first rotated so that all the harmonics are in a horizontal line, the rotation is usually very small, often about 0.5°. This means the distance between harmonics is given by the x position and allows for a spectrum of harmonic intensity as a function of wavelength to be produced. As background from scattered background light does not depend on wavelength it has to be removed before converting to wavelength. This is done by taking an average of a small area of the image as shown by the white box on figure 3.2 a), avoiding the edges of the detector. This average is then subtracted from every pixel in the image. A strip of the image is then taken, shown by the blue dashed lines, and summed vertically to produce a spectrum of harmonics as shown in figure 3.2 b). We observe 5 first order harmonics shown by the black label and in this example there are also 3 second order diffractions from higher order harmonics shown by the red labels. To know the harmonic order the spectrometer needs to be calibrated as described in the next section. In this example the first order diffractions are the 9th, 11th, 13th, 15th and 17th harmonics. While the

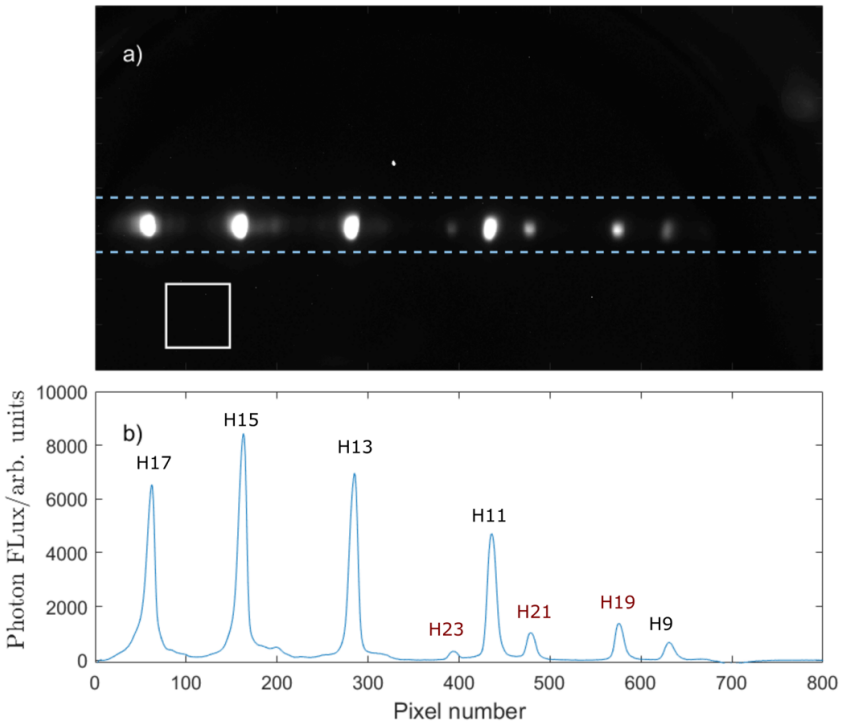


**Figure 3.2:** a) shows a typical image recorded of the XUV spectrum recorded by an AVT-MantaG-235 CMOS camera using the apparatus shown in figure 3.1. The image has already been rotated by $0.5^o$. The white box shows the region which is used to calculate the background. The blue dashed lines show the region which is summed over to produce the harmonic spectrum shown in b). The black labels in b) show the harmonic order of the first order diffraction peaks. The red labels are the harmonic orders of second order diffraction peaks. MCP set at $-1.28$ kV and phosphor at $+3.17$ kV.

three second order diffractions are the 19th, 21st and 23rd harmonic These are usually weaker than the first order diffraction as the grating is designed to maximise first order diffraction, however they are often more intense than the 9th harmonic.

## 3.3 Calibration of Spectrometer

The first task is to calibrate the spectrometer so it is known which harmonics are being detected and thus allowing the images of the harmonics recorded to be converted into wavelength. The wavelengths of the harmonics are known from equation,

$$\lambda_q = \frac{\lambda_0}{q} \tag{3.1}$$

where $\lambda_0$ is the fundamental wavelength, 790 nm, in this case, and $q$ is the harmonic order. The harmonics are diffracted off a grating and about 5 harmonics are at such an angle that they hit the MCP and are recorded by the Manta camera behind the phosphor screen of the MCP, all the other harmonics diffract at an angle that does not hit the MCP. The grating is mounted on a goniometer stage which allows the angle of the grating to change so that it is possible to move the harmonic on the MCP and observe different harmonics. To be able to optimise the SIGC for the harmonic with about 20 eV we need to determine which harmonic is which, as this then allows the pixel position on the image to be converted to wavelength. To do this we use a 0.2 $\mu$m tin filter. The transmission curve for 0.2 $\mu$m for tin is shown in figure 3.3 with the position of harmonics 11, 13, 15 for 790 nm marked on it. Tin only allows 3 harmonics through which means if we are roughly in the correct position we should see two harmonics being blocked when the filter is put into place. We expect to see a transmission of about 9

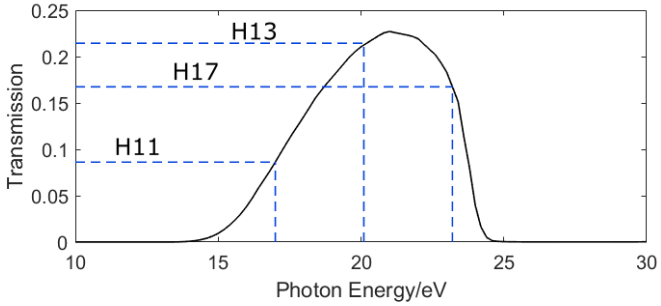


**Figure 3.3:** The transmission curve for a 0.2 $\mu m$ thick tin filter. The dashed lines indicate the location of the 11th, 13th and 15th harmonic of the 790 nm driving laser. Transmission data taken from [121].

% for the 11th harmonic, 21 % for the 13th harmonic and 13 % for the 15th harmonic. As the filters are so thin that it is not uncommon to have a number of small holes in the filter which give rise to a slightly higher transmission than expected.

The filters have a 5 mm clear aperture diameter and are mounted on a metal ring with a diameter of 17 mm. The maximum angle of the light from vertical which would hit the detector is $31^o$ and the minimum angle $23^o$, this means for all the harmonics to fit through the filter it will need to be less than 27 mm from the point of diffraction. The laser hits the grating about 25 mm before the end of the grating. Therefore there is only just enough room to put the filter in before the harmonics are too separated to all pass through the filter and not be blocked by the filter mount which would result in an incorrect identification of the harmonic orders.

The position of the filter after the grating is shown in figure 3.4. A ledge was put below the filter mount which the mount was placed on top of to ensure the height of the filter mount did not change when the filter mount was moving in and out. The mount was placed against the edge of the grating. This meant the position of the filter would be repeatable. A beam block was placed above the filter so that if we observed the harmonics on the detector there was no doubt they must have passed through the filter. To check that all the harmonics would hit the filter a measurement was taken with a broken filter which only had the metal ring mount. All five harmonics were observed so then the tin filter could be added into the setup. Following the addition of the filter, only three harmonics were observed. The spectra of these two images are shown in figure 3.5. The blue spectrum is without the tin filter and the red is with the tin filter, yellow is the same as the red spectrum but with a gain of 40 dB on the camera instead of 20 dB as with the previous images, all images had an exposure of 4 s. 1.4 W of laser power was used in 15 mbar of argon. The MCP was set at $-1.40$ kV and the phosphor screen at $+3.29$ kV

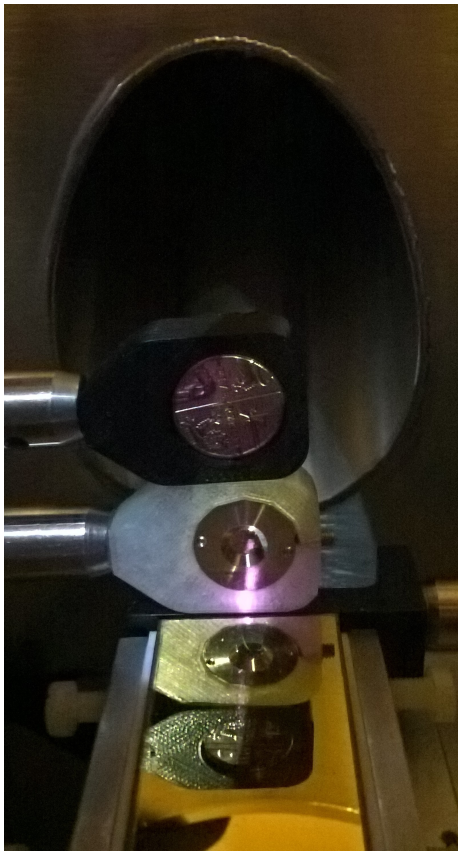

**Figure 3.4:** Image of the diffraction grating with the 0.2 $\mu$m tin filter in the white mount at the end of the grating. Above the filter is a beam block. The zero order diffraction beam can be observed hitting the bottom of the filter mount. The hole behind leads to the MCP.

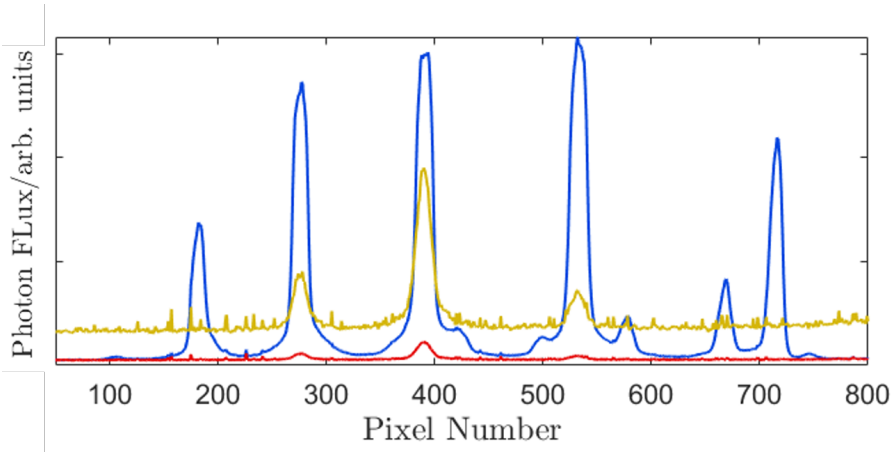


**Figure 3.5:** Blue line: harmonics observed with an empty filter mount. Red line: shows harmonics observed with 0.2 $\mu$m tin filter. Yellow line: is the same as the red line but with the gain on camera increased from 20 dB to 40 dB. All images were taken using 1.4 W with 12 mbar SIGC pressure. Voltages on MCP was $-1.40$ kV and phosphor was $+3.29$ kV. Camera exposure was 4 s.

From figure 3.5 we can be confident that we are detecting harmonics 9-17. The wavelengths of the harmonics are given by equation 3.1. This means we have 5 data points to fit to an equation for wavelength as a function of pixel position.

The first step in the convert from pixel position to the angle of diffraction. With reference to figure 3.6 and the sin rule: $A/sin\alpha = B/sin\beta$, we obtain the equation,

$$\frac{332.7}{\sin(131-\theta)}\sin\theta = \frac{332.7}{\sin(131)\cos\theta - \cos(131)\sin\theta}\sin\theta = V_1 x + C \tag{3.2}$$

where $x$ is harmonic position in pixel number, $V_1$ is the conversion between pixel and length in mm and $C$ is the offset. The value for the hypotenuse is obtained from the geometry of the vacuum chamber. This can then be rearranged to obtain $\theta$ giving us,

$$\cot\theta = \frac{332.7}{\sin(131)}\frac{1}{V_1 x + C} + \cot(131). \tag{3.3}$$

To convert from angle to wavelength we use the diffraction grating equation [116],

$$\frac{d}{m}(\sin(180-\theta_i) - \sin(180-\theta-\theta_i)) = \lambda_q \tag{3.4}$$

where $d$ is the grating separation, in this case $1/1.2\text{x}10^6$. $m$ is the diffraction order, in this case $m$=1. $\theta_i$ is the angle of the incident light. The angle has been assumed to be

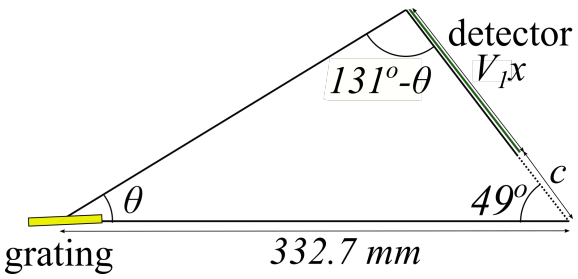


**Figure 3.6:** A simplified geometry of the detector and grating derived from the chamber geometry shown in figure3.1, to allow conversion between position on detector and angle of diffraction. The yellow rectangle shows the location of the grating and the green line the detector.

5.75$^o$, as this is the angle the grating has been designed to work best at. By allowing $V_1$ and $C$ to vary, changing the value $\theta_i$ has no effect on the overall fit. Usually the angle on the diffraction equation is defined perpendicular to the plane of the grating but here it is defined horizontal to the laser table.

When changing axis dimensions it is important to include a Jacobian to keep the area under the graph constant as the initial data is in intensity per pixel and the final data we want to be intensity per nm. As the spectrum is first converted to angle an equation relating $dx$ to $d\theta$ in required. This is done by differentiating the left hand side of equation 3.3 with respect to $\theta$ and the right hand side with respect to $x$. This gives,

$$dx = \frac{332.7(V_1 x + C)^2}{V_1 \text{sin}131} \text{cosec}^2\theta \, d\theta \tag{3.5}$$

which the spectrum is multiplied by when converting to angle. Then to convert to wavelengths a similar process is done with equation 3.4 with the right hand side being differentiated with respect to $\theta$ and the right hand side with respect to $\lambda$. This gives the equation,

$$d\theta = \frac{m}{d} \text{sec}\theta \, d\lambda \tag{3.6}$$

which the spectrum is multiplied by when converting to wavelength.

Now that the spectrometer is calibrated it is possible to convert from pixel to wavelength using the pixel position of the first order diffractions. Figure 3.7 shows the spectrum in figure 3.2 as a function of wavelength without the Jacobian in the red dashed line and with the Jacobian included in the solid black line. Both spectra have the same area. As the conversion between pixel and wavelength is almost linear there is very little difference between the two spectra. The insert shows the 13th harmonic zoomed in to show there is a difference between the two spectra. All data presented from this point onwards have the Jacobian included.

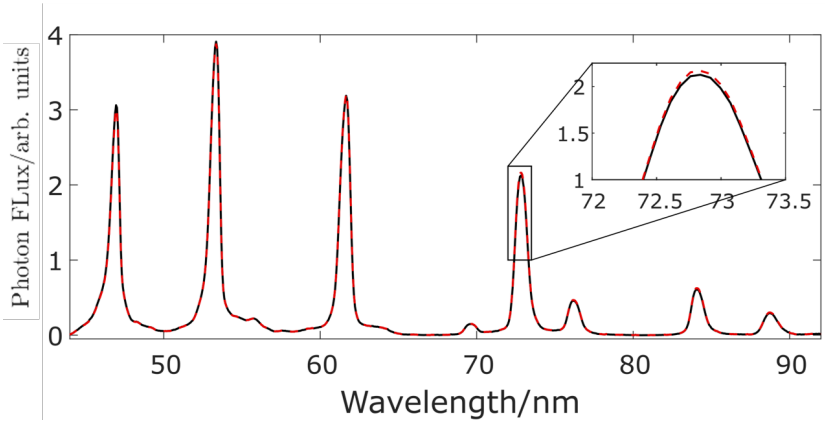


**Figure 3.7:** The harmonic spectrum from figure 3.2 as a function of wavelength with and without the Jacobian included shown by the red dashed line and the black solid line respectively. The insert shows the a zoomed in section of the graph indicated by the black box to show the difference between the two spectra. Both spectra have the same area. MCP set at $-1.28$ kV and phosphor at $+3.17$ kV.

## 3.4 Focusing Conditions

The laser is focused by an uncoated N-BK7 plano-convex focusing lens with a 75 cm focal length on a translation stage. As the harmonics are generated near the focus it is important to understand how the beam is focused in the experiment. To do this the SIGC was removed and a mirror was added which reflected the beam at $90^o$ to extend the beam path. Using a CMOS camera with a pixel size of 5.2 $\mu$m and neutral density (ND) 13 filter a series of images of the beam spot were taken with the lens at a range of different positions. The laser power was reduced to about 70 mW, to any stop non-linear effect due to focusing in air. For each position the images were then fitted to a 2D Gaussian to calculate the beam width in the X and Y axis for each image. Figure 3.8 shows the beam waist in X axis (red) and Y axis (blue). The focus is tighter in the Y axis and is not symmetric, this is likely due to a small amount of clipping which occurs in the Spitfire as the laser pulse exits the laser cavity. The beam focus has been defined as the position with highest intensity. To provide a model of the focus conditions for further calculations the data was fitted to a 4th order polynomial as this provided a good fit. The 4th order fits are shown in figure 3.8 by the solid lines.

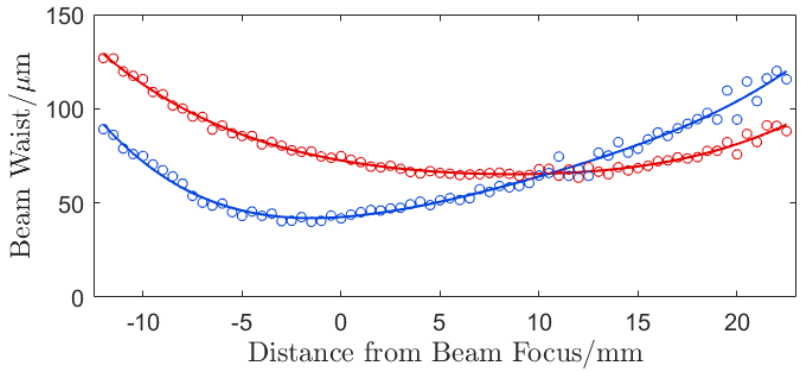


**Figure 3.8:** The beam waist of the laser through its focus in the x axis (red circles) and y axis (blue circles). The beam waist is defined as the FWHM. The zero position of the beam focus is defined as the beam spot with the smallest areas. The solid lines are the 4th order polynomial fits.

Using the best fit curves it is then possible to calculate the self phase modulation length of the laser as a function of focus position. The non-linear phase shift is given by,

$$\Delta\Phi = \frac{n_2 \omega I_0 L}{c} \tag{3.7}$$

where $n_2$ is the non-linear coefficient, $\omega$ is the angular frequency, $I_0$ is the intensity and $c$ the speed of light. When $\Delta\Phi$ is 1, $L$ is the self phase modulation length which is the point that non-linear effects should be considered. For Argon at 1 bar $n_2$ ≈1.5x10$^{-23}$ m$^2$W$^{-1}$ [122, 123], as $n_2$ is linear with respect to pressure we can calculate the value at different pressures. It is important to calculate the self phase modulation length to check that we have no unexpected focusing condition as the laser travels through the filled gas cell. In figure 3.9 we plot the result of this calculation for two pressures corresponding to our "normal" operating pressure (20 mbar), and a significantly higher pressure (60 mbar). The Rayleigh length is 25 nm for our focusing conditions. As we can see from figure 3.9 the self phase modulation length is 33 mm at the focus for 20 mbar, larger than the Rayleigh length. At 60 mbar it is 11 mm at the focus which would mean non-linear effects need to be considered. However, as the majority of the results are taken at around 20 mbar the non-linear effect will not have any effect on the overall results.

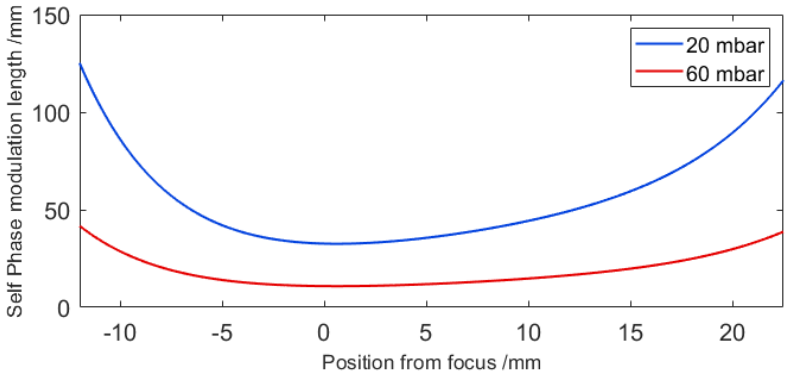


**Figure 3.9:** The self phase modulation length for the laser along the focus at 20 mbar (blue line) and 60 mbar (red line). The zero position of the focus is defined as the smallest spot size.

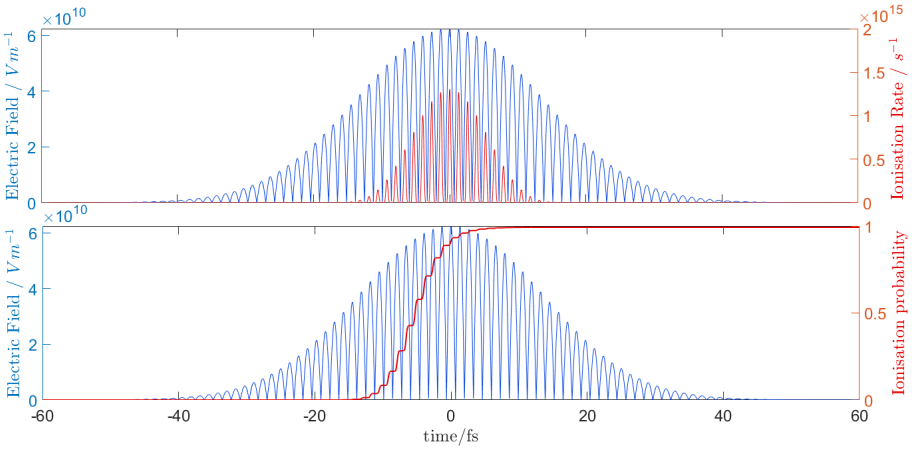


**Figure 3.10:** The blue line in both figure shows the magnitude of the real component of the electric field for a 1.4 mJ, 45 fs pulse with a spot radius of 30 $\mu$m. In a) the red line shows the ADK ionisation rate. In b) the red line shows the ionisation probability.

The other helpful calculation is to calculate the ADK ionisation rate and ionisation fraction using equations 1.20. ADK ionisation has previously been discussed in detail in section 1.2.1. Figure 3.10 a) shows the ADK ionisation rate in red for the 45 fs laser pulse shown in blue. The intensity of the laser pulse has been calculated using 1.4 mJ and a simple top-hat function for a spot with a radius of 30 $\mu$m which is equivalent to the smallest spot size in our set-up. Figure 3.10 b) shows the same pulse but with the ionisation fraction in red. You can see in this case a large fraction of atoms are ionised by the time of maximum intensity of the pulse demonstrating near the focus we are

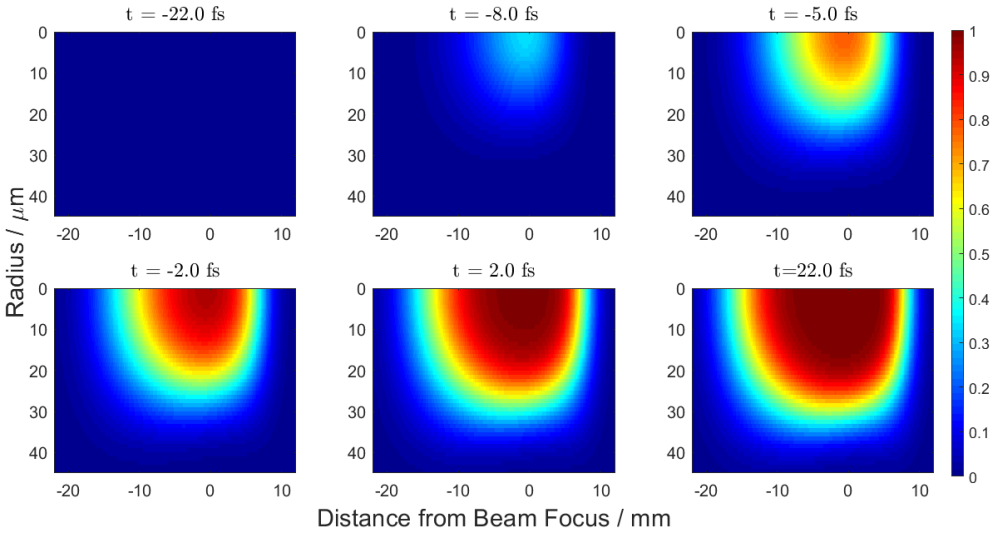


**Figure 3.11:** The ADK ionisation probability as a function of radius and focus of the beam at 6 different time positions. The first image is before any ionisation has occurred while the final image is after all ionisation has occurred. $t$ =0 fs is the centre of the laser pulse. As the laser spots are not perfect circles the average intensity at each radius was used for the ionisation calculation.

producing harmonics from the earlier parts of the pulse. Further away from the focus where the intensity is lower more ionisation will happen during the centre of the pulse where the intensity is higher. To investigate how the rate of ionisation varies depending on the focus of the laser and radial position ADK calculations were also carried out on a more complex model.

Figure 3.11 shows the ionisation fraction for different parts of the focus using the equations from figure 3.8. Again the simulations have used a 45 fs, 1.4 mJ pulse, however a 2D Gaussian had been used to calculate the intensity. As the laser spot is not symmetrical the average intensity at each radius has been calculated. The ionisation fraction is calculated for each radius and position along the beam focus. The ionisation model used does not include ionisation of $Ar^+$ which would reduce the population of the cation reducing HHG production. The IP of the cation is significantly larger so is less likely to ionise but some ionisation is still likely to be present. Time zero is defined as the centre of the laser pulse. As shown in figure 3.10 we again observe, at small radii near the focus

a large fraction of atoms have already been ionised before $t$ =0 fs. However at large radii or away from the focus we observe a significant amount of ionisation near the centre of pulse ($t$ =0 fs) which is clear from comparing the plot at $t = -2$ fs with the one at $t$ =2 fs. The most important observation is that there is very little ionisation at when the laser is $-20$ mm away from the focus or 10 mm past the focus. As ionisation is required for harmonic generation this means the there will be no generation of harmonics on gas which is either $< -20$ mm or $>$10 mm from the focus. When considering the effect of the ADK ionisation faction it is important to remember that good phase matching is not achieved at the focus due to Gouy phase shift.

## 3.5 Results and Discussion

The section presents the optimisation curves for the SIGC for the focus position, gas pressure and laser power. Optimisation has focused on the harmonic flux of the 13th harmonic of 790 nm which is 60.8 nm (20.4 eV) as this is the harmonic used in our time-resolved photoelectron spectroscopy experiments.

Initially all the optimisation of the SIGC was done using two pieces of copper tape at the exit of the SIGC as this resulted in a lower pressure in the detector chamber. However we observed some surprising behaviour in the effect of the focus position similar to that in figure 3.14 which we thought may be due to trapping gas between the two pieces of copper tape. Hence we repeated all experiments with both two pieces of copper tape and one piece at the final exit of the SIGC.

The error on the measured harmonic intensity is approximately $10\%$ (1 standard deviation), this has been calculated from stability scans which takes two images every minute for about 36 mins. This is about the time it takes to collect a complete data set investigating a single variable, e.g. the data required for a single graph. The results from a

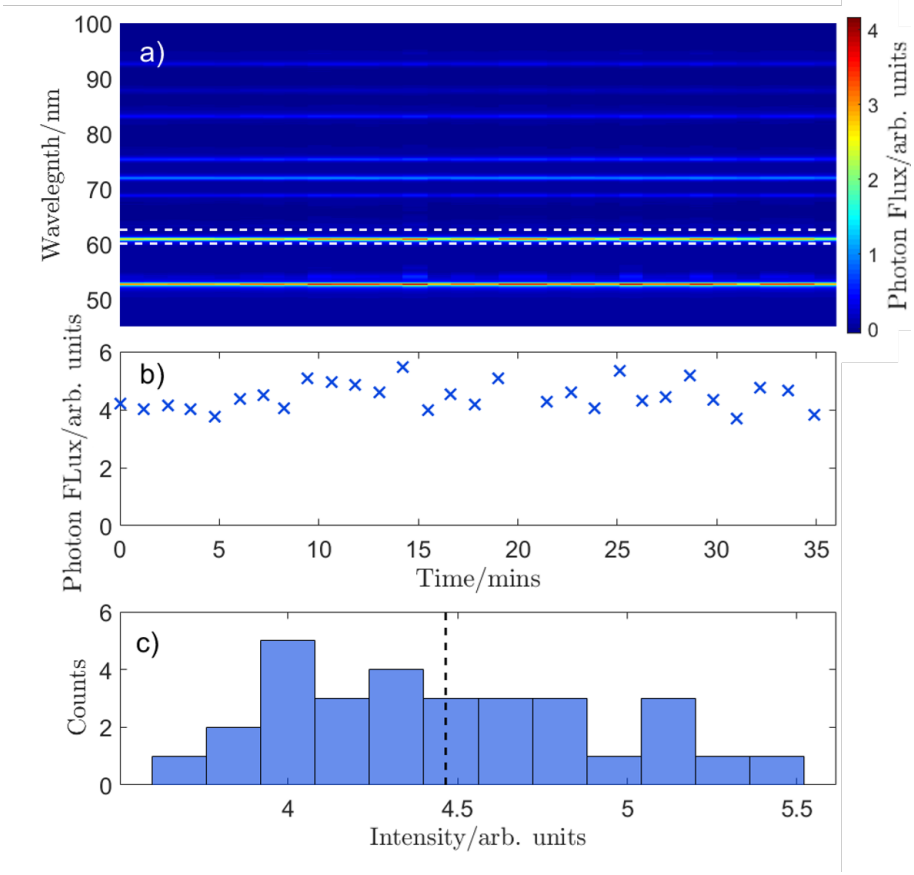


**Figure 3.12:** a) variation over 36 mins with results recorded about every minute at 20 mbar and 1.71 W of all harmonics observed, b) summed over the region shown by the dashed white lines in a) showing the stability of the 13th harmonic flux. c) shows a histogram of the intensities of the 13th harmonic, with the dashed black line indicated the mean value.

stability scan with a cell pressure of 20 mbar and 1.71 W are shown in figure 3.12. This scan was taken at typical experimental conditions and shows no long term variations.

### 3.5.1 Effect of Focus Position

The first experiment investigated the effect of the focus position of the fundamental on the harmonic intensity. This was done by moving the lens in 0.5 mm steps. To keep the exit hole size constant during the scan the lens was moved the completed distance before recording any results. The results from these scans are shown in figure 3.13 and figure 3.14. In both figures a) shows the sum over the region shown in figure 3.2 for different lens positions, b) shows the harmonic intensity for the 13th harmonic, taken by

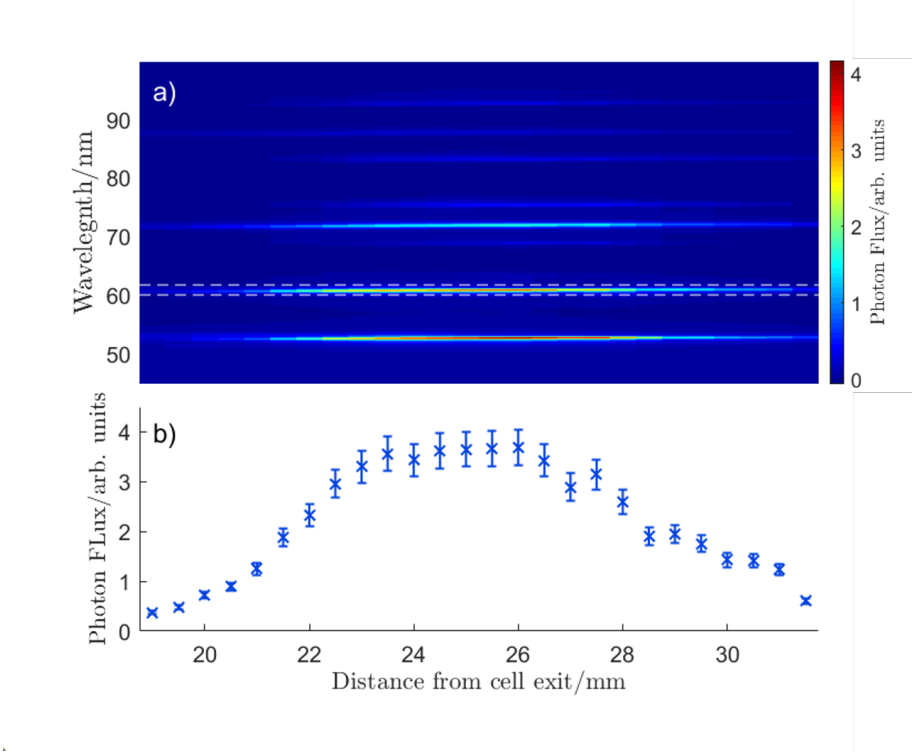


**Figure 3.13:** The effect of focus position on harmonic intensity for laser power of 1.7 W and cell pressure of 20 mbar with two pieces of copper tape on the exit. a) shows the colour map showing 4 harmonics. White dashed lines indicate the region which is summed to produce the graph in b). Positive distances means the focus is outside the cell. MCP set at $-1.28$ kV and phosphor at $+3.17$ kV. Error bars show 1 standard deviation calculated from the stability scan.

summing over a wavelength region 60.0-61.7 nm as shown by the white dashed lines in a). The x-axis in figures 3.13 and 3.14 is the position of the focus of the laser relative to the end of the exit aperture of the gas cell, positive distance means the focus of the driving laser is outside the gas cell. The relationship between the lens position and focus position was determined by taking images of the focus as described in section 3.4.

Figure 3.13 and figure 3.14 were both taken with SIGC filled with $20.0\pm0.2$ mbar of argon. A laser power of $1.70\pm0.1$ W before the lens was used. The error in cell pressure and laser power is from the fluctuations in the pressure gauge and power meter respectively. As previously stated in chapter 2, about 13% of the power is lost on the lens and SIGC window, so power in the gas cell would be around 1.48 W. The difference between

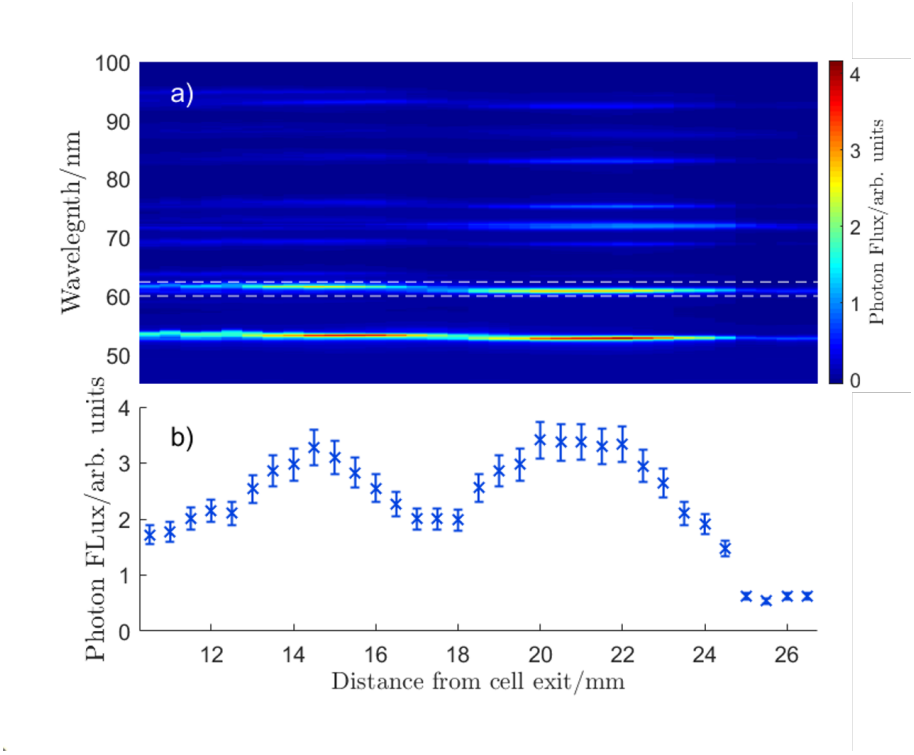


**Figure 3.14:** The effect of focus position on harmonic intensity for laser power of 1.7 W and cell pressure of 20 mbar with one piece of copper tape on the exit. a) shows the colour map showing 4 harmonics. White dashed lines indicate the region which is summed to produce the graph in b). Positive distances means the focus is outside the cell. MCP set at $-1.28$ kV and phosphor at $+3.17$ kV. Error bars show 1 standard deviation calculated from the stability scan.

the two graphs is that figure 3.13 has two pieces of copper tape on the exit whereas figure 3.14 only had one piece of tape. Figure 3.13 b) shows a single maximum from 23.5-26 mm with a maximum intensity around 3.6. This is a surprisingly large range where harmonic intensity is constant. When the focus is 23.5 mm outside the cell we are seeing significant harmonic intensity. If we are generating on gas at the exit of the cell the laser at the point of generation would be $-23.5$ mm away from its focus. Referring back to figure 3.11 which shows the ADK ionisation fraction, by $-22$ mm there is very little ionisation, at the centre there is less than 4% ionisation at 22 fs. Therefore we would expect even less ionisation to occur $-23.5$ mm away from the focus and ionisation is required for harmonic generation. Therefore even though there may be a very small variation in the location of the focus due to focusing through a gas we can be confident

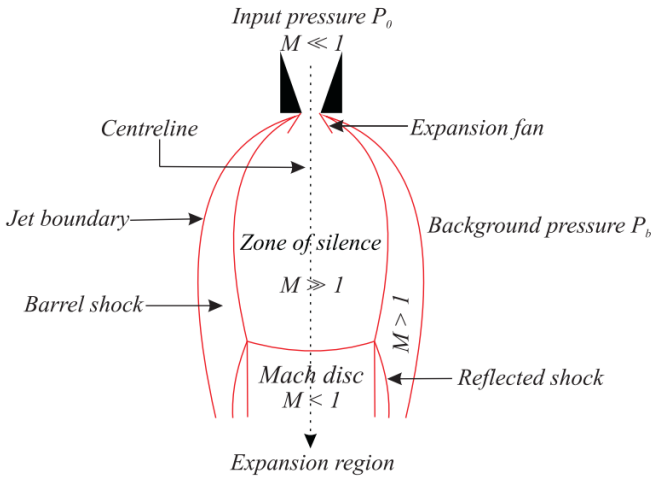


**Figure 3.15:** Diagram of free jet expansion from a nozzle. After the exit from the high pressure nozzle into a lower pressure region there is initially a low density region called the zone of silence after which a Mach disk is formed which has a high gas density. Adapted from [124]

that harmonics are not being generated near the exit of the cell but outside the cell, likely on a Mach disk that is closer to the focus.

At the exit of the gas cell a gas jet will be formed as the gas moves from a region of higher pressure to a region of lower pressure. The cell has a pressure of about 20 mbar while the pumping chamber which the gas moves to has a pressure of about 4x10$^{-3}$. The structure of the gas jet formed is shown in figure 3.15. The first region after the cell exit is known as the zone of silence. This region is characterised as having a very low pressure and rapid expansion. The second region is known as the Mach disk and has a high density, meaning it may be possible to generate harmonic using the gas in the Mach disk. And larger pressure differences multiple Mach disk can be formed.

### 3.5.2 Effect of the Copper Tape

Figure 3.14 is similar to figure 3.13, with the same experimental conditions except it only has one copper tape on the exit hole. Figure 3.14 shows a different behaviour to figure 3.13, with two maxima one at 14.5 mm and a second one from 20.0-22.0 mm.

The maximum intensity is again around 3.4. For the maximum at 20.0-22.0 mm we can again be confident we are generating outside the cell. The peak observed when the laser is focused 14.5 mm outside the gas cell corresponds to the laser being −14.5 mm away from the focus at the exit of the gas cell. Figure 3.11 shows the ionisation expected from laser −14.5 mm from the focus. There is about 60% ionisation at radii of less than 1 mm. As there is still significant ionisation at −14.5 mm it is possible the maximum at 14.5 mm is due to harmonics generated at the exit of the gas cell. The ratio of the harmonic intensity of the two peaks at 14.5 mm and 21 mm depends on the energy of the harmonics with higher energy harmonic having a higher ratio of intensity at 14.5 mm to intensify at 21 mm. This makes sense as shorter wavelengths are absorbed less so a higher percentage of harmonics generated at the cell exit will travel through the

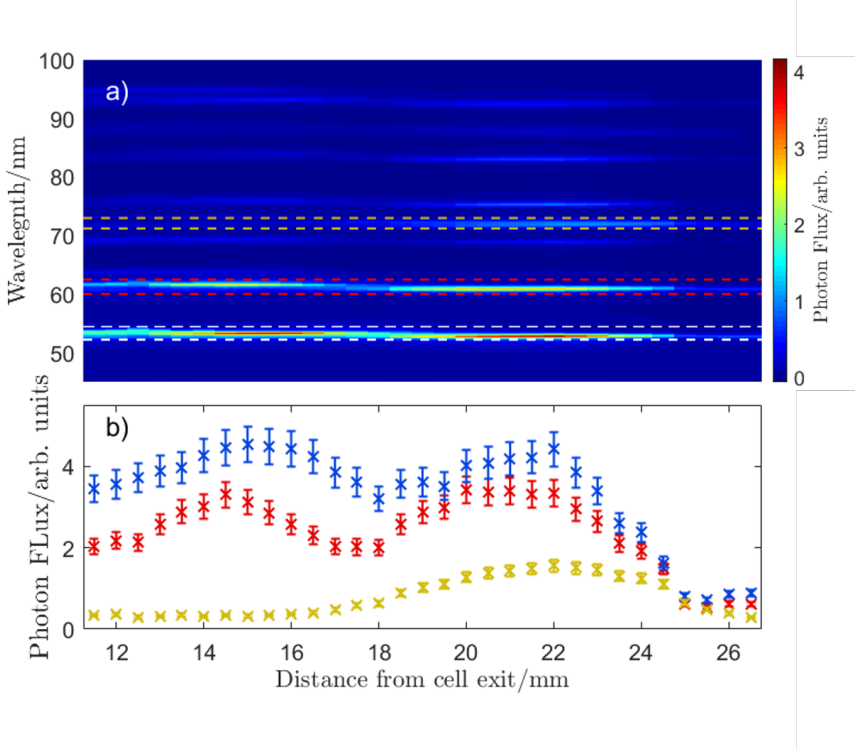


**Figure 3.16:** Same data as figure 3.14 but with harmonic intensity lineout for three harmonics. Blue data is harmonic 15, red is harmonic 13 while yellow is harmonic 11. The regions summed over in a) to produce the lineouts in b) are shown by dashed lines of the same colour expect the blue data is indicated by the white dashed lines. MCP set at −1.28 kV and phosphor at +3.17 kV. Error bars show 1 standard deviation calculated from the stability scan.

Mach disk. This is shown in figure 3.16 which shows the same data as in figure 3.14, but this time integrated over the 11th (yellow), 13th (red) and 15th (blue) harmonics. The wavelength regions summed over are 52.2-53.4 nm (11th), 60-62.2 nm(13th) and 71.2-73.0 nm (15th) as shown by the dashed white line in a). The 11th harmonic is only generated outside the cell. As previously discussed the 13th harmonic is generated equally at both positions. The 15th harmonic has a slightly higher intensity at the peak closer to the gas cell.

At first glance then it appears the copper tape is not affecting the harmonic intensity but does affect the relationship between the focus position and the harmonic flux production. This is likely due to the gas structure near the exit. Figure 3.17 shows the

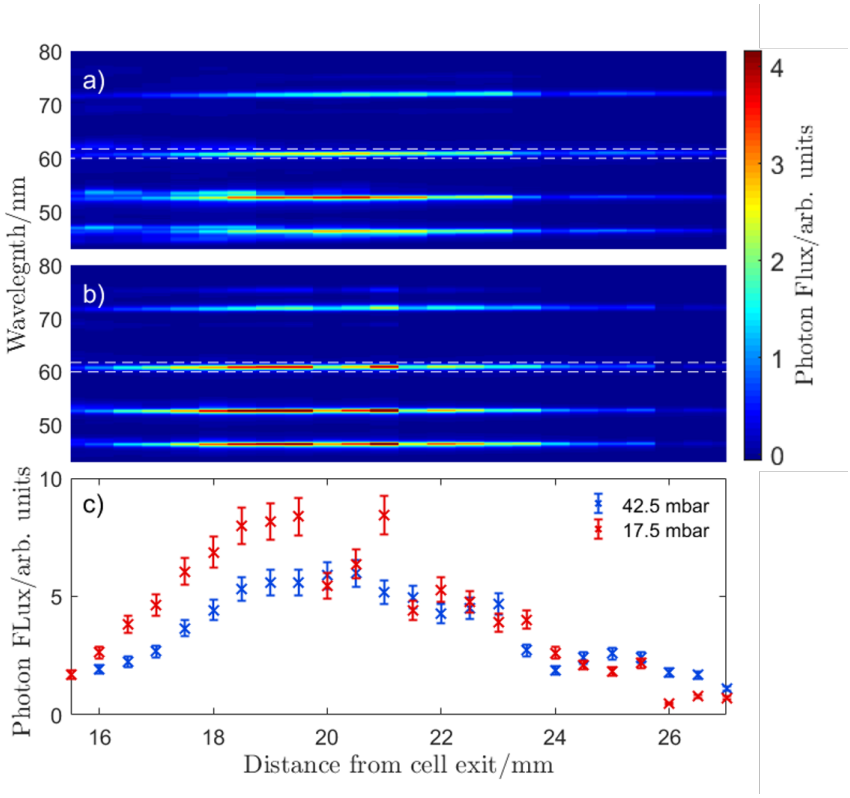


**Figure 3.17:** a) and b) show the harmonic intensity dependence on focus position with a laser power of 1.70 W. a) has a cell pressure of 42.5 mbar while b) is 17.5 mbar. The white dashed lines show the wavelengths summed over the produce the graph in c). MCP set at $-1.28$ kV and phosphor at $+3.17$ kV. Error bars show 1 standard deviation calculated from the stability scan.

harmonic intensity as a function of focus position at a laser power of 1.70 W for two pressures with a single piece of copper tape over the exit. Results were recorded in steps of 0.5 mm. Figure 3.17 a) shows the all harmonics observed at 42.5±0.3 mbar and b) at 17.5±0.1 mbar. The white dashed lines in figure 3.17 a) and b) show the wavelength region (60.0-61.7 nm) which has been summed over to produced the graph in c) which shows the intensity of the 13th harmonic. Again we observe a single peak similar to that with two copper tapes but these results are with a single piece of copper tape. Unfortunately there appears to be more noise than usual on the 17.5 mbar data. However we can still see that, firstly, changes in pressure in the ranges used with the experiments does not affect the ideal position of focus and secondly, both a single peak or double peak can be observed when using just a single piece of copper tape. In preliminary results with equivalent conditions to the earlier plots the double peak focus position dependence was exclusively observed with two copper tapes. The cause of this change in behavior is not clear, it is possible changes in alignment caused changes in the size of the exit hole or that changes in pulse compression had a significant effect on the phase matching conditions that caused the difference between the results.

When gas moves from a region of higher pressure to a lower pressure, it expands rapidly, creating a shock wave known as the Mach disk as shown in figure 3.15. Just after the exit hole there is a low density, high velocity region known as the zone of silence after which there is a Mach disk which is the densest region. If the ratio between the two pressure regions is high enough multiple Mach disks can be formed. The distance of the first Mach disk from the exit of the SIGC can be estimated by [125],

$$X_m = 0.67d\sqrt{\frac{P_0}{P_b}} \tag{3.8}$$

where $d$ is the diameter of the exit, which is about ∼100 $\mu$m, $P_0$ is the SIGC pressure, and $P_b$ is the background pressure which is about 4x10$^{-3}$ mbar. This gives a value of

5 mm. The distance between the first maximum and the start of the second maximum in figure 3.14 is 5.5 mm, this is a good agreement especially given the uncertainty on both the values for $d$ and $P_b$ used and that we may not be generating off the same laser focus position due to different pressures and phase matching conditions for the two regions. Therefore it seems a good conclusion that we are generating on the first Mach disk at the larger distance from the gas cell ($>$20 mm). Having a smaller exit hole also results in a smaller background pressure, however, the smaller exit hole size is going to be a greater effect on the distance to the Mach disk, decreasing the distance. Why decreasing the distance would result in two maxima is not clear. Potentially the smaller exit hole results in a higher pressure at the very exit of the cell allowing for good harmonic generation both at the exit of the cell and the Mach disk. Equation 3.8 seems to suggest that increasing cell pressure would move the location of the Mach disk significantly which would affect the location of the ideal focus, fortunately figure 3.17 shows this isn't the case. This is likely because increasing the cell pressure also increases background pressure counteracting some of the effect of the increased pressure meaning $P_0/P_b$ doesn't change much and the large region where good phase matching is achieved.

### 3.5.3 Effect of Gas Pressure

Figure 3.18 shows the gas dependence of the 13th harmonic at 3 different laser powers for the gas cell with 2 pieces of copper tape. The position of the focus was 25 mm outside the cell as this was the centre of the maximum determined by figure 3.13. In this experiment the copper tape was replaced at the start and the lens was not adjusted to keep the exit hole as small as possible. In figure 3.18, with two pieces of copper tape at the exit of the gas cell, the maximum harmonic intensity occurs around 17.5 mbar for all laser powers. The harmonic intensity is very similar for 1.70 and 1.90 W but is significantly lower for 1.49 W. The maximum intensity recorded is about 3.6 which occurs at the same conditions as the same maximum in figure 3.13. There is a sharp increase in intensity before the maximum, after the maximum the intensity decreased

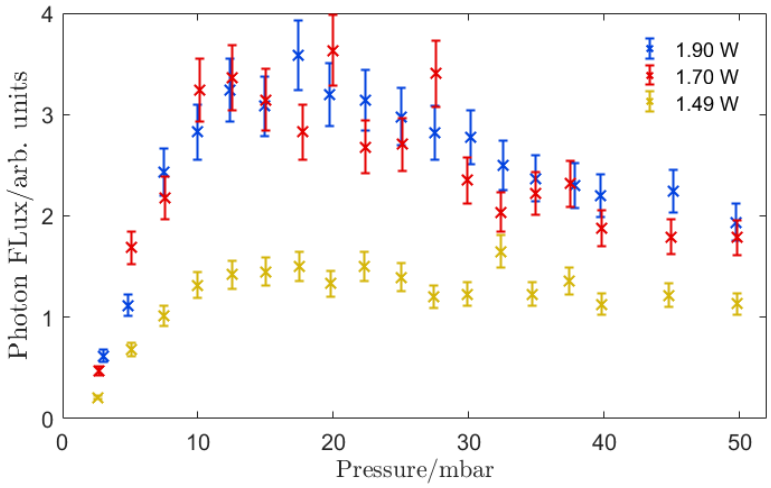


**Figure 3.18:** The effect of gas pressure on 13th harmonic intensity at 3 different laser powers. Cell exit had 2 pieces of copper tape. The focus was at 25 mm outside the gas cell. MCP set at −1.28 kV and phosphor at +3.17 kV. Error bars show 1 standard deviation calculated from the stability scan.

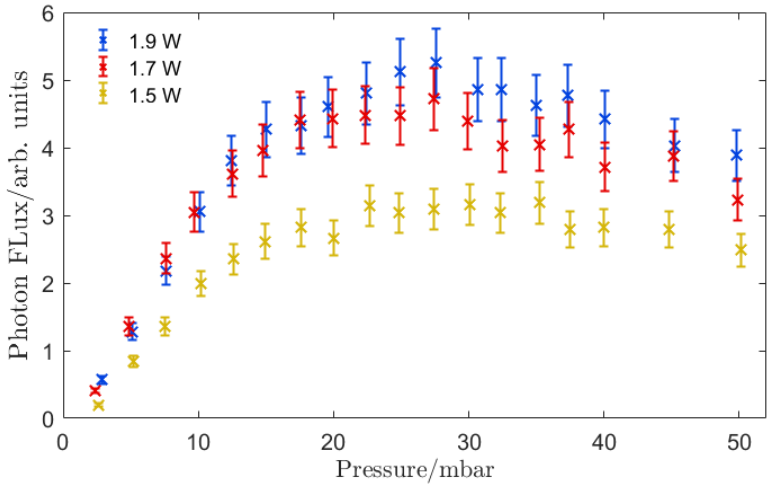


**Figure 3.19:** The effect of gas pressure on 13th harmonic intensity at 3 different laser powers. Cell exit had 1 piece of copper tape. The focus was at 21 mm outside the gas cell. MCP set at −1.28 kV and phosphor at +3.17 kV. Error bars show 1 standard deviation calculated from the stability scan.

more slowly for 1.90 and 1.70 W. For 1.49 W the intensity stays roughly constant.

Figure 3.19 shows the gas pressure dependence of the 13th harmonic at 3 different laser powers for the gas cell with 1 piece of copper tape. The position of the focus was 21 mm outside the cell as this was the centre of the maximum determined by figure 3.14.

Again the copper tape was replaced at the start of each measurement and the lens was not moved during the scan. The maximum harmonic intensity occurs around 22.5 mbar for 1.5 W and 1.7 W, the maximum appearing slightly later at 27.5 mbar for 1.90 W, however this may just be due to harmonic fluctuation. The harmonic intensity is very similar for 1.70 W and 1.90 W but is lower for 1.49 W. The maximum intensity recorded is about 5.3. Compared to the previous measurements shown in figure 3.13, the data point at 1.70 W and 20.0 mbar has an intensity of 4.4, which is very slightly outside error for the previous result in figure 3.13, however as it is only slightly larger than expected this may be due only to a smaller exit hole and therefore lower background pressure and reduced absorption of harmonics. There is a sharp increase in intensity before the maximum, after the maximum the intensity decreased more slowly for 1.90 and 1.70 W. For 1.49 W the intensity stays roughly constant.

There are two clear differences between the results in figure 3.18 and 3.19 which differ in the number of pieces of copper tape at the exit, two and one respectively. The first being the rise and subsequent decrease in harmonic intensity is much slower for figure 3.19 than in figure 3.18. The other being the relative intensity of the harmonic at $\sim$1.5 W compared to those at 1.70 and 1.90 W is much lower in figure 3.18.

As we are generating outside the SIGC we do not know the gas pressure at the region where we are generating. It appears that the pressure at the Mach disk may be increasing more rapidly for figure 3.18 than for figure 3.19 as we reach the point when absorption dominates and harmonic intensity starts to decrease at a lower SIGC pressure. This seems slightly surprising given the exit hole is larger for figure 3.19 as this result only had one piece of copper tape however it potentially results in more gas in the background and not directed to the Mach disk. It is also possible there is more movement of the location of the Mach disk for figure 3.18 as $P_b$ will not increase as much relative to $P_0$ which from equation 3.8 we see will cause greater movement in the location of the Mach

disk. However figure 3.17 seems to indicate change in SIGC pressure has a limited effect on the ideal lens position.

### 3.5.4 Effect of Laser Power

Figure 3.20 shows the laser power dependence of the 20 eV, 13th harmonic at 3 different cell pressures for the gas cell with 2 pieces of copper tape. The position of the focus was 25 mm outside the cell as this was the centre of the maximum determined by figure 3.13. Initially the harmonic intensity increases with laser power and then flattens out for higher pressures. At 30 mbar the plateau starts at 1.6 W whereas for 10 mbar this happens a lot later at about 1.9 W with 20 mbar being in the middle around 1.8 W. Again the intensity at 1.7 W and 20 mbar is around 3.7, showing consistency between the three different results shown in figure 3.13 and figure 3.18.

Figure 3.21 shows the laser power dependence of the 20 eV harmonic at 4 different cell pressures for the gas cell with 1 piece of copper tape. These were the last results obtained and it appears there was a slight change in the alignment which resulted in a significant increase in harmonic intensity. This meant the MCP was reduced from $-1.28$ kV to $-1.22$ kV to stop the detector from saturating. As the realignment caused a change in the focusing of the beam, the lens dependency scan was repeated. It showed a similar behaviour to figure 3.14 however the position of the lens on the stage was 6 mm closer to the SIGC. As the laser still passed through the exit of the SIGC without any realignment the change in the laser pointing must have been small. The reason why the harmonics were so much more intense is not clear. It may be due to better selection of the centre of the harmonic with the pinhole before the diffraction grating or the beam hitting the diffraction grating differently. As the FROG was broken it was not possible to measure the pulse length and therefore it is possible that an alignment change in the Spitfire may result in improved pulse compression. However this would be unusual as the

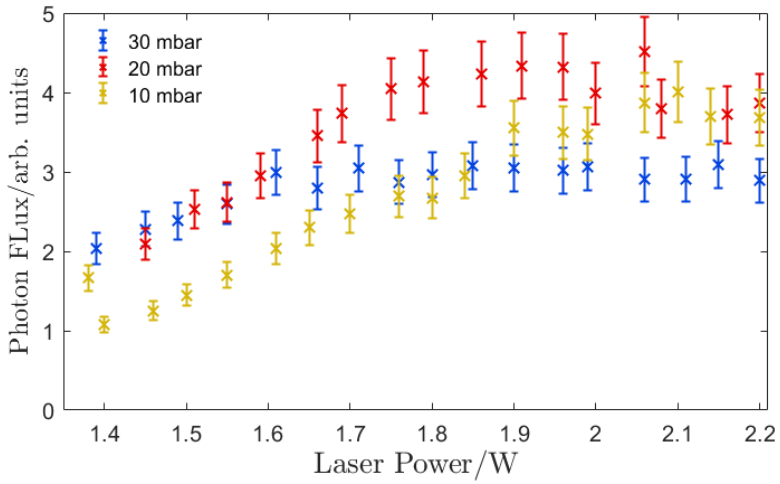


**Figure 3.20:** The effect of laser power on the 20 eV harmonic intensity at 3 different cell pressures. Cell exit had 2 pieces of copper tape. The focus was at 25 mm outside the gas cell. MCP set at −1.28 kV and phosphor at +3.17 kV. Error bars show 1 standard deviation calculated from the stability scan.

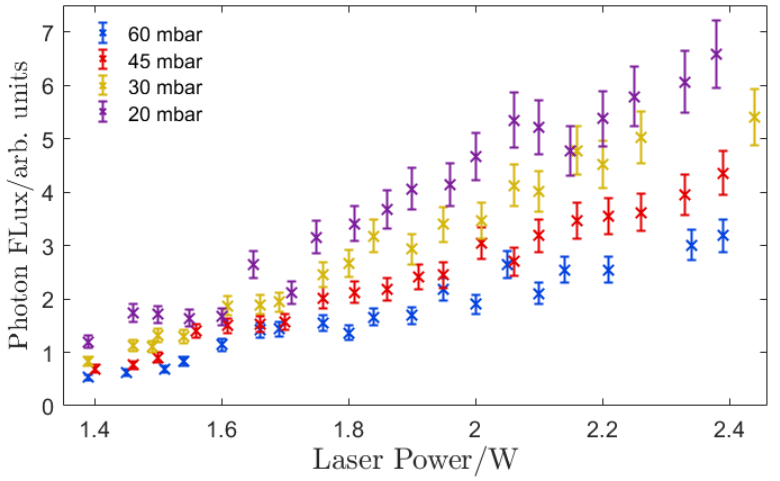


**Figure 3.21:** The effect of gas pressure on 20 eV harmonic intensity at 4 different laser powers. Cell exit had 1 piece of copper tape. The focus was at 26 mm outside the gas cell. MCP set at −1.22 kV and phosphor at +3.17 kV. Error bars show 1 standard deviation calculated from the stability scan.

Spitfire has been aligned to reduce the pulse length any change in alignment normally results in a longer pulse length.

Figure 3.21 shows a linear increase of harmonic intensity with laser power. We also see that higher pressure results in less harmonic for all laser powers. This fits with figure

3.19 which shows a maximum intensity around 20 mbar and a decrease at higher pressure.

Increasing laser power increases the amount of ionisation in the gas and hence increases the harmonic intensity. However it is possible to reach an electron plasma density where the gas becomes opaque to the fundamental. Increasing the intensity also has a significant effect on the phase matching of the system. From equation 1.43 we see that increasing laser power will increase the atomic phase mismatch. However if we are generating on the Mach disk this term will be negligible. As the ionisation fraction ($\eta$) will increase both the neutral atom and the free electron phase mismatch will change. From equation 1.36 we can see the magnitude of the neutral atom term decreases, while from equation 1.40 we can see the free electron phase mismatch increases. As the free electron term is the only negative term in the phase mismatch equation increase the intensity is likely to lead to worse phase matching conditions for the harmonics.

We appear to have reached the limit of increased ionisation resulting in more harmonics for figure 3.20 while this limit is not reached for figure 3.21. Why we would obtain the two different graphs when the only obvious difference between the two results is the size of the exit hole is not clear. However given the surprising increase in harmonics for figure 3.21 some scepticism about how much they can be compared to all the previous results would be advised.

## 3.6 Harmonic Generation from 395 nm

As explained in section 1.2.1.5 using a shorter wavelength results in a significant increase in the conversion efficiency therefore we expect a significant increase in harmonic intensity. To generate 395 nm a BBO crystal is used, with which we are able to generate a maximum of around 0.580 W of 395 nm from maximum laser power around 2.3 W

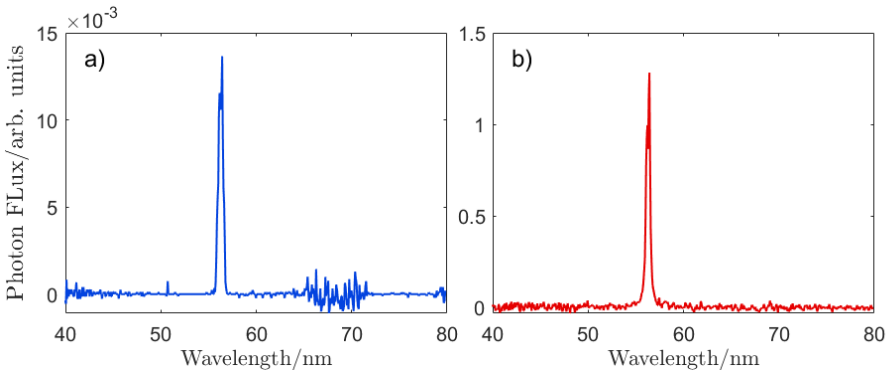


**Figure 3.22:** The 7th harmonic of 395 nm generated from 15 mbar of argon using 0.58 W. MCP voltage was −1.30 kV and phosphor was +3.20 kV. a) has no gain while b) has a gain of 40 dB on the camera.

The 395 nm and 790 nm are separated by two long pass mirrors. This means less than 2% of the power is due to 790 nm light and therefore should not cause an issue for generating harmonics.

As we are observing the 9th to 15th harmonic from 790 nm we'd expect to see the 5th and 7th harmonics of 395 nm (10th and 14th harmonic of 790 nm). Figure 3.22 a) shows a spectrum taken using 0.58 W of 395 nm in 15 mbar of argon. The MCP voltage was −1.30 kV and that phosphor was at +3.20 kV. We only observe a single harmonic which is the 7th harmonic. The intensity of the harmonic is also very weak, two orders of magnitude lower than those observed at 790 nm. Figure 3.22 b) is the same image but with a gain of 40 on the camera to show clearly that harmonic is not due to dead pixels or noise.

It is suspected that the reason that significant harmonics from the 395 nm is not generated is due to the pulse having to pass through the lens which is 3.9 mm thick in the centre causing the pulse to lengthen. At 790 nm this effect could be compensated for by the pulse compression inside the Spitfire. As a short pulse is also required to efficiently generate the 395 nm it is not possible to have a short pulse length at both the BBO and the exit of the SIGC with a lens in between these two points. Therefore the next step would be to change the lens to a focusing mirror. Unfortunately there wasn't enough

time to achieve this within this project.

## 3.7 Outlook

The experiments in this chapter have investigated the potential use of an argon filled semi-infinite gas cell for a source of HHG for time-resolved photoelectron spectroscopy (TRPES). The most suitable energy for the TRPES experiments we perform is about 20 eV and therefore this chapter has focused on the generation of the 13th harmonic of 790 nm (20.4 eV)

This chapter has shown the optimisation curves for harmonic flux using 790 nm in a SIGC with argon for focus position, cell gas pressure and laser power. Two different dependencies on focus position were observed, either a single harmonic maximum with the focus about $\sim$25 mm outside the SIGC or two maximums, one around 15 mm and another about 21 mm outside the SIGC. The different behaviour appeared to be due to different exit hole sizes, with the larger holes resulting in a single maximum. The measurements also show that the optimal position is to generate on a Mach disk outside the SIGC and hence the SIGC acts like an in-line gas jet. This means that while it is a SIGC, it is not operating like one. The harmonic flux rapidly increases with pressure until a maximum when the harmonic flux starts slowly decreasing. Although the exact maximum pressure depends on variables that can not be controlled, an ideal pressure is $\sim$20 mbar. Increasing the laser power also increases the harmonic flux however often a limit is reached when increasing the laser power does not increase harmonic flux. Unfortunately the laser power at which increasing the power further has no effect appears to be very variable and therefore will need to be checked whenever using the SIGC source. Varying the laser power to optimise the harmonics flux is easy and is a standard process when we use gas jet and finite gas cells.

As harmonic flux increases with decreases in the fundamental wavelength, we wished to generate HHG in the SIGC using 395 nm. Unfortunately it was not possible to produce harmonics with 395 nm from the current set-up. The next step would be to change the 75 cm focusing lens to a focusing mirror as this means the laser pulse would not be stretched as it passes through a lens. Once the SIGC is optimised for generation from 395 nm a quantitative comparison to a gas jet would be useful.

# Chapter 4

# Photoelectron spectroscopy of the A-band Dissociation of Methyl Iodide using a two-photon UV probe

This Chapter is based on work published in the paper: Photodissociation dynamics of CH3I probed via multiphoton ionisation photoelectron spectroscopy, Physical Chemistry Chemical Physics, 21, 11142 (2019), by Emily M. Warne, Briony Downes-Ward, Joanne Woodhouse, Michael A. Parkes, Darren Bellshaw, Emma Springate, Paulina Majchrzak, Yu Zhang, Gabriel Karras, Adam S. Wyatt, Richard T. Chapman, Adam Kirrander and Russell S. Minns. Both EMW and BDW are joint lead authors. RSM designed the experiment. EMW, BDW, RSM, MAP, RTC, ASW, PM, YZ and GK performed the experiment, and RTC, ASW, ES, PM, YZ and GK manage and run the Artemis laser facility and supported the experiment. EMW, BDW, RSM and JW analysed and modelled the experimental data, with EMW focusing on the data following excitation by 269 nm and BDW focusing on the data following excitation by 255 nm. AK and DB performed surface hopping trajectory calculations. All parties discussed the data and analysis. This chapter focuses primarily on the data 255 nm, however the 269 nm is present to provide a comparison and for completeness of discussion. A more comprehensive analysis of the

269 nm data can be found in EMW thesis[117].

## 4.1 Introduction

Methyl Iodide ($CH_3I$) is a well studied molecule, its a relatively small molecule and its first absorption band results in a rapid dissociation. The structure of methyl iodide along with bond lengths and angles are shown in figure 4.1. The potential energy surfaces that make up the A-band absorption spectrum are strongly dissociative and relatively simple but contain a conical intersection which affects the dissociation dynamics. The A-band is a generic term for the lowest lying electron states from the same electronic configuration. This makes it an ideal system to study the effects of conical intersection on molecular dynamics. Conical intersections, as discussed in section 1.1.4 often play important roles in more complex polyatomics providing routes for internal relaxation. Being well studied also makes it a good molecule to test new experimental and computational techniques. $CH_3I$ is also a molecule of interest in atmospheric chemistry due to its presents in the stratosphere and because after photodissociation to $CH_3$+I, the iodine fragment can act as a catalyst for ozone depletion.

Figure 4.2 shows 1-D cuts along the potential energy surfaces of the three states that are optically accessible from the ground state which are present in the A-band of $CH_3I$. The A-band of $CH_3I$ absorption spectrum spans the wavelength range from approximately

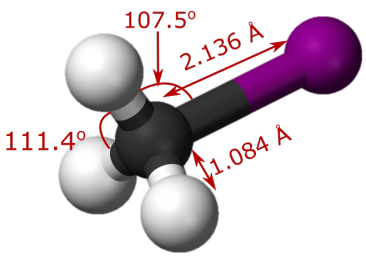


**Figure 4.1:** A diagram of methyl iodide with the iodine atom in purple, hydrogen in white and carbon is in grey. The bond angles are in degrees. Bond angles and lengths are taken from reference [126].

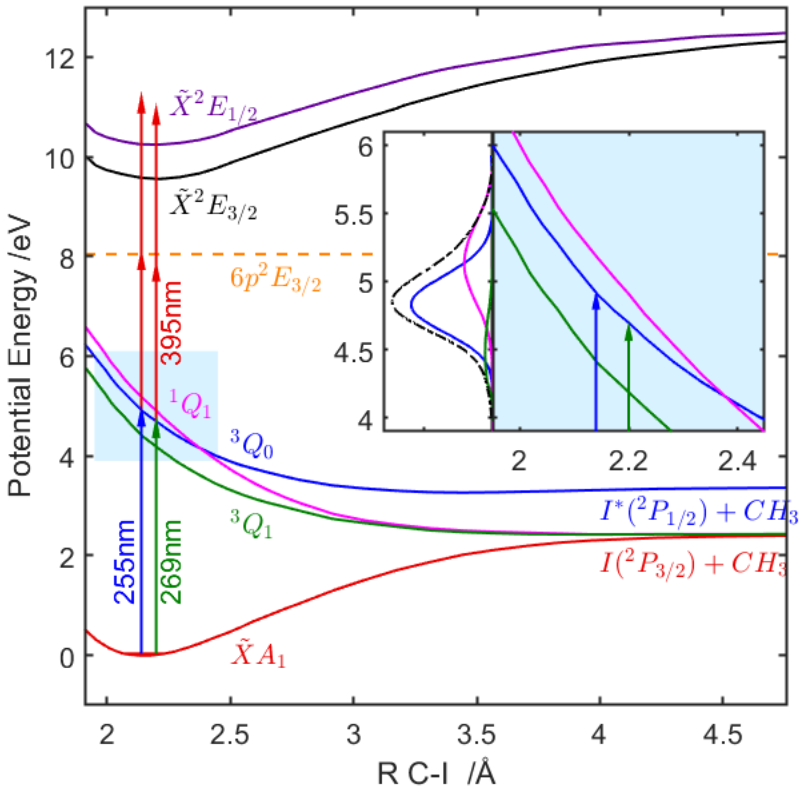


**Figure 4.2:** 1-D cuts along the C-I dissociation coordinate of the potential energy surfaces of $CH_3I$ relevant to the UV photodissociation and photo-electron detection scheme used. The potential energy surfaces shown are those in the A-band which are optical accessible from the ground state of $CH_3I$. The dashed orange line indicates the location of a resonance Rydberg state. Inset: expanded figure of the excited state potentials and a breakdown of the absorption spectrum into contributions from the three Q states associated with the A-band absorption as a function of energy. The neutral CH3I states are taken from [127], the cation states are taken from [128]. The absorption curve and decomposition are taken from [9].

220-300 nm (5.64-4.13 eV) with a maximum absorption at 258 nm as shown in the insert in figure 4.2. The A-band of $CH_3I$ is due to $\sigma^*(C-I) \leftarrow n(I)$ transition leading to the electronic configuration, $(\sigma)^2(n)^3(\sigma^\star)^1$. This electronic configuration gives rise to five states due to the presence of the atom iodine which results in strong spin-orbit coupling[129]. In Muliken[130] notation these states are labelled $^3Q_2$,$^3Q_1$,$^3Q_{0^+}$,$^3Q_{0^-}$ and $^1Q_1$. The notation is in the form $^{2S+1}Q_\Omega$, where $S$ is the total spin quantum number, $Q$ is an arbitrary label and $\Omega$ is the projection of the total electron angular momentum along the internuclear axis and the $+/-$ are the symmetry of the molecular

orbital. Only transitions into the $^3Q_1$,$^1Q_1$ and $^3Q_{0^+}$ states (the $+$ will be dropped from now on) are optically allowed transitions. The strong parallel transition to the $^3Q_0$ state dominates the absorption spectrum. Both the transitions two the $^3Q_1$ and $^1Q_1$ states are weak perpendicular transitions. The $^3Q_1$ state has a maximum to the red side of the absorption and the $^1Q_1$ has a maximum to the blue side of the absorption maximum. The relative contributions of the $^3Q_1$ and $^1Q_1$ states to the overall absorption profile are uncertain and a number of different decompositions of the A-band are present in the literature which are discussed in detail in the next section.

Figure 4.2 shows that all three potential energy curves in the A-band are strongly dissociative in character and excitation onto them will result in the breaking of the C-I bond. At a C-I bond length of 2.4 Å there is a conical intersection between the $^3Q_0$ and $^1Q_1$ states, this allows for transfer between the two states. The $^3Q_0$ state results in the products $CH_3$+I* $\left(^2p_{1/2}\right)$. While the $^1Q_1$ and $^3Q_1$ states lead to the ground state products, $CH_3$+I$\left(^2p_{3/2}\right)$.

Frequency-resolved measurements [14, 131, 132, 133, 134, 135, 136, 137] across the A-band of this system have focused on the product formation and their angular distribution. The highly parallel nature (to the polarisation of the laser) of the product recoil fragments of both spin orbit states of the measured iodine product is evidence of rapid dissociation and the majority of the population being excited by a parallel transition into the $^3Q_0$ state [14, 132, 133]. A number of studies have been carried out at 266 nm, as it is the third harmonic of a Ti:sapph laser measuring the quantum yield of the products. They have all shown consistent results with around 70% yield[14, 9, 136, 137] of spin-orbit excited iodine. At wavelengths below 225 nm the $^1Q_1$ state dominates the formation of the ground state products [133], shown by the product channel having a perpendicular angular distribution ($\beta_2$ <0). $\beta_2$ is an anisotropy parameter and can have a value of $2 > \beta_2 > -1$. A value of 2 indicates a completely parallel distribution and $-1$

is a perpendicular distribution. A more detailed explanation of beta values can be found in section 4.3.1. As excitation onto the $^3Q_0$ state is a parallel transition and excitation on the $^1Q_1$ state is a perpendicular transition, if both states contribute equally to a product channel the overall angular distribution would be isotropic ($\beta_2$=0). The same justification can be used to measure the contribution of the $^3Q_1$ state as it is also a perpendicular transition at the other side of the absorption band. While no experiments show the $^3Q_1$ state dominating the ground state product formation there is a significant contribution at wavelengths longer the 330 nm with $\beta_2$ values around 0.3 [14, 132] compared with a $\beta_2$ value of 1.7 at 266 nm [129, 138]. As the wavelength increases, moving further to the red side of the absorption band the quantum yield of I$^*$ decreases, dropping to about 30% at 300 nm and more ground state iodine is formed [14, 135]. Over the central region of the absorption band (280-240 nm), the quantum yield is roughly the same[9, 133, 132] (and references therein). At both 266 nm and 248 nm there are a number of experiments measuring the quantum yield, there is a variation of about 20% making it difficult to determine changes in quantum yield.

There are also a number of frequency domain experiments on the blue side of the absorption maximum that measure the quantum yield. A significant number of these experiments have been at 248 nm and obtain values around 0.6-0.8 for the quantum yield of I$^*$, $(\Phi_{I^*})$ [14, 139, 140, 141], an experiment by Karpov *et. al* at 254 nm obtains the value of 0.8 for $(\Phi_{I^*})$[134]. Both Eppink and Parker[14] and González *et. al*[133] have used product angular distribution measurements to determine the contribution of the $^1Q_1$ state to the overall absorption. González *et. al* showed the $^1Q_1$ state doesn't contribute significantly until 220 nm [133].

The majority of previous time-resolved studies have focused on the red side of the absorption band, around 266 nm. A number of product formation experiments at 266/268 nm experiments have been carried out, these have all shown a consistent picture, rapid dis-

sociation on the $^3Q_0$ state, with a formation time of 100 fs for excited state iodine. While the ground state iodine formed by a transition from the $^3Q_0$ state to the $^1Q_1$ state through the conical intersection had a formation time of around 80 fs from experiments with a pump-probe cross-correlation of about 200 fs [129, 142, 19, 143]. The appearance time, in this case, is defined as the time taken for the C-I bond length to reach approximately 13 Bohr. The 13 Bohr value is derived from calculations of when the experimental resonance conditions are met for the resonance enhanced multiphoton ionisation (REMPI) detection scheme [19]. This is when the ground electron state of the methyl fragment and the $3p_z$ Rydberg state is separated in energy by 2 photons of the probe wavelength. A Coulomb explosion experiment using a 272 nm pump laser was shown to be consistent with the product formation experiments [22], giving a photodissociation time of approximately 100 fs.

The only time-resolved study on the blue side of the absorption maximum we are aware of measured the fragment formation time following excitation by 243 nm similar to the previously mentioned experiments using 268/266 nm [19]. For a pump wavelength of 243 nm they observed a formation time of vibrational ground state $CH_3$ correlated with $I\left(^2P_{3/2}\right)$ and $I^*\left(^2P_{1/2}\right)$ of 53 fs and 83 fs respectively. The formation time of the products was defined the same as for the 266 nm pump wavelength. This is shorter than the times measured with the longer pump wavelength, this not surprising given the increased pump energy meaning there is more kinetic energy available upon dissociation. Interestingly they observe an increase in formation time with vibrational excitation of the methyl fragment umbrella mode ($\nu_2$) at 243 nm which is not observed in 268 nm results. As the probing step is the same for both pump wavelengths the probe step can not be the cause of the observation that the formation time increases with methyl fragment vibrational excitation at 243 nm. This observation could also not be explained by the 4D wavepacket or 9D surface-hopping trajectory calculation they also carried out which showed the vibrationally excited product being formed typically within about 10 fs of the

vibrationless products. Whereas the experiment showed the vibrational products being delayed by as much as ∼80 fs [19]. Currently there is no explanation for the delay in the observation of the vibration products with a 243 m pump.

We investigate the photodissociation dynamics of $CH_3I$ following excitation into the A-band using time-resolved photoelectron spectroscopy (TRPES). The $CH_3I$ molecule has been excited using two different pump wavelengths, 269 nm (4.61 eV) and 255 nm (4.86 eV), at the red and blue side of the absorption maximum. The early time dynamics where then observed using a two-photon ionisation 395 nm (3.14 eV) probe. The excitation and ionisation processes are shown in figure 4.2.

The rest of this chapter presents the results from the TRPES experiment mapping the dissociation of $CH_3I$. After discussing the experimental set-up and data analysis there is a brief discussion on the results from excitation by the 269 nm pump. Then the results from excitation by the 255 nm pump laser is discussed and finally discuss how these results compare to other results in the literature.

### 4.1.1 A-State Absorption Band

To understand the photodissociation dynamics of $CH_3I$ it is important to understand the contributions of the three potential energy states to the initially excited wavepacket. Unfortunately in $CH_3I$ there is still some uncertainty and disagreement around the contributions of each state to the overall absorption and how the contributions from the different states change across the absorption band. In this section we summarise some key results relating to the composition of the A-band absorption. Figure 4.3 shows four decompositions of the A-band absorption. Figure 4.3 a) and b) are experimental results obtained by magnetic circular dichroism (MCD) [144] and final product state angular distributions [14] respectively. Figure 4.3 c) and d) are computational results from Rubio-Lago *et. al*[132] and from Alekseyev *et. al* [9] respectively. In all figures the

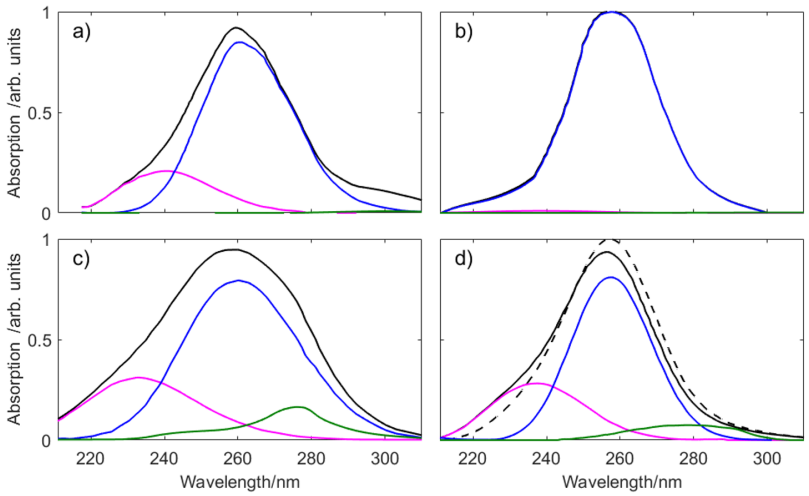


**Figure 4.3:** Four decompositions of the A-band of methyl iodide from the literature. The black line shows the overall absorption. The pink, blue and green lines show contribution to into the $^1Q_1$, $^3Q_0$ and $^3Q_1$ states. a) and b) are from experimental results. a) is from a magnetic circular dichrosim experiment taken from [144], b) from final product angular distribution taken from [14]. c) and d) are theoretical results taken from [132] and [9] respectively. The black dashed line in d) is an adjusted absorption curve which matches the experimental absorption curve better. Both the total observation and the decompositions for all figure have been taken from the respective literature.

black line is the overall absorption. The pink curve is absorption into the $^1Q_1$ state, the blue curve absorption into the $^3Q_0$ state and the green curve absorption into the $^3Q_1$ state. In figure 4.3 d) the dashed line is an adjusted absorption curve created by adjusting the centre of the different curves to more closely match the experimental absorption curve. This was justified due to the computational method usually overestimating the energy of potential energy curves, for more detail see [9]. Both experimental results use the same centres for the three absorption curves determined by the MCD experiment. Experimental measurements of the angular distribution of the products from Eppink and Parker [14] show highly parallel products, suggesting a contribution of less than 1% of the absorption maximum from the $^1Q_1$ state and the $^3Q_0$ state. Whilst MCD [144] results suggest the contribution from $^1Q_1$ is about 20% of the absorption maximum. Eppink and Parker suggest the difference in the contribution of the $^1Q_1$ may be due to dimers formed in the MCD experiments. Eppink and Parker also make a few assumptions

that would result in a low estimate absorption in the $^1Q_1$ state. They assumed there is only transfer through the conical intersection from the $^3Q_0$ state to the $^1Q_1$ state and not the other way. They also assume that product contributions from the $^1Q_1$ would be purely perpendicular.

Computational predictions[132, 9] also show a similar contribution from the $^1Q_1$ state and also predicate a contribution of about 10% for the $^3Q_1$ state, this is a much higher value than either experimental results. However as previously state computational models tend to over predict the energy of excitation, also the dipole moment for transition into the $^1Q_1$ state from *ab initio* data overestimates the absorption[19, 143]. Both computational studies used the same potential energy surfaces from [9]. A summary of the differences between the relative percentage excitation fraction of each state for the two central wavelengths studied is shown in table 4.1. The percentage excitation fraction is the percentage of molecules that are excited into the different states.

| | 255 nm | | | 269 nm | | |
|---|---|---|---|---|---|---|
| | $^3Q_0$ | $^1Q_1$ | $^3Q_1$ | $^3Q_0$ | $^1Q_1$ | $^3Q_1$ |
| magnetic circular dichroism[144] | 86.0% | 14.0% | 0% | 96.7% | 3.3% | 0% |
| product state angular distributions[14] | 99.5% | 0.5% | 0% | 100% | 0% | 0% |
| wave packet calculations[132] | 80.5% | 14.2% | 5.3% | 81.7% | 5.1% | 13.3% |
| multireference configuration interaction[9] | 75.3% | 23.9% | 1.8% | 81.6% | 8.0% | 10.3% |

**Table 4.1:** Percentage excitation fraction at the two wavelengths studied based on published experimental and theory results.

## 4.2 Experimental

The experiment was performed at the Artemis laser facility. The general experimental beamline and chambers for TRPES experiments were described in more detail in chapter 2, here we describe the specifics of this experiment.

The pump pulses were generated using 8 W from compressor 1 to pump the HE-TOPAS OPA to generate either 269 or 255 nm as described in chapter 2 . This gave a pulse energy 6 and 1 $\mu$J for 269 and 255 nm respectively. The pump beam was then focused outside the vacuum chamber with 1 m focusing mirror and reflected into the interaction chamber with a D-Shape mirror.

The probe was generated using the output from the compressor 2 and a BBO to produce the second harmonic of 790 nm at 395 nm. The pulse power of the probe was 10 $\mu$J. The second harmonic was separated from the fundamental using a pair of dichroic mirrors. The probe was focused into the interaction chamber by the toroidal mirror. The angle between the two beams was about $3^o$.

The relative delay between the two beams can be changed by moving the translation stage in the pump beam path. To find the rough point when both pulses arrive at the same time (time zero), an oscilloscope and photodiode are used to overlap the pulses in time. To increase the precision we then looked for the increased intensity in the VMI image. Before time-zero there will not be any signal, when there begins to be photoelectron signal we must be close to time-zero this method provides a precise enough time-zero to perform the experiment. An even more precise time-zero is determined from the data using the fits discussed in section 4.3.3. For our experiments, we then scan through a range of -300 to 500 fs for 269 nm and -500 to 300 fs for 255 nm in 25 fs steps (Total stage movement of $\sim$120 $\mu$m).

The $CH_3I$ is introduced into the chamber by expanding the room temperature vapour of $CH_3I$ from a liquid sample holder through a 1 KHz pulsed nozzle. This produces a molecular beam which is skimmed before crossing the laser beams.

The photoelectrons were collected using the VMI detector as described in section 2.3.3.2.

The VMI repeller was set to 250 V and the extractor set to 183 and 184 V for 269 nm and 255 nm respectively. The MCP image was recorded with the sCMOS camera with 10 s exposure, two images were recorded before moving to the next delay. We cycled through each time step 26 times for 269 nm and 4 times for 255 nm. There was a camera error during the acquisition for 255 nm resulting in the camera not recording images after the 4th cycle. After 26 cycles for the 269 nm the sample ran out stoping the data acquisition. The total collection time per each delay was 520 s for 269 nm and 80 s for 255 nm.

## 4.3 Data Analysis

### 4.3.1 Polar Onion Peeling

As explained in section 2.3.3.2 the measured VMI image is a 2-D representation of a 3-D newton sphere. This 3-D sphere consist of concentric spherical shells, each shell originates from electrons with a particular kinetic energy and with an angular distribution defined by,

$$I(\theta) \propto \sum_{even\ n \geq 0}^{2^{*}photons} \beta_m(r) P_n(cos\theta) \tag{4.1}$$

where $\theta$ is the angle between the laboratory frame z-axis and the electrons direction of ejection. $\beta_m$ is the anisotropy parameter and $P_n$ is the n$^{th}$ order Legendre polynomial. As

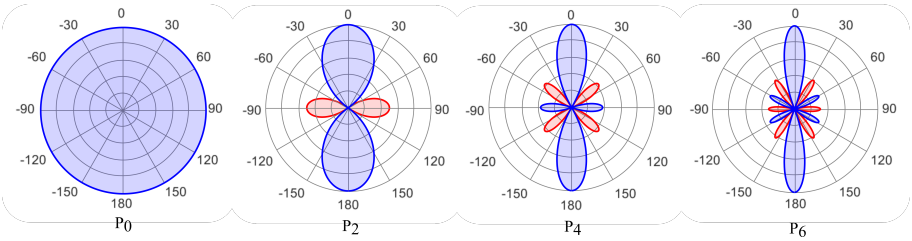


**Figure 4.4:** The Legendre polynomial distribution for $P_0$, $P_2$, $P_4$ and $P_6$. The blue angles show area of enhanced electron emission compared to an isotropic distribution and the red angle are the region with decreased electron emission.

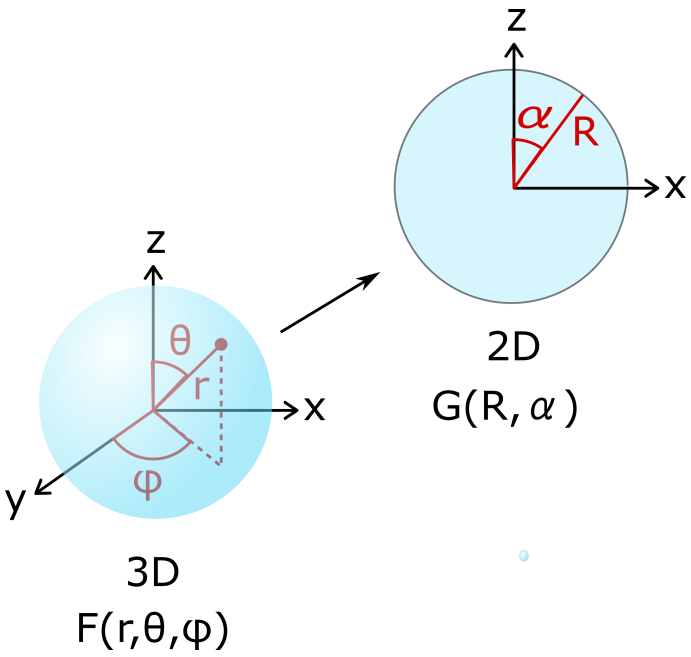


**Figure 4.5:** The VMI process of collapsing a 2D Newton sphere of electrons described by $F(r, \theta, \varphi)$ into a 2D projection described by $G(R, \alpha)$. The laser is polarised along the $z$ axis and the detector is in the $x - z$ plane. Figure adapted from [117] with permission.

the $CH_3I$ is ionized by three photons $\beta_2$, $\beta_4$ and $\beta_6$ are included in the fit. The first term is isotropic as $P_0(cos\theta) = 1$, the angular distribution for $P_2$, $P_4$, $P_6$ are shown in figure 4.4.

Figure 4.5 shows a Newton sphere which is described by $F(r, \theta, \varphi)$, being projected along the y-axis onto a detector in the x-z plane, and the laser polarisation is along the z-axis. This 2-D projection is described by $G(R, \alpha)$. The coordinate system used to describe the 3-D and 2-D functions are defined in figure 4.5. $r$ always refers to the radius of the 3-D function while $R$ is used for the radius of the 2-D function. This transform is known as an Abel transform.

This projection means that at radius, $R$, of the 2-D image there are contributions from both electrons with $r = R$ in the 3-D Newton sphere but also from electrons with $r > R$ and $\varphi \neq 90^o$ or $270^o$ so they weren't perpendicular to the detector. Because the 3-D sphere has cylindrical symmetry around the laser polarisation axis which is parallel to the

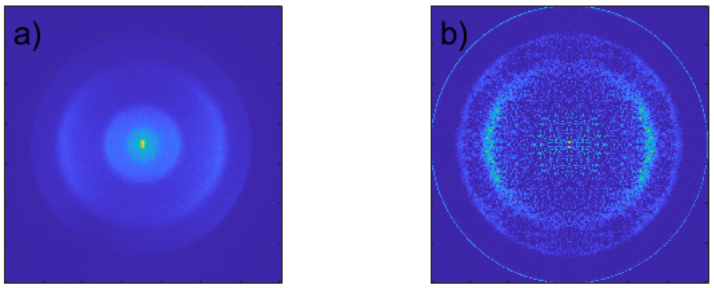


**Figure 4.6:** a) The original recorded VMI image at time zero after excitation with a 255 nm pump and ionisation by two 395 nm photon. b) the reconstructed image from a) from the POP MatLab code from Natan[145].

detector it is possible to retrieve the Newton sphere from the 2D image. An example of the 2D projection which is recorded is shown in figure 4.6 a).

To retrieve the 3D distribution the most common methods are pBASEX (polar basis set expansion) or POP (polar onion peeling). In pBASEX the image is fitted using a basis set of functions with know inverse Abel transforms which correspond to a particular radius and angular distribution. The coefficient for each basis set is calculated using the singular value decomposition method. We used the POP method which has been shown to produce similar results to pBASEX but is faster and less computationally expensive [146]. The code we used is based on the methodology developed by Roberts *et al.* [146] and implemented in MATLAB by Natan. [145]. The reconstructed image from the POP Matlab code for figure 4.6 a) is shown in b)

The centre of the image is found by taking a slice of the image which is summed over and plotted against radius. If the center is correct the position of the peaks will line up. This is shown in figure 4.7, a) shows the data which hasn't been centred correctly while b) shows the same data but with the correct centre. This process is done in both x and y directions to find the image centre.

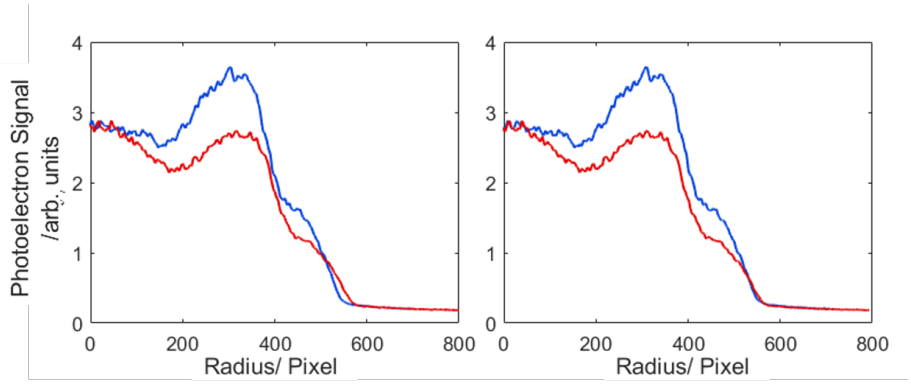


**Figure 4.7:** A sum across the bottom half of the VMI images shown in figure 4.6. The blue line is the right hand side of the image and the red line is the left hand side. a) the centre of the image is incorrect and b) the centre has been moved by 6 pixels so the peaks line up showing the centre has been found.

After finding the centre of the image the first step is to collapse the image down to a single quadrant where each pixel is the mean value of the equivalent pixels in the four quadrants of the original image. Next the Cartesian coordinates of the image are changed into polar coordinates to reduce error. In Cartesian coordinates there is significant error accumulation as the process has to start with the outermost point on the detector where the signal is smallest due to the Jacobian from going from 3D spherical coordinates to 2D Cartesian. In polar coordinates the error at large radii is reduced and error accumulation is not a concern. This transform is depicted in figure 4.8. The length of the $90^o$ arc at radius $R$ is $2\pi R/4$ and at $R = 0$ we have one pixel therefore the number of polar pixels at $R$ is $\pi(R + 1)/2$. The intensity value for each polar pixel is calculated from the average value of the Cartesian pixels it overlaps and weighted by the degree of overlap.

Once this is completed the onion peeling can start. The 2D image can be expressed at the sum of individual 2D projection $g(r; R, \alpha)$ for all $r$ components of the full 3D distribution $F(r, \theta, \varphi)$

$$G(R, \alpha) = \int_0^{r_{max}} g(r; R, \alpha) dr, \tag{4.2}$$

where $R \leq r$. At $R_{max}$ there are no more, higher energy electrons, therefore the only

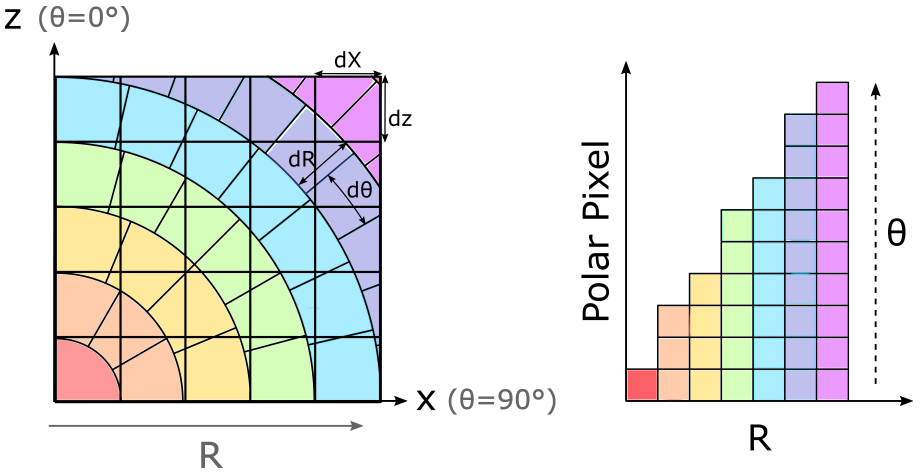


**Figure 4.8:** a) shows the original Cartesian grid in black and the new polar grid is shown in gray. Each radius is shown in different colours. b) shows the increase in number of pixels with increasing radius.

contribution is from most energetic electron with $\varphi = 0$. This means the $\alpha$ dependence, $I(\alpha)$ in the 2D image is equivalent to the $\theta$ dependence in the Newton sphere, $I(\theta)$, which is described by equation 4.1. Therefore the $\beta$ values can be determined for $r_{max}$. This allows the 2D projection to be calculated. The POP code used pre-computed basis set of 2D projections of radial $\delta$-function to speed up the computational time. The basis is found using a numerical simulation method rather than an analytical calculation, $10^8$ random values of $\theta$ and $\varphi$ are generated to create a Newton sphere with radius $r$. These are then projected into 2D as $x = rsin(\theta)sin(\varphi)$ and $z = rcos(\theta)$. A factor of $sin(\theta)$ is included to account for size of each surface interval, $r^2 sin(\theta)d\theta d\varphi$ has a $sin(\theta)$ dependence. The 2D distribution is normalised and then converted to polar coordinates the same way as the data was.

With $g(r_{max}; R, \alpha)$ now known it can be subtracted away from the experimental image, "peeling away" the outermost shell of the Newton sphere. This process is then repeated for $(r_{max} - dr)$, this continues until the entire image is inverted.

Figure 4.9 shows how POP work for a simple example with two different electron kinetic energies. The total 2D projection is shown by the yellow line made up of two contributions

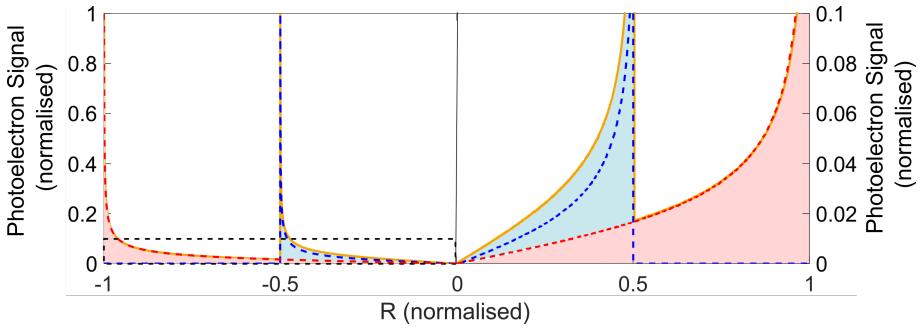


**Figure 4.9:** An example of a 2D projection (yellow line) of a Newton sphere made of two shell electrons. The contribution to the total image from the higher energy, outer electron shell is shown by the red dashed line. The contribution to the total image from the lower energy, inner electron shell is shown by the blue dashed line. The figure shows the full diameter of the image, with the left hand side showing the full intensity range and the right hand side shows a more zoomed in version. Figure adapted from [117] with permission.

shown by the red and yellow fill. The right hand side is a zoomed in version of the left hand side and shows the area indicated by the black dashed box on the left hand side. As previously stated the contribution from higher energy electron can be determined from the signal at $|R|$=1 This signal shown by the dashed red line is subtracted to leave the blue dashed line. The contribution from the lower energy electron can now be determined from the signal at $|R|$=0.5, allowing the spectrum to be reproduced.

### 4.3.2 Calibration

The photoelectron spectrum derived from the image in figure 4.6 is shown in figure 4.10 a). A background is taken as an average of the first three earliest time spectra, from the inverted images, where no pump-probe signal is observed and is subtracted across all time delays. This removes the pump only and probe only signal. Two photons of 255 nm have a total energy of 9.74 eV, which is greater than the IP of $CH_3I$ which is 9.53 eV. In figure 4.10 we observed two peaks at small radii (low energy) which are the result of two photon absorption of the probe. As these peaks have no probe dependence they are removed by the background subtraction. These peaks are not observed in the 269 nm data as there is not enough energy from two 269 nm photons (9.22 eV total

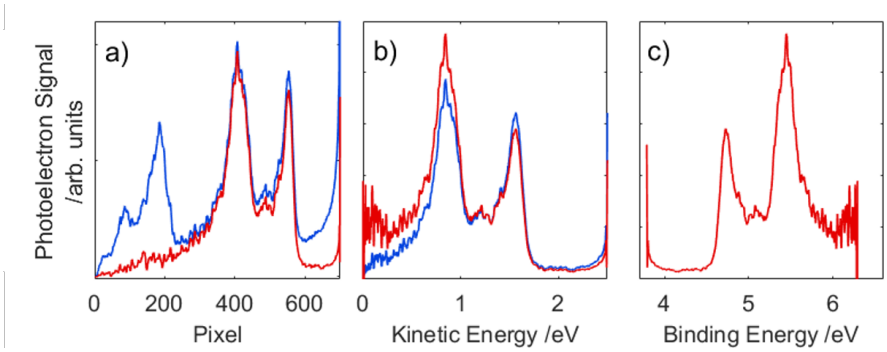


**Figure 4.10:** a) shows the spectrum from the image in figure 4.6 which corresponds to excitation by 255 nm and ionisation at 395 nm at time zero in blue and the same spectrum with the background subtracted in red. b) shows the spectra on the kinetic energy scale without the Jacobian scaling (blue) and with the Jacobian scaling (red). c) shows the spectrum including the Jacobian on the binding energy scale.

energy) for ionisation.

To convert the x-axis of the photoelectron spectrum from radius to binding energy we use conservation of energy to give,

$$BE = h\nu_{probe} - E_{KE} \tag{4.3}$$

$$= h\nu_{probe} - mR^2 \tag{4.4}$$

where $\nu_{probe}$ is the frequency of the probe laser and $m$ is a constant. $BE$ is the binding energy of the molecule, $E_{KE}$ is the kinetic energy of the photoelectron which is proportional to the radius on the image squared ($R^2$). Hence if a peak is known to appear at a certain binding energy the value of $m$ can be calculated. Figure 4.11 shows the calibration curve to convert from pixel radius to electron kinetic energy. Due to peaks shifting to lower binding energy at later times we calibrated the spectra using a spectrum at 100 fs when the peaks have shifted to the lower binding energy. We could assign three peaks as shown by the cross in the figure. The blue cross is from two photon absorption of the pump while the other two peaks where pump-probe features, shown in red. Methyl iodide has two sharp peaks at 9.53 eV and 10.12 eV which were used [147]. The peaks

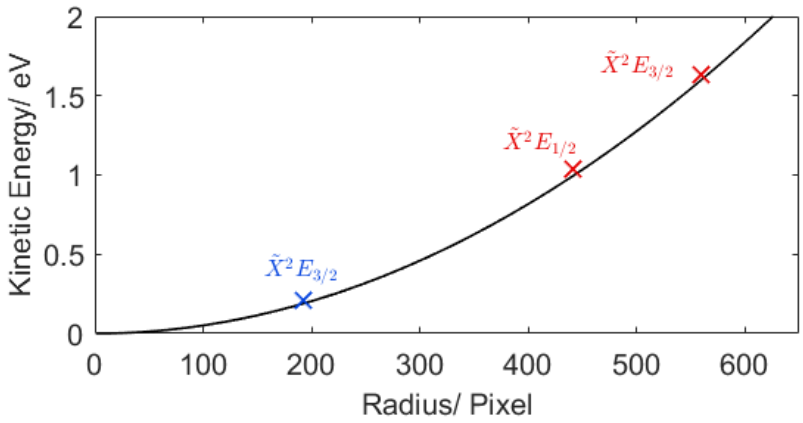


**Figure 4.11:** The calibration curve to convert from pixel radius to electron kinetic energy. The blue cross represents a peak from two photon absorption of the 255 nm pump, while the red crosses are the known peak from a 255 nm photon and two 395 nm photons.

assignments are also labeled in the figure. As the VMI conditions are almost identical for both pump wavelengths we checked the $m$ values were very similar for consistency. When converting the axis from pixel to energy the spectra are divided by the Jacobian, which is the radius $R$, to keep a constant area under the spectra, the effect of including this factor is shown in figure 4.10 b). Binding energy has been defined with respect to the excited state to allow a more direct comparison to the XUV TRPES results. All data shown has the Jacobian included

### 4.3.3 Kinetic Equations

To obtain a more quantitative analysis of the states dynamics we used a simple kinetic model. If we consider the simple picture shown in figure 4.12 with defined energy levels. The $S_1$ state is populated by a laser pulse (pump), this state can then decay to $S_2$, the rate of this decay is defined by decay rate $\lambda_1$ (not to be confused with $\lambda$ used for frequency. $S_2$ can then decay to $S_3$ with a decay rate $\lambda_2$. The rate equations for the population of states $S_1$ and $S_2$ are given by,

$$\frac{d\rho_1(t)}{dt} = \sigma_{01} f_{pump}(t) - \lambda_1 \rho_1(t) \tag{4.5}$$

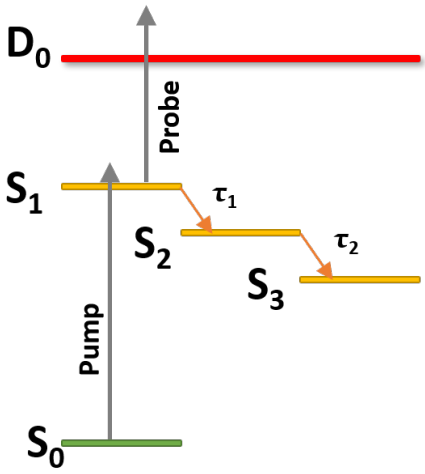


**Figure 4.12:** A simplified pump-probe diagram with three distinct excited states. $S_0$ is the intial populated ground state. $S_1$ is the excited state which decays to $S_2$ which subsequently decays to $S_3$. The probe ionises to the $D_0$ state.

$$\frac{d\rho_2(t)}{dt} = \lambda_1\rho_1(t) - \lambda_2\rho_2(t) \tag{4.6}$$

where $\rho_1$ and $\rho_2$ are the population of states $S_1$ and $S_2$ respectively and $\sigma_{01}$ is the cross-section for excitation from the ground state $S_0$ to the excited state $S_1$. $f_{pump}$ is the is time profile of the pump laser pulse. This is usually assumed to be a Gaussian:

$$f_i(t) = \frac{I_i}{\sqrt{2\pi}\sigma_i} e^{\left(-\frac{1}{2}\left(\frac{t}{\sigma_i}\right)^2\right)}; (i = pump, probe) \tag{4.7}$$

where $I_i$ is the total pulse intensity, and $\sigma_i$ is the standard deviation of the Gaussian laser pulse. Be careful not to confuse $\sigma$ used for standard deviation with $\sigma$ for cross-section. The first order solution of equation 4.5 has a known solution which leads to the expression for $\rho_1$

$$\begin{aligned}\rho_1(t) &= e^{-\lambda_1 t}\left(\int_{-\infty}^{t} e^{\lambda_1 x}\sigma_{01} f_1(x)dx + C\right) \\ &= e^{-\lambda_1 t}\frac{I_{pump}}{\sqrt{2\pi}\sigma_{pump}}\sigma_{01}\int_{-\infty}^{t} e^{\lambda_1 x} e^{-\frac{1}{2}\left(\frac{t}{\sigma_{pump}}\right)^2} dx\end{aligned} \tag{4.8}$$

The constant $C$ is the initial population of the $S_1$ state. As there is no other excitation pathways $C = 0$. The expression of the excited state population is then convolved with the probe laser pulse to obtain an expression for the photoelectron signal. This can be shown to equal,

$$\begin{aligned} S_1 &= \int_{-\infty}^{\infty} \sigma_{ion1} f_2(t) \rho_1(t) dt \\ &= e^{-\lambda_1 \Delta t} \sigma_{01} \sigma_{ion1} \frac{I_{pump} I_{probe}}{2} e^{\frac{(\sigma\lambda_1)^2}{2}} \left(1 + \mathrm{erf}\left(\frac{\Delta t - \sigma^2 \lambda_1}{\sqrt{2}\sigma}\right)\right) \end{aligned} \tag{4.9}$$

where $\sigma_{ion1}$ is the cross-section for ionisation from the $E_1$ state to the ion state and $\sigma = \sqrt{\sigma_{pump}^2 + \sigma_{probe}^2}$ which is the cross correlation of the pump and probe laser pulses. The $\mathrm{erf}$ function is known as the error function and is given by the equation,

$$\mathrm{erf}(z) = \frac{2}{\sqrt{\pi}} \int_0^z e^{-t^2} dt \tag{4.10}$$

If you we follow the same process with eqn 4.6, you obtain this expression for the photoelectron intensity,

$$\begin{aligned} S_2 =& \sigma_{01} \sigma_{ion2} \frac{I_{pump} I_{probe}}{2} \frac{\lambda_{12}}{\lambda_1 - \lambda_2} \times \\ & \left[ e^{-\lambda_2 \Delta t} e^{\frac{(\sigma\lambda_2)^2}{2}} \left(1 + \mathrm{erf}\left(\frac{\Delta t - \sigma^2 \lambda_2}{\sqrt{2}\sigma}\right)\right) - \right. \\ & \left. e^{-\lambda_1 \Delta t} e^{\frac{(\sigma\lambda_1)^2}{2}} \left(1 + \mathrm{erf}\left(\frac{\Delta t - \sigma^2 \lambda_1}{\sqrt{2}\sigma}\right)\right) \right] \end{aligned} \tag{4.11}$$

The second part of eqn.4.11 is the identical form to eqn.4.9. Hence it is possible to describe the population evolution at a given energy with,

$$S = \sum_i A_i e^{-\lambda_i \Delta t} e^{\frac{(\sigma\lambda_1)^2}{2}} \left(1 + \mathrm{erf}\left(\frac{\Delta t - \sigma^2 \lambda_1}{\sqrt{2}\sigma}\right)\right) \tag{4.12}$$

where $A_i$ contains all the constants from the previous equations. A positive $A_i$ indicates

a decay and a negative value indicates a population rise. A Gaussian component may need to be included for the non-resonance processes which occur only during pump-probe overlap to give,

$$S = A_G e^{-\frac{1}{2}\left(\frac{\Delta t}{\sigma}\right)^2} + \sum_i A_i e^{-\lambda_i \Delta t} e^{\frac{(\sigma\lambda_1)^2}{2}} \left(1 + \mathrm{erf}\left(\frac{\Delta t - \sigma^2\lambda_1}{\sqrt{2}\sigma}\right)\right) \tag{4.13}$$

Due to overlapping features in the VMI results, it's not possible to exact different features and their associated lifetimes, therefore, we performed a global fit across the whole energy range to produce a decay associated spectrum (DAS).

## 4.4 Dynamics of Methyl Iodide pumped at 269 nm

The results from excitation with a 269 nm pump have been discussed in much more detail in Emily Warne's thesis [117] as she lead the analysis however a brief overview of the key results of the analysis is presented here to allow comparison with the 255 nm results.

Figure 4.13 shows the photoelectron spectrum at time zero where there is maximum overlap between the 269 nm pump and 395 nm probe. The spectrum peaks are labelled with their assignment. We observe ionisation into both spin orbit ion states, $E_{3/2}$ and $E_{1/2}$, although there is a significantly higher intensity of electrons resulting from ionisation into the $E_{1/2}$ ion state than the $E_{3/2}$ ion state. This is not observed in any of the other results we obtained and therefore we suspect the high intensity of the $E_{1/2}$ peak is due to accidental resonance with an intermediate state in the ionisation process, however the identity of this state has not been determined. For both ion states we also observe the vibrational excitation of the $\nu_2$ $CH_3$ symmetric deformation (0.155 eV). For $E_{3/2}$ we also observe another peak which has been labelled $\nu_4$, $CH_3$ non-symmetric stretch vibration (0.379 eV) however it could also be $\nu_1$, symmetric stretch vibration (0.364 eV)

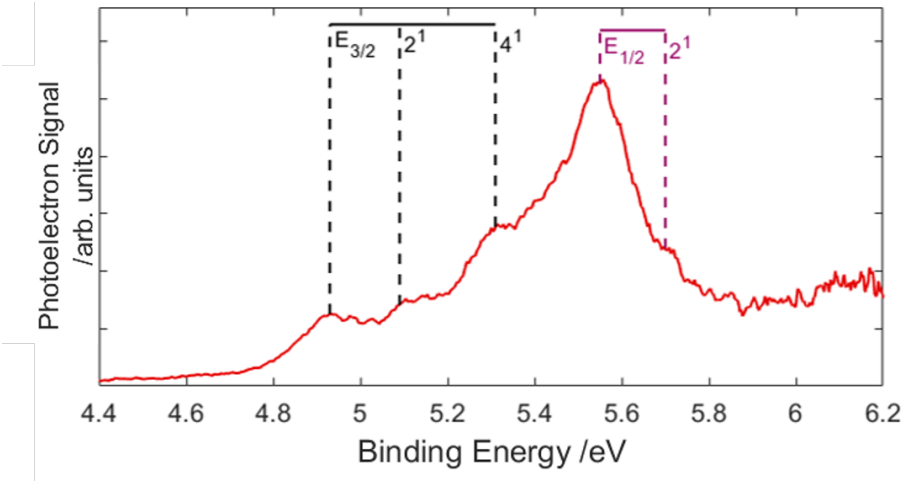


**Figure 4.13:** Photoelectron spectrum obtained at time zero with a pump of 269 nm and a two photon 395 nm probe. The combs above the spectrum indicate the expected location of the vibrational state in the lower (black) and the higher (purple) spin orbit electronic state of the ion for which peaks where observed in the photoelectron spectrum. The vibrational energies of the cation where taken from [148].

as the experiment does not have the energy resolution to separate these two vibrations. Figure 4.14 shows the time dependent photoelectron spectrum following excitation of $CH_3I$ with a 269 nm probe. The time dependent spectrum shows a short lifetime as expected from previous results around 269 nm [142, 149]. As the photoelectron spectrum was collected with a VMI the beta values could be extracted from the images using the POP code. The beta values showed no time dependence and hence only the beta values recorded at time zero have been presented in figure 4.15. As the ionisation was a three-photon process with both laser pulses being linearly polarised light, $\beta_2$, $\beta_4$ and $\beta_6$ were included in the fit. $\beta_6$ was around zero for all energies so hasn't been presented here. $\beta_2$ is close to one across the peaks showing peaks are dominated by electrons parallel to the laser polarisation. $\beta_4$ is around 0.2-0.3 suggesting that the excited state is not isotropic and is aligned with respect to the polarising light.

To obtain a quantitative measure of the lifetime the time dependent spectra were fitted using equation 4.13. The fits were performed using the Levenberg-Marquardt algorithm from MATLAB's *lsqnonlin* function. The Levenberg-Marquart algorithm is used to solve

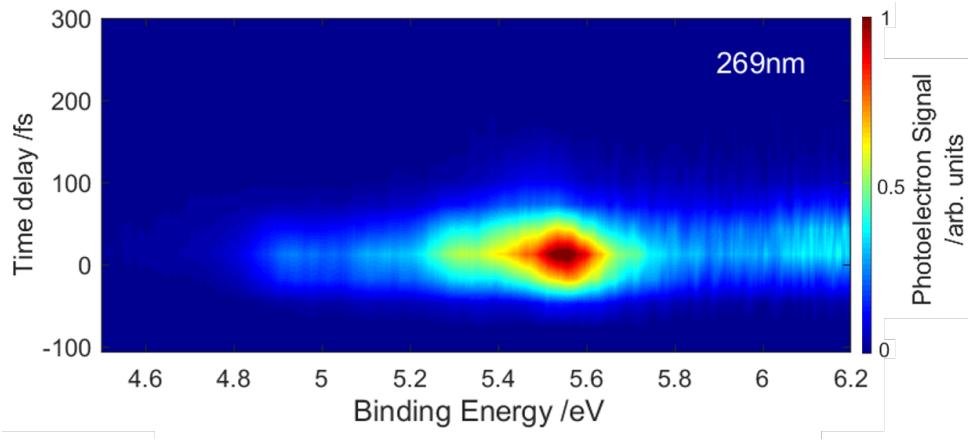


**Figure 4.14:** Time dependent photoelectron spectrum of $CH_3I$ collected via VMI following excitation by 269 nm and ionization with the 395 nm probe.

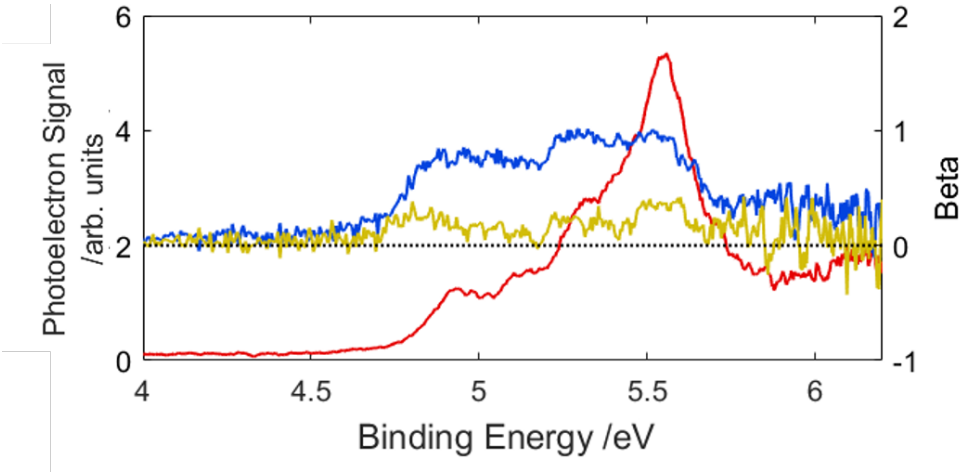


**Figure 4.15:** Photoelectron spectrum obtained at time zero with a pump of 269 nm and a two photon 395 nm probe (yellow). $\beta_2$ (blue) and $\beta_4$ (red) are plotted with the scale on the right

nonlinear least squares problems. It was determined that the best fit to the entire spectrum was achieved with a Gaussian and one exponential decay of lifetime 30 fs. The amplitude of the Gaussian $A_g$ across the spectrum is shown as the blue line in figure 4.16 b) and the amplitude of the exponential $A_1$ in the red line. An example fit is shown in figure 4.16 a) at the energy indicated by the black dashed line in b). The Gaussian had a full width half maximum (FWHM) ~65 fs. This short lifetime of the initial excited state indicates rapid movement of the wavepacket out of the observation window which is consistent with rapid dissociation of the C-I bond. This is the dynamics which is expected from the 1-D potential energy of the A-band. It also consistent with

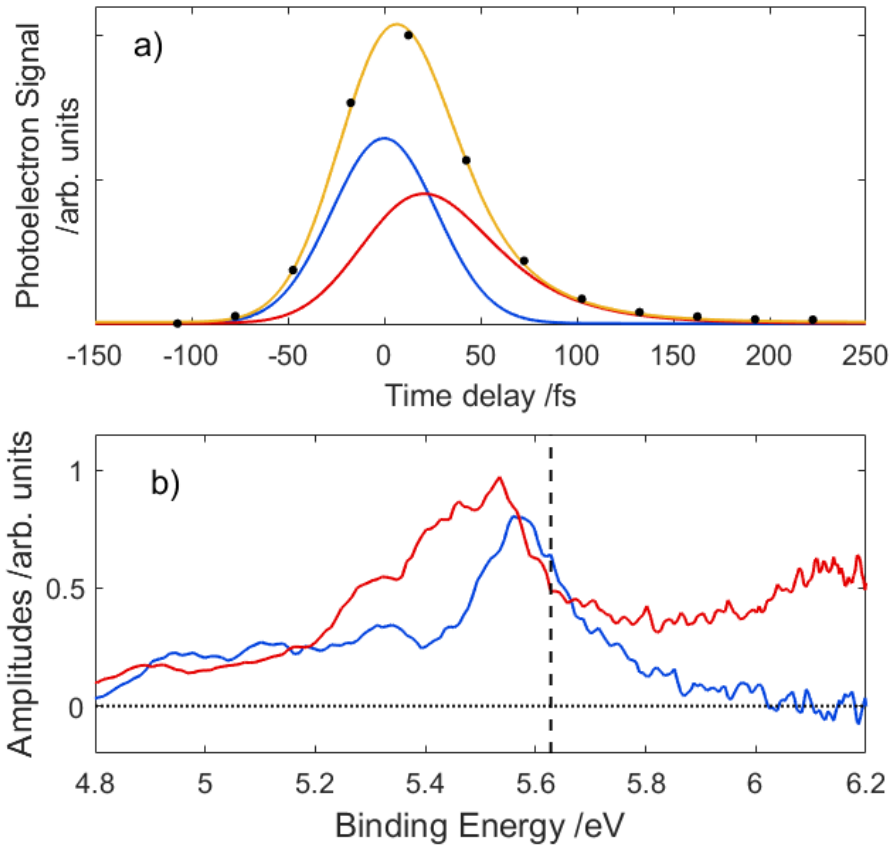


**Figure 4.16:** a) the results of the global fit (yellow) to the experimental data (black data points) at the energy indicated by the black dashed line on b). The contribution of the Gaussian (blue) and the exponential decay (red) across the entire spectrum is shown in b)

previous Coulomb explosion results at 272 nm [22] and product formation measurements at 266/268 nm [129, 142, 19].

## 4.5 Dynamics of Methyl Iodide pumped at 255 nm

The red line shown in figure 4.17 is the photoelectron spectrum at time zero. The combs above the spectra show the assignment of the peaks. Once the spectrum has been calibrated to binding energy using the known peaks as described above it is possible to make assignments of the other peaks. The binding energy of the lowest two states of the cation is taken from reference [147] while the vibrational energy of that cation is

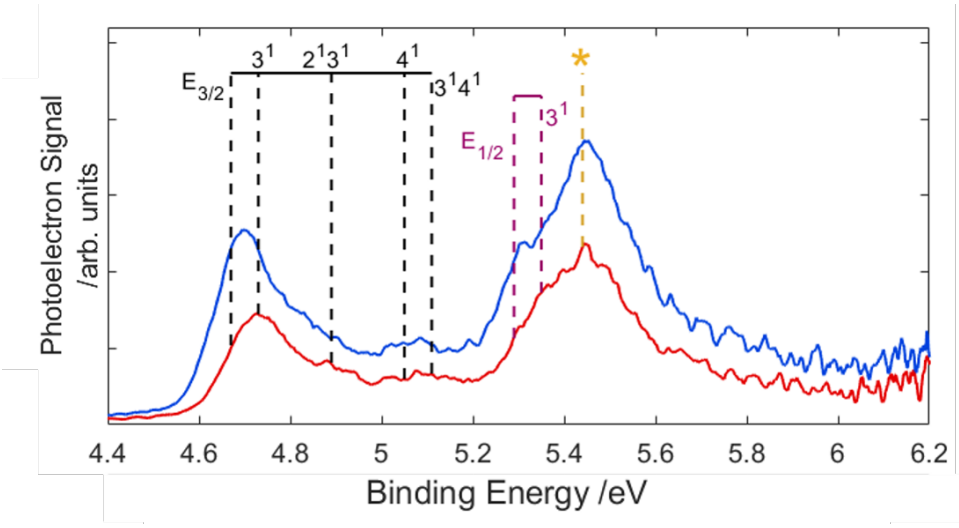


**Figure 4.17:** Photoelectron spectrum obtained at time zero (red) and 100 fs later (blue) with a pump of 255 nm and a two photon 395 nm probe. The combs above the spectrum indicate the expected location of the vibrational states in the lower (black) and the higher (purple) spin-orbit electronic states of the ion which have peaks observed in the photoelectron spectrum. Vibrational energies where taken from [148]

taken from [148]. Initially we observe $\nu_3$ C-I stretchering mode (0.067 eV) combination bands $\nu_3$ for the lower spin orbit state $^2E_{3/2}$. Similarly to the 269 nm data the $\nu_3\nu_4$ peak is to broad to distinguish between $\nu_4$ and $\nu_1$. We only observe the $\nu_3$ vibration in the high spin orbit state, $^2E_{1/2}$. The intense peak marked with $*$ has the corrected energy of the $\nu_2$ vibration of the $^2E_{1/2}$ ion state. However, we have no explanation for its high intensity, therefore, we suspected the increased intensity was due to an accidental resonance with a Rydberg state at the $1 + 1'$ level. This requires a Rydberg state with energy equivalent to one pump photon (4.87 eV) and one probe photon (3.15 eV), so a total energy of 8.03 eV. The 6p$\left(^2E_{3/2}\right)$ $\nu_1^2$ Rydberg state has energy of 7.98 eV close to the required energy [150]. Ionisation from this state would have significant overlap with the $^2E_{3/2}$ $\nu_1^2$ cation state resulting in a peak at a binding energy of 5.38 eV. The peak we observe is at 5.41 eV hence in a good agreement. Within our experiment we do not have the energy resolution to distinguish between the $\nu_1$ and $\nu_4$ vibrations, therefore we assign the peak marked with $*$ to $\nu_1^2$ or $\nu_4^2$ of the $^2E_{3/2}$ cation state due the accidental resonance with equivalent vibrations in the 6p Rydberg state at the $1 + 1'$ level.

Figure 4.18 shows the time dependent photoelectron spectrum following excitation of $CH_3I$ by 255 nm and ionisation by two 395 nm photons. There is a significant increase in the lifetime compared with figure 4.14 and significant signal is still present after 150 fs. Along with the extended lifetime there is a shift of 0.04 eV towards lower binding energies, indicated with black arrows. This results in unexpected given the previously measured lifetimes at around 266 nm, the results using a 269 nm pump and the 1D potential energy curves in figure 4.2 that indicated rapid dissociation. Analysis of these dynamics is discussed in section 4.5.1.

Figure 4.17 also shows the spectrum at ~100 fs in blue. There is an increase in the intensity of the peaks and we also see the peaks shift to energies that more closely match the ground state and vibrational energies without a $\nu_3$ excitation too. This shift is due to the increasing population in the vibrational ground state of the ion suggesting a change in the vibrational overlap between the ion state and the excited state wavepacket. The only peak that does not shift to lower binding energy is the one labeled with the orange star, this, therefore, supports the Rydberg resonance theory. As the final ionisation step involves a Rydberg state the electron emitted will always be at the same energy, in this

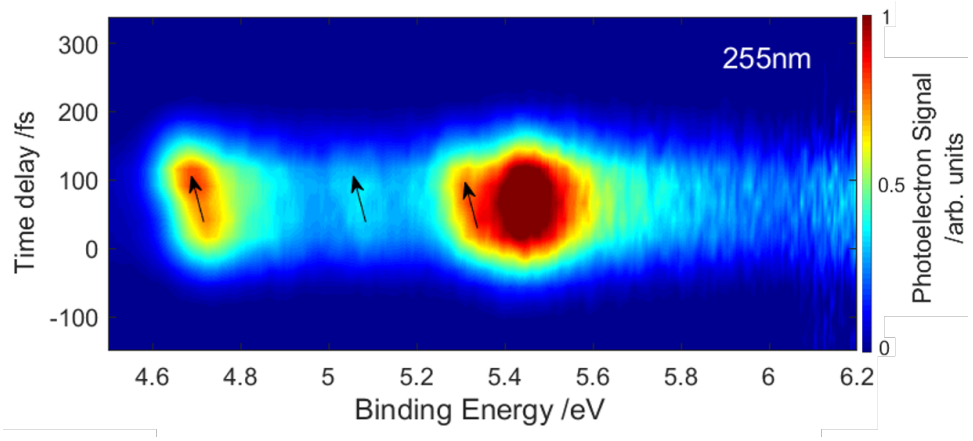


**Figure 4.18:** Time dependent photoelectron spectrum of $CH_3I$ collected via VMI following excitation by 255 nm and ionisation with the 395 nm probe. The arrows indicate the shift of peaks to lower binding energies at later delay times.

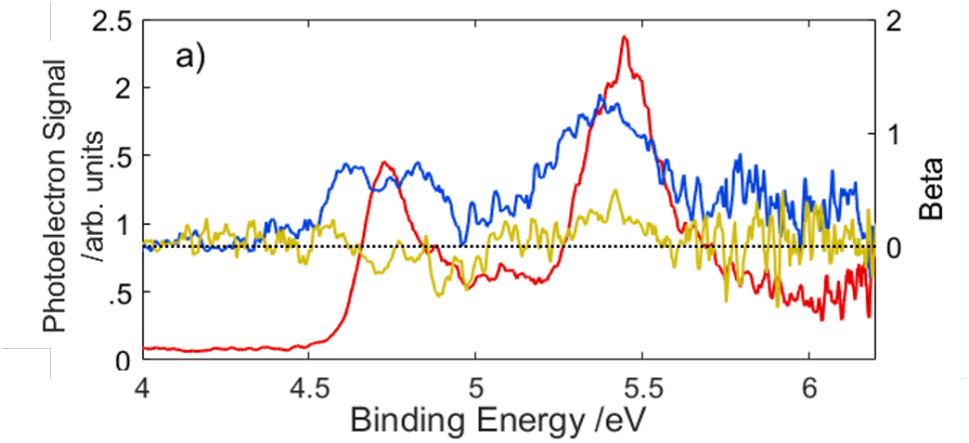


**Figure 4.19:** Photoelectron spectrum obtained at time zero with a pump of 255 nm and a two photon 395 nm probe (yellow). $\beta_2$ (blue) and $\beta_4$ (red) are plotted with the scale on the right

case as the molecule rearranges the molecule will move out of resonance with the Rydberg state. This means the probability of ionisation reduces significantly and the signal will decay instead of shifting to lower binding energy as seen with the other peak.

From the VMI images $\beta_2$, $\beta_4$ and $\beta_6$ values where obtained. The beta values show no time dependence and $\beta_6$ was around zero for all energy values. Figure 4.19 shows $\beta_2$ (red) and $\beta_4$ (yellow) values at time zero along with the time zero spectrum. $\beta_2$ across the peaks is around 1, showing the major contribution to the signal is from electrons emitted parallel to the polarisation of the laser. This is also consistent with the expected $\beta$ value from the 6p Rydberg orbital. The $\beta_4$ value shows some variation across the peaks although as the values are small across all the peaks we have placed little significance on this. As there is no time dependence of the $\beta$ value they provide limited information of the dynamics of the dissociation. The time dependence of $\beta_2$ is shown in figure 4.20. The $\beta_2$ values do not change with time while there is still significant photoelectron signal.

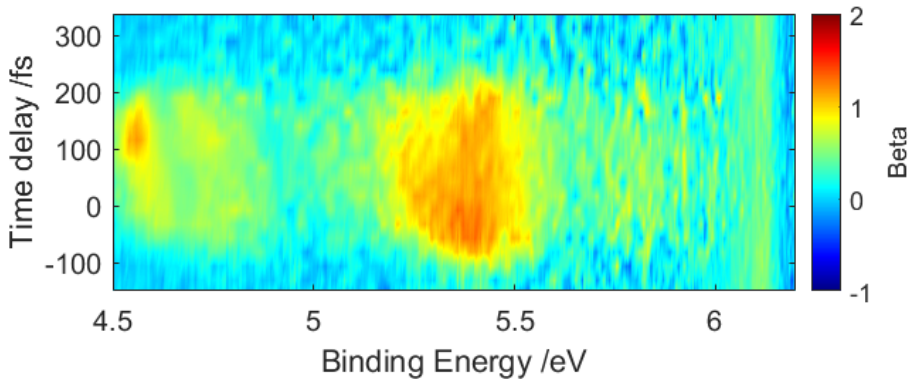


**Figure 4.20:** The $beta_2$ values of the angular distribution of photoelectron following excitation by a 255 nm photon and ionisation by two 395 nm photons. Values are shown as a function of binding energy and pump-probe delay.

### 4.5.1 Decay Associated Spectra

Similarly to the 269 nm the time-dependent spectrum for 255 nm was initially fitted using equation 4.13, using the Levenberg-Marquardt algorithm from MATLAB's *lsqnonlin* function. This equation models the dynamics using a simple kinetic model. To capture the delayed rise and shift we tried using three exponential decays convolved with a Gaussian. It was hoped that 1 exponential decay would describe the decay out of the initial excited state, the second exponential decay would model the decay into a secondary state which is the cause of the later time dynamics and the third would model the decay out of this secondary state. The simulated fit at binding energy 4.66 and 5.62 eV is shown in figure 4.21 a) and b) respectively. The total fit is shown in yellow, with the contributions from the three exponential decays shown in red, blue, and green. The amplitudes of the three exponential decay across the whole spectrum are shown in c), the dashed black lines show the locations of the fits shown in a) and b). The error fraction of the fits for the whole spectrum is shown in d), with blue showing the fits underestimating the signal and red overestimating the signal. This fit has a FWHM of 144 fs which is significantly longer than the FWHM from the 269 nm data and all the lifetimes are below the temporal resolution of the experiment which is defined by the cross-correlation of the two laser pulses. For this fit lifetimes below $\sim$50 fs can not

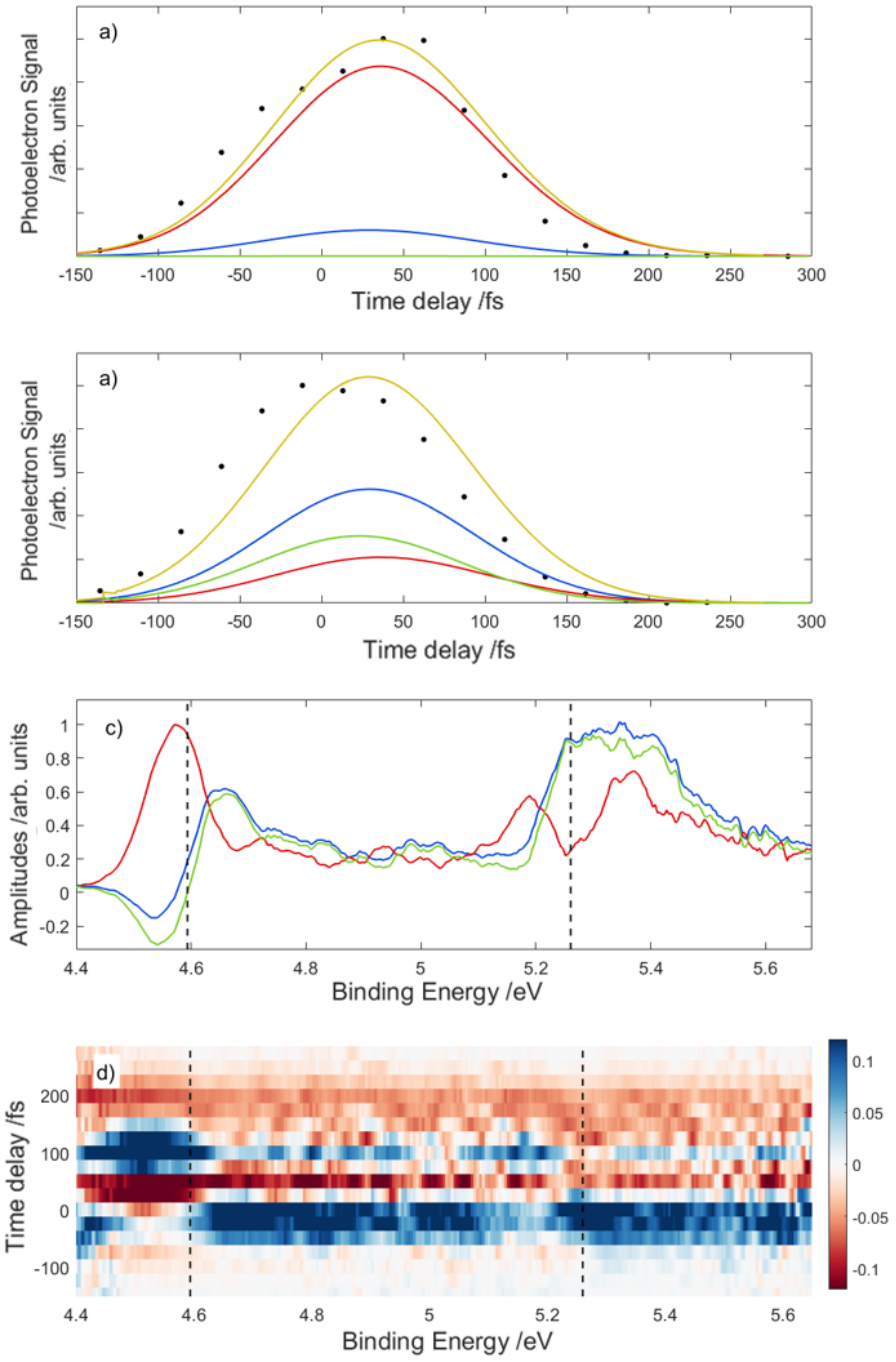


**Figure 4.21:** a)The results of the global fit with three exponential decays (yellow) to the experimental data (black data points) at the energy indicated by the black dashed line on c) and d) with the a) being at the lower binding energy. All the components were convoluted with a Gaussian with a FWHM of 144 fs, and all had lifetimes below the resolution of the experiment. The contribution of the first exponential decay (blue) and the second exponential decay (red) across the entire spectrum is shown in c). The fraction error, with a colour axis between -0.12-0.12 is shown in d). Fraction error is defined as the difference between the signal and simulated value divided by the signal.

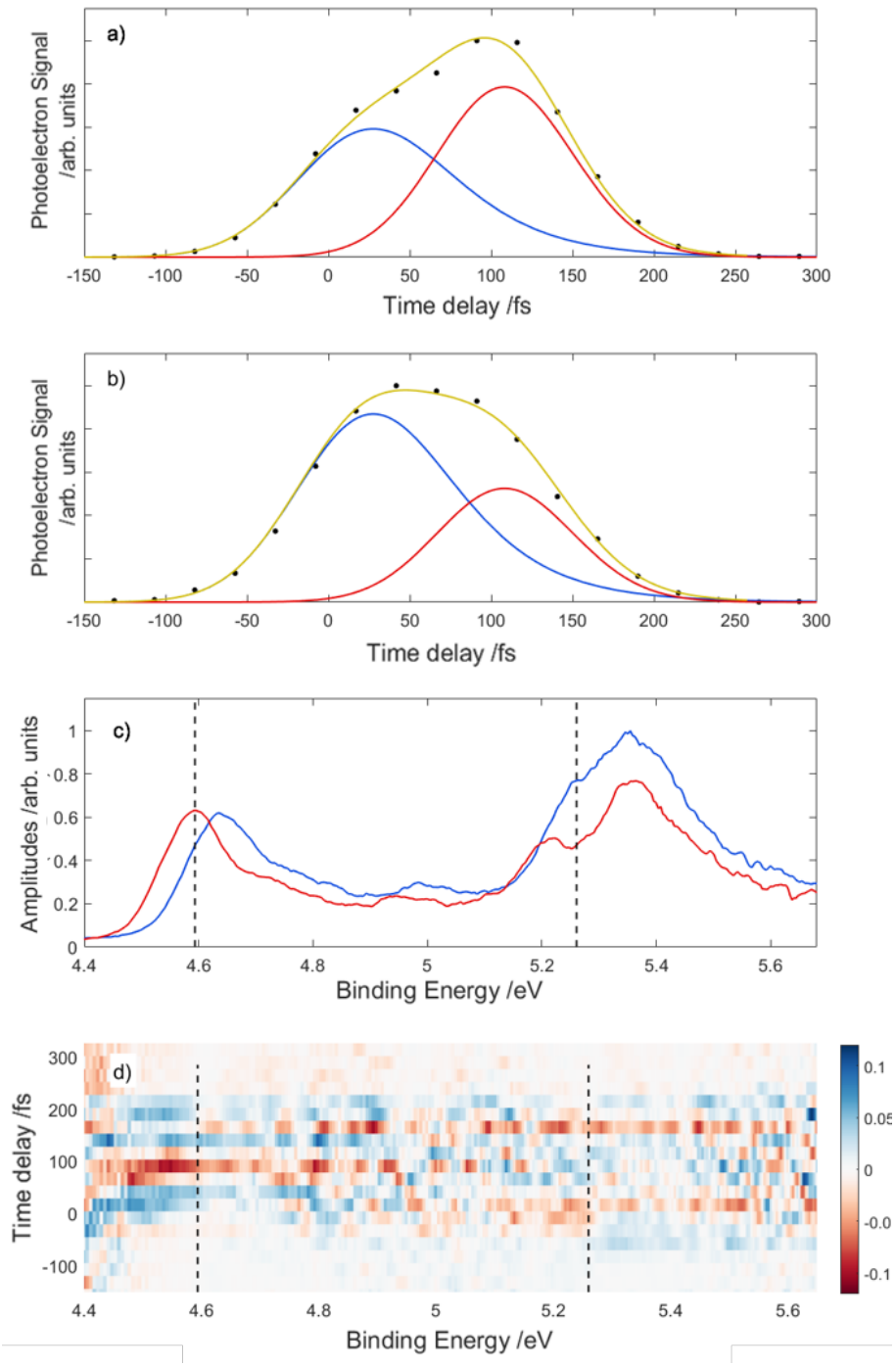


**Figure 4.22:** a)The results of the global fit (yellow) to the experimental data (black data points) at the 4.66 eV, with the contributions from two exponential decays different time-zeros, b) shows the same information as a) but for energy 5.62 eV. The first component (blue) has a lifetime of 40 fs, the second (red), 10 fs. Both a convoluted with a Gaussian with a FWHM of 94 fs. The separation of the two components is 100 fs. The contribution of the two exponential decay with a variable time-zero across the entire spectrum is shown in c). The fraction error, with a colour axis between -0.12-0.12 is shown in d). Fraction error is defined as the difference between the signal and simulated value divided by the signal.

be determined. At late times the fit considerably over-estimates the spectrum intensity while at early times the intensity is considerably underestimated. This structure in the residuals shown in figure 4.21 d) shows that the fit is not a good model of the data. We also observed very similar results for four exponential decays. The simple kinetic model is unable to accurately fit the data due to the changes in Franck-Condon overlap causing shifting energy features and increasing signal strength which results in a delayed peak maximum of the longer lived component.

Therefore a variable time zero for each component was used. Two exponential decays were required to fit the data. Figure 4.22 c) shows the amplitudes of exponential decay across the binding energy. Figure 4.22 a) shows the fit at 4.66 eV where the increased intensity is most apparent and b) shows the fit at 5.62 eV where the first component has larger amplitude. In both figures, the blue is an exponential decay centred at time zero, with a lifetime of 40 fs. The red exponential decay is centred 100 fs later and has a lifetime of 12 fs. Both decays are convolved with the same Gaussian with an FWHM of 94 fs. Figure 4.22 d) show the fraction residuals, the residuals do not show any significant structure showing this model provides a good fit and smaller errors than the fits using single time zero.

## 4.6 Discussion

The 269 nm spectrum shows a lifetime for the exited state to move out of the region of ionisation, BE>6.26 eV, to be 30 fs. The short lifetime is expected due to the steep gradient of the $^3Q_0$ along the $R(C-I)$ and is consistent with other measurements around this wavelength.

The 255 nm time dependent spectrum is significantly different from the 269 nm spectrum. The first exponential decay has a lifetime of 40 fs, similar to the lifetime seen at

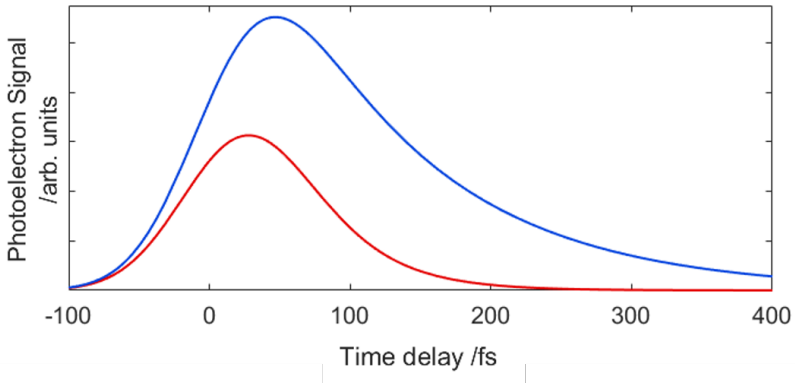


**Figure 4.23:** Example profile of the measured intensity from two equal populations with different lifetimes: 40 fs (red) and 110 fs (blues) but convoluted with the same Gaussian pulse with a FWHM of 144 fs.

269 nm. We therefore suggest that the initial fast decay is due to dynamics similar to those observed at 269 nm on the $^3Q_0$ state.

The second contribution to DAS is of similar intensity but as the laser pulse time duration is not negligible, features with a longer lifetime will appear more intensely due to the ability to build up population. Figure 4.23 shows the intensity difference for a 40 fs and 110 fs lifetime with the same population, ionisation propensity, and detection sensitivities and same convoluted Gaussian with a FWHM of 144 fs. If we model the first feature having a 40 fs lifetime, from the fit and the second feature as having a lifetime of about 110 fs as this is the location the maximum of the feature it is possible to estimate the relative population of the second feature. The second feature appears to be due to a population around 50% the size of that producing the earlier feature. It should be stressed the lifetime of the second feature is a rough guess as we could not fit the data to exponential decays with the same time-zero caused by pump-probe overlap. The purpose of this calculation is to give a ballpark value for the percentage of the population which causes the extended lifetime feature.

Considering the initial excitation step in more detail we see from table 4.1, at 255 nm

there is very little if any excitation into the $^3Q_1$ state therefore the overall dynamics are unlikely due to dynamics on the state. Also if dynamics on the $^3Q_1$ state were responsible for the delayed feature we would expect to also observe it at 269 nm. Three of the four studies predict a non-negligible contribution from $^1Q_1$ state of around 20%. This is still significantly lower than our very rough estimation of 50% however due to the two-photon probe we may be seeing an artificial enhancement of the secondary feature due to a resonant state in the ionisation step. We suggest this extended lifetime may be due to dynamics on the $^1Q_1$ state. Although the $^1Q_1$ state is more dissociative along the $R(C-I)$ coordinate than the $^3Q_0$ state the dynamics may involve motion in other dimensions, however even with higher dimensions included, what dynamics may cause a longer lifetime is not clear from the potential energy curves. The shift to lower binding energy indicates that after excitation the molecule rearranges itself so that at around 100 fs it has a structure closer to the two lowest ion states. It has also been suggested it may be due to a vibrational excitation of the molecule causing the extended lifetime. Results from Murillo-Sánchez [19] showed an increased appearance time for vibrationally excited molecule following excitation by 243 nm. This would be more significant for 255 nm than for 269 nm as the increased energy means vibrational excitation is more likely.

## 4.7 Conclusion

Using a two photon probe we measured the initial dissociation dynamics of methyl iodide following excitation at 269 nm and 255 nm. At 269 nm we observed rapid dissociation, around 30 fs. This is in agreement with previous results and is expected from the potential energy surface of $^3Q_0$. At 255 nm the dynamics are much more complex and show an extended lifetime with a secondary feature appearing at about 100 fs accompanied by a 0.04 eV shift to lower binding energies. We suggest the longer lived dynamics are the result of population on the $^1Q_1$ surface, although the relative intensity of this fea-

ture is significantly larger than expected. It has also been suggested that the extended lifetime observed at 255 nm may be due to an accidental resonance in the ionisation step.

The two-photon probe used in this chapter allows us to measure the initial dynamics with enough spectral resolution to resolve different vibration states of the lowest two ion states. However it doesn't allow the complete dissociation to be observed. Using an XUV probe would allow the full dynamics to be observed as there would be enough energy in the probe to always ionise. An XUV probe would also remove questions about the effect of any accidental resonance in the ionisation process on the observed dynamics and extended lifetimes as well as the relative intensity of the delayed feature as the ionisation step would be a single photon process.

# Chapter 5

# Photoelectron Spectroscopy of the A-Band Dissociation of Methyl Iodide using a XUV Probe

This Chapter is based on work in the published paper: Photodissociation dynamics of methyl iodide across the A-band probed by femtosecond extreme ultraviolet photoelectron spectroscopy, Journal of Physics B, by Briony Downes-Ward, Emily M. Warne, Joanne Woodhouse, Michael A. Parkes, Emma Springate, Philip A. J. Pearcy, Yu Zhang, Gabriel Karras, Adam S. Wyatt, Richard T. Chapman and Russell S. Minns[151]. RSM designed the experiment. EMW, BDW, RSM, JW, MAP, RTC, ASW, PP, YZ and GK performed the experiment, and RTC, ASW, ES, PM, YZ and GK manage and run the Artemis laser facility and supported the experiment. EMW, BDW, RSM and JW analysed and modelled the experimental data. EMW focused on analysing the data at 269 nm while BDW focused on the analysis of the data from the 254 nm and 243 nm pump and analysis of 279 nm was shared between both of us. Therefore this chapter does not focus on the data 269 nm but the other three wavelengths, however the 269 nm is present to provide a comparison and completeness of discussion. A more comprehensive analysis of the 269 nm data can be found in EMW thesis [117] and in paper [152].

## 5.1 Introduction

The previous chapter discussed results from a time-resolved photoelectron spectroscopy (TRPES) experiment which studied the dissociation dynamics of the A-band of methyl iodide. In the previous experiment we used two pump wavelengths of 269 and 255 nm and the dynamics were then probed using two photon absorption of 395 nm. In this chapter I present a complementary study in which we probed the A-band of methyl iodide using TRPES but this time we used four wavelengths (279, 269, 254 and 243 nm) to cover a wider range of the central A-band than the previous experiments as shown in figure 5.1. We also changed the probe to use a 54.9 nm (22.6 eV) probe. This is the 7th harmonic of 400 nm (chapter 3 focused on 20.4 eV as an 800 nm driving laser was being used). The previous multiphoton probe with a total energy of 6.28 eV meant that only the initial excited state could be observed but this time with a higher probe energy the dissociation dynamics could be followed to cover geometries with higher binding energies.

A review of the current literature on the study of the A-band of $CH_3I$ has been presented in the previous chapter. Figure 5.1 shows the 1D potential energy surfaces of the 3 optical allowed transitions in the A-band of methyl iodide, $^1Q_1$, $^3Q_0$ and $^3Q_1$. All three potential energy curves shown are strongly dissociative and therefore we expect rapid dissociation of the C-I bond on excitation to the A-band and this is what has previously been observed at 268\266 nm [22, 129, 19] and what we observed at 269 nm with our two-photon ionisation TRPES results. However our results at 255 nm showed significantly different dynamics with an increase in intensity after 100 fs well after the dissociation is expected to be completed [12].

The inset in figure 5.1 shows the overall absorption curve [131] and the location of the 4 pump wavelengths. At the centre of the absorption band (258 nm) the large majority of excitation is into the $^3Q_0$ state. However the relative contribution of the 3 states to

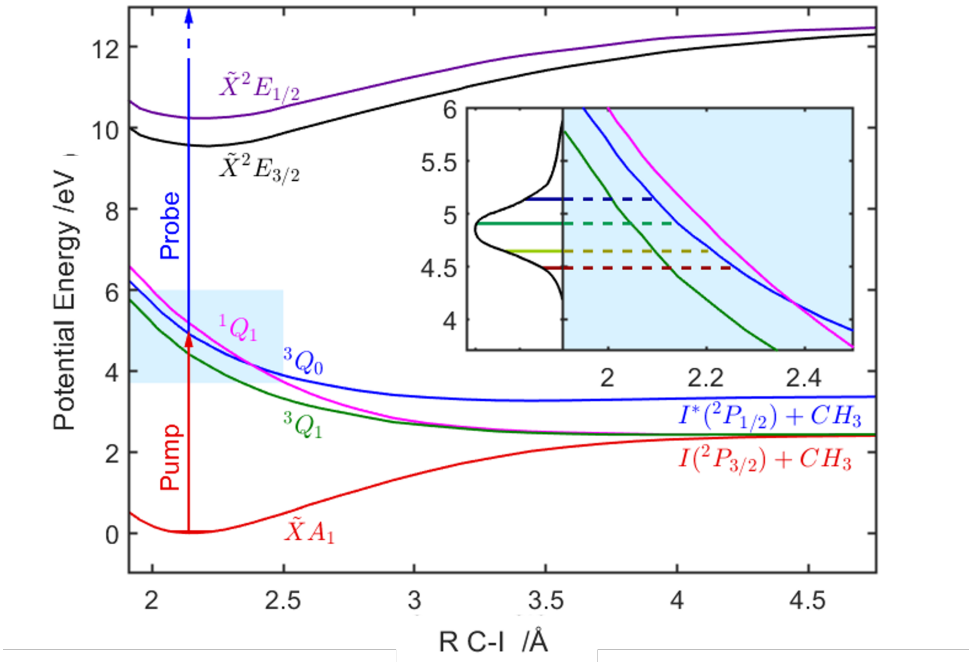


**Figure 5.1:** 1-D cuts along the C-I dissociation coordinate of the potential energy surfaces of $CH_3I$ relevant to the UV photodissociation and photoelectron detection scheme used. Inset: expanded figure of the excited state potentials and the total absorption spectrum of methyl iodide with the location of each pump wavelength marked. The ground state energy curves are taken from [127] and the cation states are taken from [128]. The overall absorption curve is taken from [14].

the overall absorption curve is uncertain and has been discussed in detail in section 4.1.1.

With this new experiment it is hoped to answer some of the questions raised by the previous experiment. The single XUV photon will provide information on the effect, if any, of the probe on the observed dynamics as accidental resonance will no longer occur. The XUV photon also extends the window of observation allowing us to follow the dissociation until the onset of the ground state peaks. By also exciting with 243 nm this will help to understand whether this extended and more complex dynamics is continued to be observed at shorter wavelengths with greater energy and absorption into the $^1Q_1$ state. The different excitation fractions from published experimental and theoretical results for the four pump wavelengths used in this experiment are shown in table 5.1 .

| | 243 nm | | | 254 nm | | |
|---|---|---|---|---|---|---|
| | $^3Q_0$ | $^1Q_1$ | $^3Q_1$ | $^3Q_0$ | $^1Q_1$ | $^3Q_1$ |
| magnetic circular dichroism[144] | 50.0% | 50.0% | 0% | 86.0% | 14.0% | 0% |
| product state angular distributions[14] | 97.9% | 2.1% | 0% | 99.5% | 0.5% | 0% |
| wave packet calculations[132] | 60.4% | 34.5% | 5.1% | 80.5% | 14.2% | 5.3% |
| multireference configuration interaction[9] | 50.0% | 50.0% | 0% | 75.3% | 23.9% | 1.8% |
| | 269 nm | | | 279 nm | | |
| | $^3Q_0$ | $^1Q_1$ | $^3Q_1$ | $^3Q_0$ | $^1Q_1$ | $^3Q_1$ |
| magnetic circular dichroism[144] | 96.7% | 3.3% | 0% | 100% | 0% | 0% |
| product state angular distributions[14] | 100% | 0% | 0% | 100% | 0% | 0% |
| wave packet calculations[132] | 81.7% | 5.1% | 13.3% | 70.1% | 2.5% | 26.8% |
| multireference configuration interaction[9] | 81.6% | 8.0% | 10.3% | 67.0% | 0.0% | 33.0% |

**Table 5.1:** Percentage excitation fraction at the four wavelengths studied based on published experiment and theory

The time-resolved XUV photoelectron spectra following excitation by 279, 269, 254 and 243 nm are presented and discussed in this chapter along with a comparison to the previous two-photon ionisation experiment which was presented in the previous chapter.

## 5.2 Experimental

This experiment was carried out at the Artemis laser facility with the general set-up for a TRPES experiment described in detail in chapter 2. The specifics of this experiment will be described below.

From the OPA we generated four wavelengths, 279 nm (4.45 eV), 269 nm (4.61 eV), 254 nm (4.87 eV) and 243 nm (5.10 eV) with pulse energies of 2.8$\mu$J (279 nm), 3.7 $\mu$J (269 nm), 2.2$\mu$J (254 nm) and 1.5$\mu$J (243 nm). The wavelengths are chosen to cover both the red and blue sides of the A-band absorption maximum (258 nm) of methyl iodide. The probe is generated via high harmonic generation using approximately 450 $\mu$J of the second harmonic, 395 nm. The 7th harmonic (54.9 nm, 22.6 eV) is isolated using a time preserving monochromator. The pump is focused into the vacuum chambers by

a 1 m convex mirror and directed into the interaction region by a D-shaped mirror. The XUV beam is focused into the interaction by a toroidal mirror with a 1 m focal length which is located behind the D-Shaped mirror. The beams are overlapped by looking at a scintillator crystal. The scintillator crystal luminescence when hit by the laser allowing for spatial overlap between the two laser pulses to be achieved.

The $CH_3I$ was introduced into the chamber by an effusive expansion of the room temperature $CH_3I$ vapour through a 200 $\mu$m nozzle. The electrons were collected by an electron time-of-flight (TOF) spectrometer as opposed to velocity map imaging (VMI) due to the low signal levels expected from the excited state of $CH_3I$. This is due to the XUV flux being much lower than the UV probe used in the previous chapter and because the cross section of ionisation for a molecule reduces as the excess probe energy above the ionisation energy increases. A TOF spectrometer has better signal to noise resolution than a VMI spectrometer. In a VMI electrons with the same kinetic energies will hit the detector at different radii and angles depending on the angle it was emitted, this allows information on the angular distribution to be extracted however this spreads out the signal meaning there is great noise in the overall signal resulting in worse signal to noise resolution. In a TOF only the arrival time of the electrons are recorded and all electrons on the same kinetic energy have the same arrival time meaning the signal is not spread out, resulting in better signal to noise resolution. The drift tube of the TOF spectrometer did not have a voltage applied, while the lens was held at 100 V. A schematic of the TOF is shown in figure 5.2. The voltage on the MCP was 1.8 kV.

The signal from the electrons hitting the MCP at the end of the TOF is amplified and then sent to a constant fraction discriminator (CFD). This attenuates the signal by a constant fraction. It also takes a copy of the input signal and inverts it and delays it by 1.25 ns (greater than the rise time of the signal). The attenuated and inverted/delayed signals are added to produce a signal that crosses zero at a time independent of the

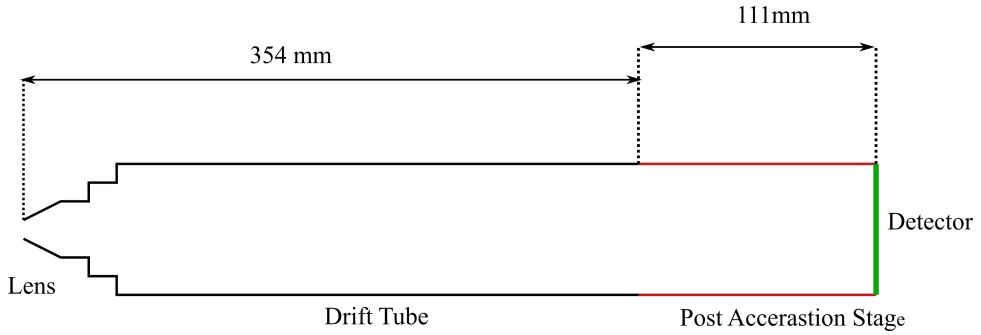


**Figure 5.2:** A schematic of the electron TOF. With the lens a drift tube followed by a post acceleration stage which rapidly accelerate the electrons toward the detector. The acceleration stage is not included in the distance the traveled by the electron.

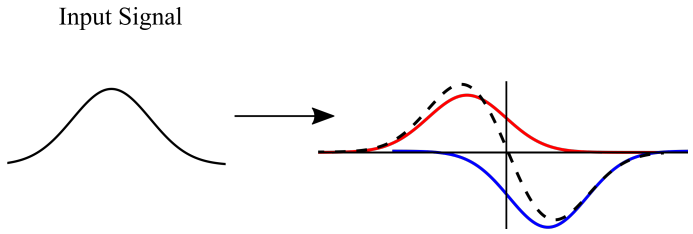


**Figure 5.3:** The input signal to a CFD. The red line is the signal after being attenuated. The blue line shows the inverted and delayed signal. The black dashed line is the sum of both signal which crosses zeros independently of the amplitude of the initial input signal.

amplitude of the initial input signal. This process is shown in figure 5.3. The CFD output is sent to a time-to-digital converter (TDC) to digitise the signal. The TDC starts measuring when triggered by the laser pulse using a fast photodiode. It then stops measuring when the signal from the CFD arrives. This then results in a list of times electrons hit the MCP.

The photoelectron spectra were recorded for delays -200-500 fs in 25 fs time steps. Each spectrum, at each delay point was collected for 1 s (1000 laser shots). The delays were recorded for -200-500 fs before moving back to -200 fs and cycling through all the delays again, this is done to avoid systematic errors due to changes in experimental conditions such as laser power drop, decreases of $CH_3I$ pressure or shifts in alignments of laser beams. The delay times were cycled through 2004, 2007, 2770, 5200 times for 279, 269, 254, and 243 nm respectively

## 5.3 Initial Data Analysis

The raw data is a list of electron arrival times and the corresponding electron count, an example is shown in figure 5.4 a). The arrival times have a constant but arbitrary time offset. The electron arrival times are converted to binding energy using the equation,

$$\begin{aligned} BE &= E_{probe} - KE \\ &= E_{probe} - \frac{1}{2} m_e v^2 \\ &= E_{probe} - \frac{1}{2} m_e \left( \frac{d}{t_{tdc} - t_{offset}} \right)^2 \end{aligned} \tag{5.1}$$

where $E_{probe}$ is the energy of the probe photon (eV), $KE$ is the kinetic energy of the electron, $m_e$ is the electron mass (eV/$c^2$), $d$ is the length of the electron flight (m), $t_{tdc}$ is the time outputted from the TDC (converted from ns to s) and $t_{offset}$ is the time the electron are created, e.g. when the XUV laser pulse arrives at the interaction region.

A few photons from the laser pulses reach the detector and as photons travel a lot faster than electrons their arrival time is used for $t_{offset}$. The small peak due to these photons is shown in the log plot in figure 5.4 b) at a TDC time of 268.2 ns.

Both $E_{probe}$ and $d$ are known approximately but their exact values are determined from the data. $E_{probe}$ is roughly the 7th harmonic of 395 nm but the exact value will depend on various factors such as phase matching conditions. $d$ is roughly the length of the spectrometer which is known but does depend on the exact position the lasers and methyl iodide sample interact, e.g. where the photoelectrons are born.

To obtain exact values for these two variables we used sharp peaks in the spectrum which have known values. Methyl iodide has two sharp peaks at 9.53 and 10.12 eV which could be used. Most spectra also had peaks from nitrogen (probable due to a small air leak in

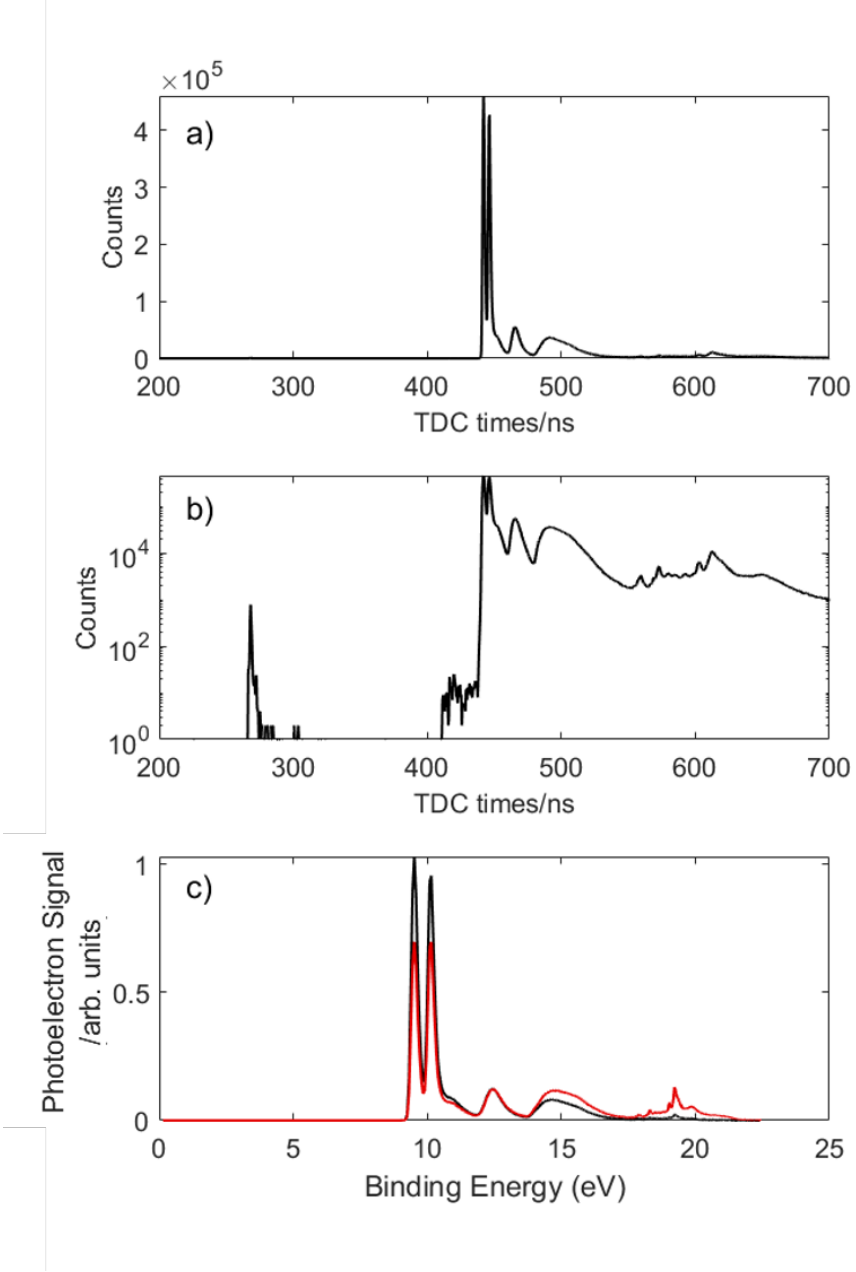


**Figure 5.4:** a) the raw data from a single delay showing the electron counts from the MCP against their arrival time from the TDC. The TDC times are offset from the electron flight time be a constant value. b) shows the same data as a) but on a log scale. At 268.2 ns there is a spike due to photons from the laser pulse. This is used for the time offset of the TDC times. At ∼420 ns we also observe signal due to excited state dynamics. c) shows the same data again but now in binding energy. Black shows the data before the Jacobian had been applied and red after. In this figure both curves have the same area.

the sample gas line), we therefore also used a peak from nitrogen at 15.6 eV to widen the energy range. For those results without nitrogen the TDC times of the two methyl iodide peaks were compared to those results with a nitrogen peak and were found to be identical to one of the fits therefore the values from the fit with nitrogen were used. To confirm our fits we plotted each spectrum over the spectrum from reference [147] and the spectra were found to match well.

When converting between TDC time to energy the Jacobian of equation 5.1 needs to be included to keep the area of the graph the same. The raw data is in counts per nanosecond but the calibrated data is counts per eV. Therefore we need to convert from $dt$ to $dBE$. From differentiating equation 5.1 we know $dBE \propto dt/t^3$. Therefore to convert the data to counts per eV we need to multiply by $t^3$. As all other factors are constant across the spectrum they can be ignored as they will have no effect on relative intensities.

## 5.4 Results

### 5.4.1 Ground State Spectrum

The photoelectron spectrum associated with ionisation of the ground state of methyl iodide with a 22.6 eV photon is shown in figure 5.5. There are a number of peaks due to ionisation into many cation states. There are two sharp features at 9.53 eV and 10.12 eV corresponding to the removal of a non-bonding electron on the iodine. This results in ionisation into the spin-orbit split ground state of the cation, $\tilde{X}^2E_{3/2}$ and $\tilde{X}^2E_{1/2}$ respectively. The next broad peak at approximately 12.5 eV is due to the removal of an electron from the highest C-I bonding orbital, the results of ionisation into the $\tilde{A}^2A_1$ ion state. There are many more higher energy cation states and peaks due to ionisation into some of them can be observed at higher binding energies in figure 5.5.

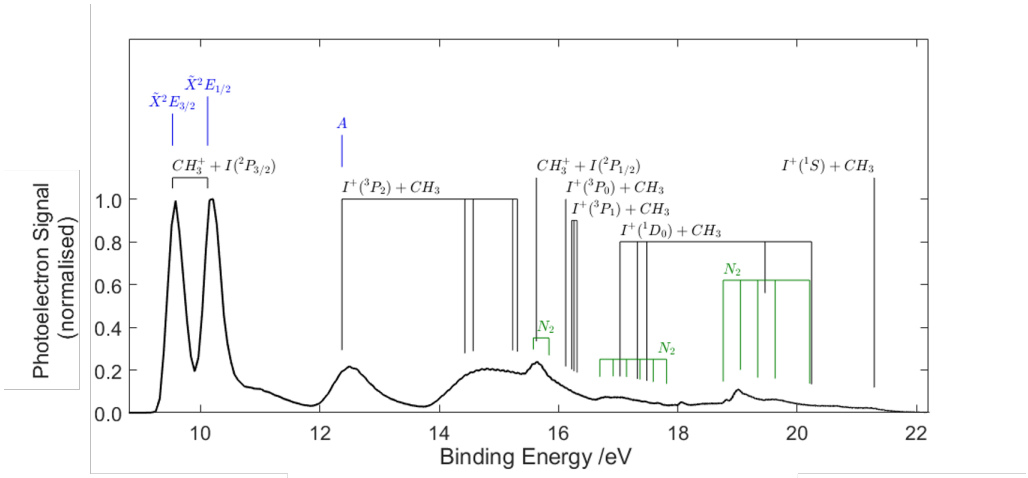


**Figure 5.5:** The ground state photoelectron spectrum from ionization by 22.6 eV. The intensity has been normalised so the most intense peak is 1 and has been summed overall delay times. The black combs are the peaks due to $CH_3I$ and have been labelled with the dissociation products. The combs for the peaks at 9.53 and 10.12 eV are taken from [147] while the rest are taken from calculations of the cation states from [153]. If known the peaks have also been labeled with their final ion state symmetry. The green combs are the locations of peaks due to $N_2$ and the location of the combs are taken from [147]. Combs are marked for all cation states even when there is no apparent corresponding feature.

The green combs indicate the location of peaks resulting in ionisation from residual $N_2$ gas. We observe three $N_2$ bands, the result of ionisation of electrons from the $3\sigma_g$, $1\pi_u$ and $2\sigma_u^*$ orbitals, in increasing binding energy order.

### 5.4.2 Excited State Dynamics

Figure 5.6 shows the excited state photoelectron spectrum at t=10 fs (the closest spectrum to time-zero) following excitation by 279 nm and ionisation by 54.9 nm. The neutral excited state electron configuration is $(\sigma)^2(n)^3(\sigma^\star)^1$. At >8.9 eV we observe the onset of the first ground state peak of $CH_3I$. We also observe three excited state peaks. The two lowest binding energy peaks at 5.3 eV and 5.9 eV correspond to the removal of the $(\sigma^\star)$ electron and ionisation of the molecule in its Franck-Condon geometry into the two spin orbit states of the ground electronic state of the cation, $\tilde{X}^2E_{3/2}$ and $\tilde{X}^2E_{1/2}$ respectively. The third peak at 8.1 eV corresponds to the removal of an electron from the non-bonding orbital localized on the iodine atom, leading to the population of a

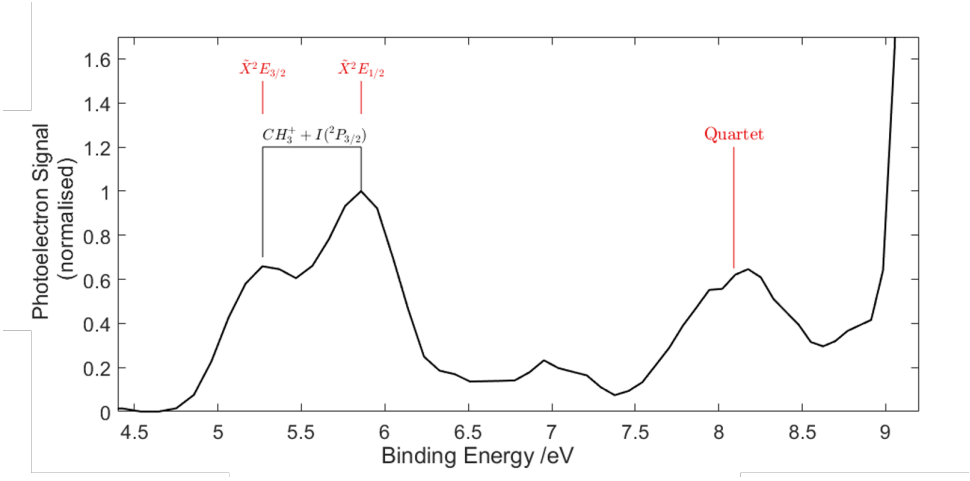


**Figure 5.6:** The excited state photoelectron spectrum following excitation by a 279 nm pulse and ionisation by 22.6 eV. The spectrum is the closest result to time zero (t=10 fs). The intensity has been normalised so the most intense excited state peak has a maximum intensity of 1. At >9 eV there is the onset of the first ground state peak of $CH_3I$. States are labelled with final ion state symmetry and asymptotic products were known.

quartet cation state upon ionisation.

Figure 5.7 shows the time dependent photoelectron spectra following excitation into the A-band of $CH_3I$ at 279 nm (4.45 eV,a), 269 nm (4.61 eV,b), 254 nm (4.87 eV,c) and 243 nm (5.10 eV,d) and subsequent ionisation with a 54.9 nm (22.6 eV) probe. Around time zero all spectra show the three peaks observed in figure 5.6. Two intense peaks below 6 eV that are separated by about 0.5 eV, corresponds to the electron ground state of the cation $\tilde{X}^2E_{3/2}$ and $\tilde{X}^2E_{1/2}$. The third weaker, broader peak is around $\sim$ 7-8 eV is the result of ionisation into a quartet cation state. The centre of the three peaks are indicated by the white dashed lines on each spectrum.

At 279 nm, 269 nm and 243 nm we observe qualitatively similar spectra, a rapid decay of signal out of the binding energy region associated with ionisation from the Franck-Condon (FC) geometry into the $\tilde{X}$ cation state and a time dependent shift to higher binding energy at the later time associated with an increased C-I bond length. This suggests that the underlying dynamics for all three pump wavelengths are similar and

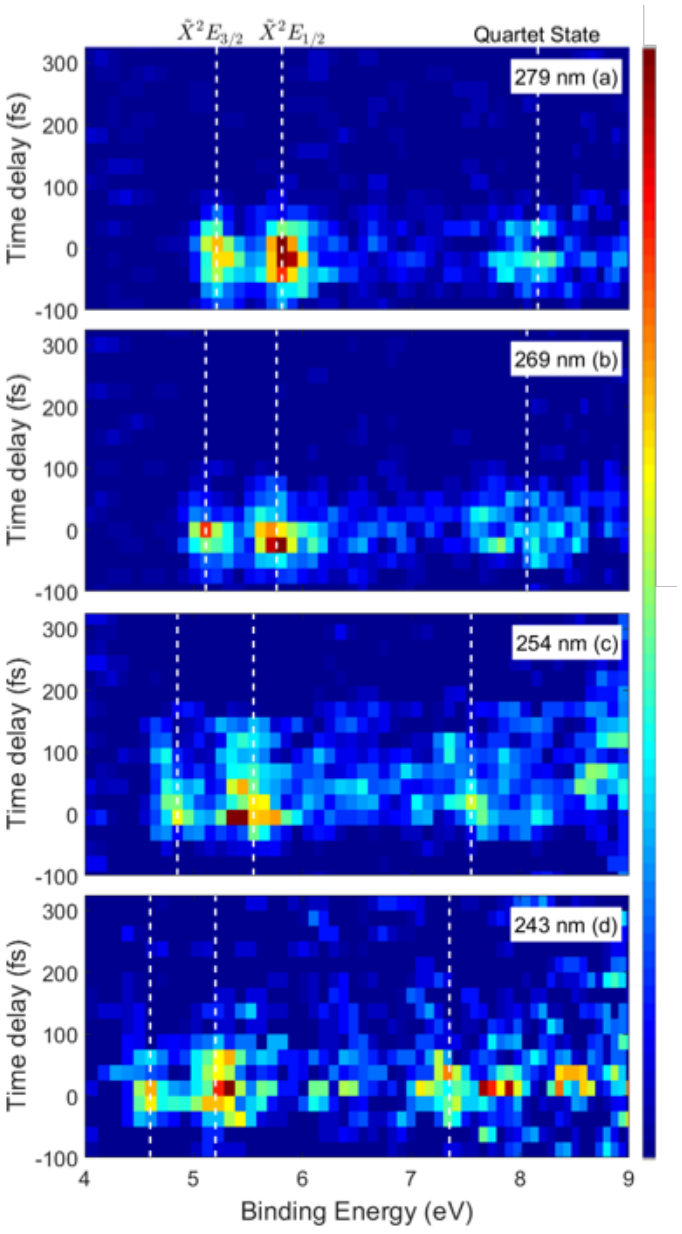


**Figure 5.7:** Time dependent photoelectron spectrum of $CH_3I$ following excitation at 279 nm (a), 269 nm (b), 254 nm (c) and 243 nm (d).The dashed white lines indicate the position of the initial peaks associated with ionisation into the ground and quartet cation states. The location of the dashed lines are from the peak location in the data.

are consistent with the rapid dissociation expected. At 254 nm the spectra show a very different behavior. The time dependent photoelectron spectrum between 4-6 eV however is very similar to the two-photon ionisation results at 255 nm presented in the previous chapter, showing an extended lifetime and a delayed secondary feature appearing at about 100 fs.

Figure 5.8 shows the intensity profile over the peaks in the spectra related to ionisation into the $\tilde{X}$ cation state from the FC geometry for all for pump wavelengths. This is over a binding energy range 4.91-6.14 eV, 4.96-5.95 eV, 4.70 -5.70 eV and 4.55-5.38 eV for the 279 nm (a), 269 nm (b), 254 nm (c) and 243 nm (d) data respectively. The inserts in b) and c) are the fits over the same region for the two-photon ionisation results.

To determine the errors in the data we used bootstrapping analysis. As the data was saved every 10 cycles we could split the data into data sets of 10 cycles. From these small data sets, we randomly selected the data to create a data set with an equal number of cycles to the original data. The small data set of 10 cycles can be selected multiple times when creating these new big data sets. We create 10,000 big data sets from which a standard deviation can be calculated. The error bars in figure 5.8 are from this bootstrapping analysis and shows the 95% confidence interval.

Again the data was fitted to exponential decays convolved with a Gaussian. The equation is given as a sum of,

$$I = A_i e^{-\lambda_i \Delta t} e^{\frac{(\sigma\lambda_i)^2}{2}} \left(1 + \mathrm{erf}\left(\frac{\Delta t - \sigma^2\lambda_i}{\sqrt{2}\sigma}\right)\right) + y_0, \tag{5.2}$$

where $A_i$ is the amplitude. $\lambda_i$ is the decay constant, $\Delta t$ is $t - t_0$, the pump-probe time delay and $\sigma$ is the cross-correlation of the pump-probe laser pulses. $y_0$ is the offset of the baseline which is not exactly zero. The intensity profile of 279 (a), 269 (b) and

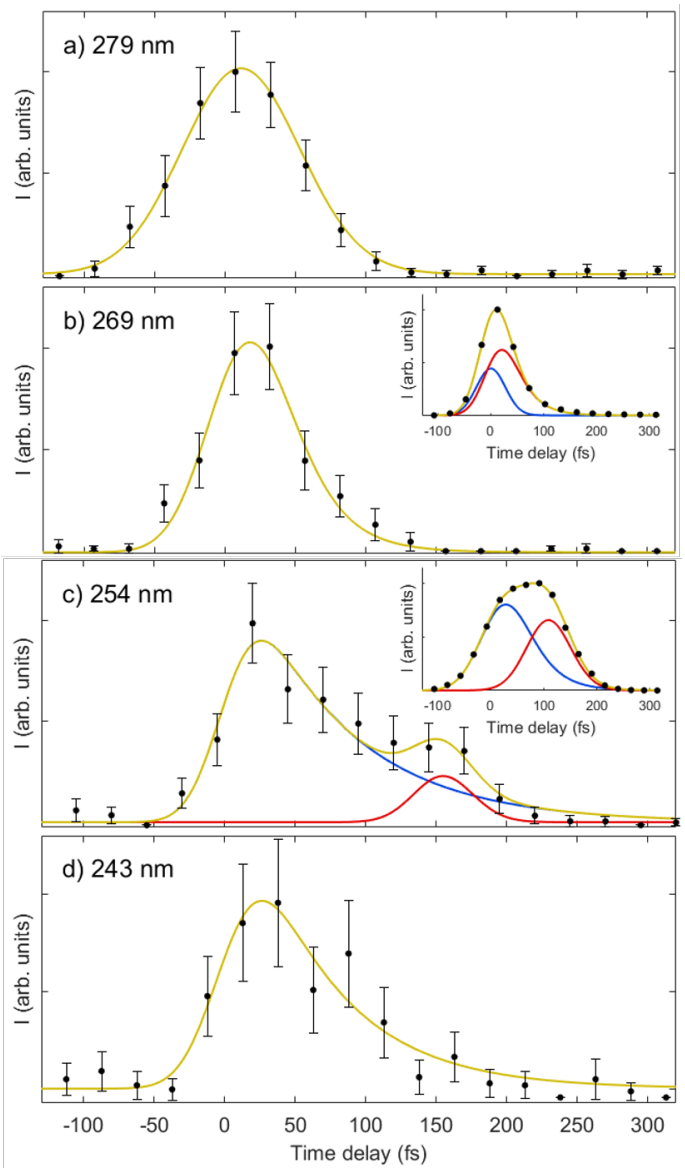


**Figure 5.8:** The photoelectron intensity profile (black data points) over the $\tilde{X}$ state for 279 nm (a), 269 nm (b), 254 nm (c), 243 nm (d), covering binding energy regions 4.91-6.14 eV, 4.96-5.95 eV, 4.70-5.70 eV and 4.55-5.38 eV respectively. Data error bars mark the 95% confidence interval and are obtained from bootstrapping analysis. The yellow line is the fit to the data. For a), b), d) this is an exponential decay, while for c) this is two exponential decays with variable time zero. The two decays are also plotted with the blue and red curves. The insets in b) and c) are the fits and data for the same binding energy region from the two-photon ionisation results. The fits use the same model as the single photon ionisation results[12]. The values for the fits are presented in table 5.2.

243 nm (d) could all be fitted to a single exponential term while 254 nm (c) was fitted with two exponential terms with a variable $t_0$. From figure 5.7 and 5.8 it appears that 279 nm is longer lived than 269 nm, this is misleading as it is actually due to a much longer pulse duration for 279 nm than 269 nm as shown in table 5.2. The errors on the fit are quoted for 1 standard deviation and are obtained from bootstrapping analysis in which 1,000 data sets were created and fitted. These data sets are different from those used to determine the error on the data point however they are consistent, having the same mean and standard deviations. We used a smaller number of data sets due to the increased computational cost of fitting the data. The cross-correlation of the pump-probe laser pulses with the 279 nm pump has a FWHM of 87$\pm$9 fs that means we obtain the best fit with lifetimes below the resolution of our experiment, putting an upper limit on the lifetime of the wavepacket moving out off the Frank-Condon region of $<$25 fs.

At 269 nm the FWHM is 60$\pm$8 fs, this meant we could obtain a lifetime of the excited state peak to be 23$\pm$6 fs. Fitting to 243 nm data gave a FWHM of 57$\pm$20 fs and a lifetime of 46$\pm$14 fs. This is a longer lifetime than the longer pump wavelength, however the data is still accurately described by a single exponent decay and suggests the excited state population rapidly dissociates at this short wavelength too. For these three wavelengths, although slightly different lifetimes are measured, the observations are all consistent with the rapid movement of the population out of the Franck-Condon region which is accurately described by a single exponential decay. This suggests the dynamics are roughly similar at the three wavelengths

The intensity profile for 254 nm over the binding energy region associated with initial excitation to the $\tilde{X}$ cation (4.70-5.70 eV) is shown in figure 5.8 c) is significantly different from the intensity profile for the other three wavelengths with significant intensity out past ionisation 150 fs. This data could not be accurately modelled with a single exponential decay. We fitted the data using the same model as the previous two-photon-

results presented in chapter 4, two exponential decays with the same cross-correlation and variable time-zeros. It should be stressed this is a purely empirical model which allows comparison between the two measurements but care should be taken when extracting mechanistic information from the numbers alone. From the fit we obtain a FWHM of 77$\pm$27 fs and separation of the two features of 114$\pm$38 fs. The first feature has a lifetime of 52$\pm$23 fs, while the lifetime of the second feature was below the resolution of the experiment giving an upper limit of $<$20 fs

The error on the fit for 254 nm is larger than the fits for 279 nm and 269 nm where there is a similar level of noise due to the increased number of variables for the fit. We see a significant cross-talk between the variables, in particular the FWHM and the lifetime of the first feature. Figure 5.9 shows the distribution of the FWHM and $\tau_1$ for 888 fits to the initially excited state feature caused by ionisation into the $\tilde{X}$ cation states of 254 nm. We ran a 1000 fits but excluded fits that did not converge or had a FWHM of less than 30 fs as this was deemed too short to be physical given the length of the laser pulses produced by the TOPAS. We observed two different possible fits, either a short FWHM and a long lifetime or a longer FWHM and shorter lifetime. Although we can't rule out either possibility we suspect the longer FWHM and short lifetime is more suitable for the experiment as the other solution produces very short pulses which would be surprising compared with the FWHM from the other three pump wavelengths. The short lifetime is also consistent with the two-photon ionisation results which due to the better signal to noise ratio did not have the issue with fitting the data.

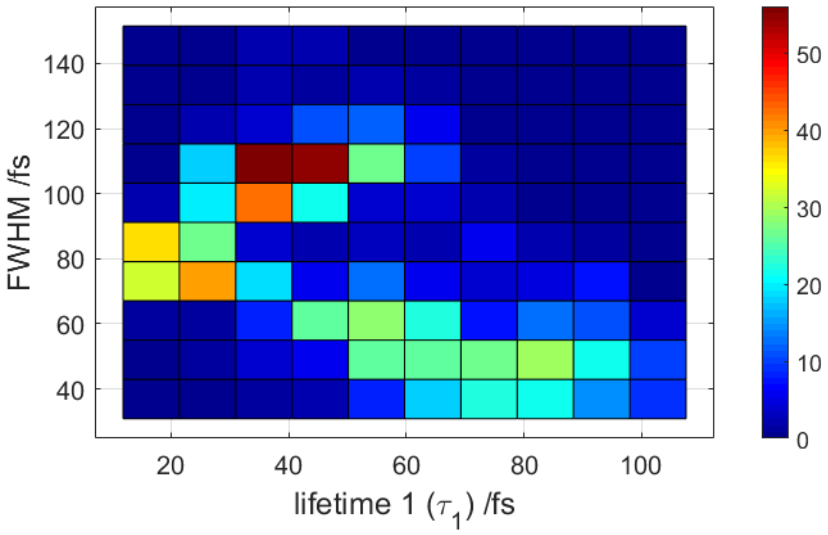


**Figure 5.9:** The distribution and relationship of sigma and first lifetime for the fits of two exponential decays convoluted with a Gaussian to the time profile of FC region of the 254 nm photoelectron spectrum for 888 fits which successfully converged and have a sigma great than 13 fs. The colour scale is the number of fits in each bin.

### 5.4.3 Comparison to the Two-Photon Ionisation Results

To compare the XUV result with the previous two-photon ionisation results we plot the time-dependent photoelectron spectrum following ionisation at 254/255 nm together. Figure 5.10 shows the two photon and XUV time dependent photoelectron spectra in a) and b) respectively. Both data have the same time step but the two photon ionisation

| Probe-XUV | | | | | Probe-MPI[12] | | | | |
|---|---|---|---|---|---|---|---|---|---|
| Wave-length/nm | FWHM/fs | $\tau_1$/fs | $\tau_2$/fs | $\Delta t$/fs | Wave-length/nm | FWHM/fs | $\tau_1$/fs | $\tau_2$/fs | $\Delta t$/fs |
| 279 | 87±9 | <25 | - | - | - | - | - | - | - |
| 269 | 60±8 | 23±6 | - | - | 269 | 64 | 32 | - | - |
| 254 | 77±27 | 52±23 | <20 | 114±38 | 255 | 94 | 40 | 12 | 97 |
| 243 | 57±20 | 46±14 | - | - | - | - | - | - | - |

**Table 5.2:** Fit parameters for the observation time constants and delays for the Franck-Condon regions obtained in the XUV and two photon ionisation experiments. The data has been fitted to exponential decays convoluted with a Gaussian. The fits are shown in figure 5.8. The fits are over the binding regions 4.91-6.14 eV, 4.96-5.95 eV, 4.70 -5.70 eV and 4.55-5.38 eV for the 279 nm , 269 nm , 254 nm and 243 nm data respectively. The errors are 1 standard deviation and are calculated using bootstrapping analysis.

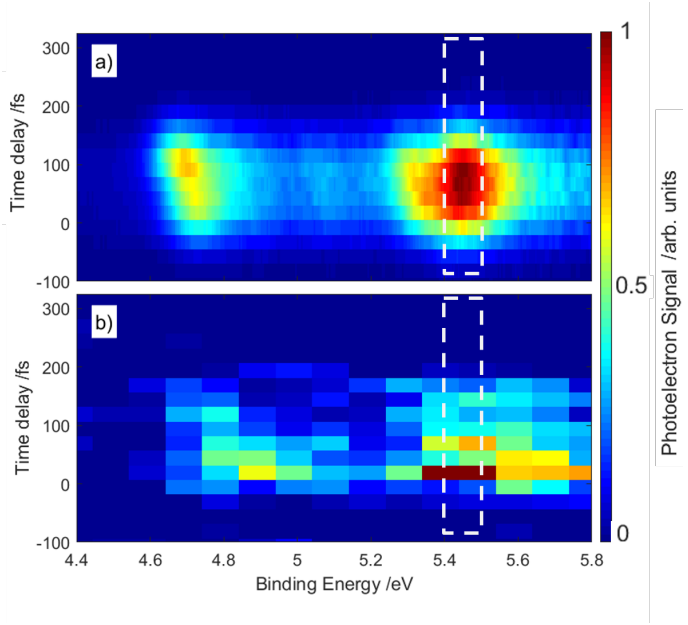


**Figure 5.10:** Time dependent photoelectron spectrum of $CH_3I$ following excitation at 255 nm and probed using a multiphoton ionisation(a), and at 254 nm and probed using single photon XUV ionisation (b).

results have significantly better energy resolution than the XUV results, 0.005 eV compared to 0.1 eV. The resolution of the two photon ionisation results is determined by the pixel spacing, the XUV resolution is determined by the TOF binning size. The difference in resolution is mainly due to much lower electron energy $\sim$1 eV measured in the two photon ionisation experiments as opposed to the $\sim$17 eV electron energy measured during the XUV experiments. Despite the energy resolution difference there are a number of similarities. Both show significant intensity out to almost 200 fs, much longer than all other wavelengths measured. The two photon ionisation data shows an initial energy shift to a slightly lower binding energy. The shift of approximately 0.04 eV is smaller than the energy resolution of XUV data, however, as the pulse has a finite energy width we do see a shift in the centre of the photoelectron peaks in the XUV data to lower binding energies that matches the observations in the two photon ionisation data. The long lived feature at 5.5 eV which does not shift in binding energy in the two photon ionisation result was previously assigned to $\tilde{X}^2 E_{3/2}\,\nu_2^2$ with ionisation through a Rydberg state which is shown by the dashed white box in figure 5.10. The XUV data does not

have the energy resolution to separate this feature from the $\tilde{X}^2E_{1/2}$ peak however we do not see any unexpected enhancement of the peak supporting our initial assignment. The values to the empirical fits used for both data sets are shown in table 5.2. All comparable values from the fits of the two data sets are the same within error, showing consistency between measurements. The similarity of the spectra and lifetimes obtained and separation of the two features suggest that extended excited state lifetime is the result of dynamics of $CH_3I$ on the A-band and not the consequence of any accidental resonance during the ionisation process. However, the multiple ionisation process appears to have artificially enhanced the secondary feature. Therefore our previous estimation of the relative population of the secondary feature being 50% appears to be a significant overestimation.

We repeat the rough calculation previously used to estimate the relative population of the secondary feature in the two photon ionisation results using the intensity from the XUV results. Using the same variables as before, a lifetime of 40 fs and 110 fs, we obtain a value of around 10%. This is much closer to the value for the contribution of the $^1Q_1$ state to the overall absorption at 254 nm for three out of four of the papers shown in table 5.1. The results from the product state angular distributions [14] is the only paper that suggests a significantly lower contribution of about 2%.

### 5.4.4 Longer Term Dynamics

To analyse the shift of the signal to higher binding energy the intensity profile as a function of time over a few different binding energy regions was plotted as shown in figure 5.11. The bottom line out (green), labelled $\tilde{X}$ is over the energy region associated with ionisation from the FC geometry, the same as plots in figure 5.8. The second row (teal) is after the binding energy region $\tilde{X}$ and just before the onset of the quartet state. The third row (blue), labeled $Q$ is over the quartet state. The fourth region (purple) is binding energies between the quartet state and the onset of the ground state features. The

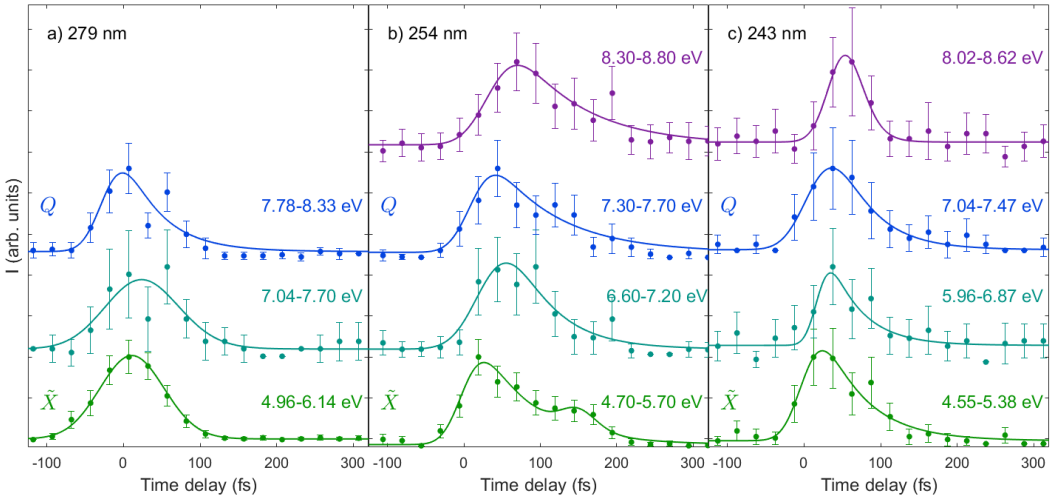


**Figure 5.11:** Integrated photoelectron intensity over a number of binding energy regions as labelled for pump wavelengths of 279 nm (a), 254 nm (b) and 243 nm (c). The error bars mark the 95% confidence interval. Each region has been normalized to the highest intensity feature. The bottom traces are over the FC region and are the same as those in figure 5.8. All other regions have been fitted to a single exponential decay. The second row is over the binding energy just below the appearance of the quartet state. The third row is over the quartet state and the fourth row is just below the ground state features.

region is absent from the 279 nm data as there is not a significant enough separation between the photoelectron peaks relating to ionisation into the quartet and ground state. The fits to the $\tilde{X}$ binding energy region, shown by the solid green are the same as those described above. All the other regions were fitted to an exponential decay convolved with a Gaussian. The results of the fits are shown in table 5.3. These higher energy regions have significantly more noise than the FC region so one should be careful about how much value to put on the fits. The fits to the 279 nm data show no significant variation in the values from the fit in the three binding energy regions this shows we are not able to observe any time delay second region (teal) which is associated with long C-I distance. This is due to noise on the data set and the data point at 60 fs being surprisingly low intensity making extracting accurate fits difficult. The fits show similar time zeros and short lifetime which means they are consistent with a rapid dissociation of the C-I bond. At 243 nm we observe a time offset. Both the first (green) and third (blue)

| | 279 nm | | |
|---|---|---|---|
| Energy region/eV | Time offset ($t_0$) /fs | FWHM /fs | Lifetime ($\tau_1$) /fs |
| 4.96-6.14 | 0±7 | 87±9 | <25 |
| 7.04-7.70 | 4±13 | 74±25 | 30±17 |
| 7.78-8.33 | 6±17 | 65±25 | 30±17 |
| | 254 nm | | |
| 4.70-5.70 | 0±10 | 77±27 | 52±23 |
| 6.60-7.20 | 25±14 | 74±20 | 44±20 |
| 7.30-7.70 | 2±13 | 65±28 | 82±20 |
| 8.30-8.80 | 31±15 | 82±37 | 82±27 |
| | 243 nm | | |
| 4.55-5.38 | 0±10 | 57±29 | 46±14 |
| 5.96-6.87 | 25±13 | 74±24 | 26±19 |
| 7.04-7.47 | 13±12 | 59±15 | 20±11 |
| 8.02-8.62 | 31±9 | 56±20 | 47±13 |

**Table 5.3:** The fit parameters for the first exponential decay used to fit the different binding energies region for 279 nm, 254 nm and 243 nm to measure the shifts in time zero as the C-I bond stretches. The errors are 1 standard deviation and are calculated using bootstrapping analysis.

binding energy regions are within error of each other. We expect them to both have the same time-zero as they are both over the initial peaks and hence the signal is initiated at pump-probe overlap. Both second and fourth energy regions have a time offset as expected. The signal in these regions is associated with longer C-I distances and hence there is a delay in observed time as the C-I separates after the initial excitation from the pump wavelength. There is 27 fs of variation in the lifetime of the different binding energy, however given the large amount of error on these values there is not a significant change in lifetimes. All lifetimes are below 50 fs. The results from the fits are consistent with rapid dissociation of the C-I bond which has a slightly longer lifetime at 243 nm.

At 254 nm comparison between the three higher binding energy and FC region needs to be done carefully as different models have been used to fit the data. The fit to only one component will cause the lifetime to be significantly increased and the time offset to be earlier than with two components. Although the higher binding energy intensity traces show hints of a secondary, delayed component, particularly in the $Q$ state at

around ∼150 fs this can not be asserted with any confidence due to the limited signal on this data set. Similar to the 243 nm data we observe a similar onset time for the $\tilde{X}$ and $Q$ states and a time offset for regions 2 and 4. We also see this extended lifetime we observed for the $\tilde{X}$ state at the higher binding energy shown by the significantly longer lifetimes of ∼82 fs compared to other wavelengths. This is most clearly shown by comparing the purple region for 243 nm and 254 nm. In the 243 nm data the signal reaches a maximum at around 50 fs and then returns to baseline around 100 fs, whereas in the 254 nm the intensity similarly reaches a maximum around 50 fs but doesn't return to the baseline signal until around 200 fs.

## 5.5 Discussion

### 5.5.1 279 and 269 nm Results

There are a number of previous studies close to pump wavelengths of 266 nm that show that the $I^{\star}(^2P_{1/2})$ channel accounts for about 70% of the product [14, 9]. The appearance time of this fragment (as defined by the time the C-I bond reaches a length of 13 Bohr (6.9 Å)) in conjunction with the vibrationless $CH_3$ was recently measured to be 114 fs [19]. The ground state iodine, which accounts for about 30% of the product, has a short appearance time of 75 fs [19]. A distance of 13 Bohr was chosen as the distance when products are formed, as this is the distance when the energy of the Rydberg states no longer change with increasing C-I distances. Interestingly, the measurements also showed that the product channels associated with the vibrationally excited umbrella mode in $CH_3$ $\nu_2$ fragments have shorter appearance time than their vibrationless equivalent when produced in conjunction with the excited $I^*\left(^2P_{1/2}\right)$ co-fragment, and longer appearance times when associated with the ground $I\left(^2P_{3/2}\right)$ co-fragment. The shorter appearance times (84 fs for the $\nu_2 = 1$ channel) observed for the vibrationally excited fragments in the $I^*\left(^2P_{1/2}\right)$ channel is difficult to explain and

is at odds with the modelling performed with both 4D and 9D potential surfaces which consistently show very similar or slightly longer lifetimes for the various vibrational states covered. These timescales are consistent with our measurement. In our experiments we measured a lifetime of ∼25 fs for the wavepacket to leave the initial FC region. This gives the wavepacket 50-90 fs to travel about 4.4 Å to be consistent with the product formation experiments. If we assume the fragments are traveling at their asymptotic velocity it would take 86 fs and 113 fs to travel 4.4 Åfor I and I* respectively [22, 154]. We are not able to resolve the different product channels or the vibrational distribution because our measurements are a weighted average of all the product channels. We are also only able to extract accurate lifetimes for the start of the dissociation. This means the timescales from the two experiments are not directly comparable but they are consistent.

### 5.5.2 243 nm Pump

At 243 nm the $I^*(^2P_{1/2})$+$CH_3(\nu = 0)$ has been shown to still be the dominant product channel [14, 140]. Both I* and I were recently shown to have shorter appearance times than those measured at 266 nm at 83 fs and 53 fs respectively [19]. This is likely due to the increased kinetic energy available on dissociation however this observation appears to be contradictory with our observation of an extended, lifetime compared to the 279 nm and 269 nm results. The production formation experiments are state specific so are able to separate the formation times for the vibrationally excited products. This experiment showed that vibrationally excited products are formed at later times. The complementary 4D wavepacket calculation they also carried out showed the vibrationally excited products were formed with a higher prevalence at 243 nm than at 266 nm. The vibrationally excited product were delayed by as much as ∼80 fs relative to the vibrationless products. For example the formation time for $CH_3(\nu_2 = 1)$ in conjunction with I* and I was 133 fs and 135 fs respectively compared to 83 fs and 53 fs. This delay is significantly more than expected from their computational calculation which suggested

a delay of less than 10 fs compared to the vibrationless products.

We suggest that we measured a lifetime for the wave packet moving out of the FC geometry to be 46 fs, about 20 fs longer than the comparable lifetimes measured for 279/269 nm pump wavelength is due to the increased prevalence of vibrations product and the increased lifetimes associated with them. This highlights one of the challenges with comparing the product formation results with the TRPES results, as the TRPES provides results which a weighted average over all quantum states.

### 5.5.3 254 nm Pump

We are unaware of any time-resolved product state measurements close to 254 nm making comparisons difficult. In the work of Murillo-Sánchez *et al.*[19], it was suggested that the extended lifetime observed in the two photon ionisation photoelectron spectroscopy measurements at 255 nm could be due to accidental resonances with a higher lying electron state in the ionisation step. Our single photon measurements has ruled this suggestion out. Accidental resonances appear to have enhanced the amplitude of the longer lived state when compared to the single photon results but the long lived feature and the unusual time profile which requires a secondary exponential decay to model is still observed. We suggest the relative population of the delayed feature is about 10% compared to the first feature as opposed to the 50% suggest earlier based on the two photon ionisation results. The shift to higher binding energy as the dissociation progresses could also be followed with the higher energy probe, at higher binding energy an extended lifetime compared with the other pump lengths was also observed.

In both the single and multiphoton probe experiments the time-resolved photoelectron spectra have been fitted to two exponential decays convolved with a Gaussian with a variable time-zero. In the XUV and two photon the first decay has a lifetime of 40 fs and 52$\pm$23 fs respectively. This lifetime is similar to those measured at the other three

wavelengths (279, 269 and 243 nm). We therefore suggest the first exponential decay is modeling rapid dissociation dynamics on the $^3Q_0$ state which is also observed at all other wavelengths. The dynamics which is causing the extended lifetime is unknown but a number of suggestions have been made.

It has been suggested the extended lifetime and unusual time profile may be due to transfer of energy into vibrational products as seen in the 243 nm data. If a new region of the $^3Q_0$ potential energy surface became accessible at 254 nm where Franck-Condon overlap with the methyl cation $\tilde{X}$ state were reduced, this may explain the time-dependent modulation of the ionisation cross section observed in this measurement. However we expect to continue to observe an effect on the time profile of the FC region at 243 nm which we do not observe. From the vibrational partition function, we also expected some vibrational excitation of the room temperature ensemble of methyl iodide, with about 7% in the $\nu_3$ vibration (C-I stretch) and 1% in the $\nu_6$ vibration ($CH_3$ rock). This is close to the 10% population we suggest causes the secondary feature. This may have an effect on the observed photoelectron spectrum but why this would only be observed at 254 nm is not clear. We have also suggested the extended lifetime may be due to increased excitation into the $^1Q_1$ state followed by geometric relaxation on the $^1Q_1$ state. However again at 243 nm we would expect a greater percentage of excitation onto the $^1Q_1$ state than at 255 nm so it is not clear why we wouldn't observe this effect in the 243 nm data.

It is clear more experiments such as product formation time experiments around 254 nm are required to help understand the dynamical cause of the extended lifetime and secondary feature observed in the 254 nm photoelectron spectrum.

## 5.6 Conclusion

We have used a 22.6 eV probe in a time-resolved photoelectron spectroscopy experiment to investigate the dissociation dynamics of $CH_3I$ following excitation into the A-band. We excited at four wavelengths (279, 269, 254, 243 nm) covering the central region of the A-band absorption.

We fitted the initial features following excitation by 279, 269 and 243 to a single exponential decays with lifetimes of $<$25 fs, 23 fs and 46 fs respectively. The rapid dissociation observed at the two longer wavelengths is consistent with previous results [19, 142, 143] and the potential energy surfaces of the excited states. We suggest the longer lifetime observed at 243 nm is due to the increased prevalence of excited state fragments which have been shown to have longer appearance times than the associated vibrationless products [19].

At 254 nm we were no longer able to fit the initial feature to a single exponential decay instead we used two functions with a variable time-zero. This is the same as we used in our previous multi-photon ionisation experiment. We obtain a similar value of the fits as the previous results with lifetimes of the two features being 52 fs and $>$20 fs with a separation of 114 fs. However the intensity of this secondary feature was much weaker and we suggest only about 10% of the population caused this secondary feature.

We also follow the later term dynamics and a noticeable delay in the onset time for higher binding energy were observed for both the 254 and 243 nm data. We also observe a significant increase in the lifetime of the higher binding energy region for 254 nm compared to other wavelengths.

We have been able to rule out an effect of the probe causing this extended feature

in the 254 nm data however there are still a number of questions about the nature of the dynamics which causes this more complicated spectrum. Two suggestions have been made, either a result of dynamics on the $^1Q_1$ state or dynamics due to vibrational excitation, however neither of these explanations explains why this extended lifetime would not also be observed at 243 nm .

# Chapter 6

# Summary

The work presented in this thesis explored the use of high harmonic generation (HHG) to generate a probe for time-resolved photoelectron spectroscopy (TRPES). Two TRPES experiments were presented within this thesis, one used a UV probe while the second used an XUV probe generated by HHG. These experiments studied the chemical dynamics in methyl iodide ($CH_3I$) after excitation into the A-band.

In chapter1 the theory behind molecular dynamics was discussed along with the processes of photoexcitation and photoionisation. A review of advancements in TRPES was presented as well as some alternative experimental method used to study time-resolved gas phased chemical dynamics. The second half of the chapter looked at the theory of HHG for the generation of an XUV probe for the use in TRPES. The most common experimental geometries used for HHG from a gas source were discussed and compared.

Chapter 2 discussed the laser, beamline and equipment used to study HHG from a semi-infinite gas cell (SIGC) in our lab at Southampton. The chapter also discussed the laser, beamline and equipment used at the Artemis laser facility which was used to perform the TRPES experiments on $CH_3I$ using both XUV and UV probes. This included discussion of vacuum chambers, detection methods and data collection used for both TRPES

experiments.

Chapter 3 presented the results from the characterisation of the SIGC in our lab at Southampton. The chapter discussed the data analysis and calibration of the spectrometer. Then the calibration curves for the harmonic intensity of the 13th harmonic of 790 nm (60.8 nm,20.4 eV) where presented. The effect of the focal position of the laser, the cell gas pressure and the power of the driving laser were investigated. These variables were investigated with both one and two pieces of copper tape at the exit of the cell as this also appeared to have a significant effect on the optimisation curves. These results showed the focus position of the laser needs to be about 2 cm outside the cell suggesting the HHG is occurring in a Mach disk outside the cell. This conclusion was supported by calculations of the ADK ionisation fraction for the beam focus which showed very little ionisation 2 cm away from the focus. There was variation in the ideal conditions due to variables which could not be controlled, such as the precise alignment of the laser and size of the SIGC exit hole which is affected by the number of copper tapes at the exit hole. However, for HHG of the 13th harmonic of 790 nm a good starting position for optimisation was a cell pressure of 20 mbar and a laser power of 1.7 W. This is true for both one and two pieces of copper tape. Two pieces of copper tape keeps the exit hole small and therefore the gas pressure in the detection chamber which is beneficial hence, it is also suggested to have copper tape on both sides of the exit.

The final two chapters present TRPES experiments preformed at the Artemis laser facility to study the dissociation dynamics of the A-band of $CH_3I$. In chapter 4 we used a two-photon UV probe to ionise following excitation by a 269 nm or 255 nm photon. At 269 nm we observed photoelectron signals that were consistent with a rapid dissociation with a lifetime of 30 fs for the photoelectron peaks. At 255 nm we observed a more complex time profile with an extended lifetime and secondary feature appearing after

100 fs, along with a 0.04 eV shift to lower binding energies. We estimate the secondary feature was due to about 50% of the population of the initial feature. The cause of the extended lifetime and secondary feature is not clear however we offered several suggestions. We suggested the first feature is due to dynamics on the $^3Q_0$ surface while the secondary feature is due to dynamics on the $^1Q_1$ surface. Another suggestion is it may be due to vibrational excitation either of the initial ground state ensemble or from vibrational excitation when electronically excited to the A-band. It was also suggested that the observed extended lifetime may not be due to dynamics in the A-band of methyl iodide but actually a result of the two-photon probe step, this suggestion was ruled out by the experiment in the following chapter.

In chapter 5 presented a complementary TRPES study which used a single XUV photon probe (22.6 eV). Four pump wavelengths (279 nm, 269 nm, 254 nm, 243 nm) were used to extend the region of the A-band studied. At 279 nm and 269 nm we observed signals that were consistent with a rapid dissociation out of the Franck-Condon geometry of less the 25 fs. At 243 nm we observed an extended lifetime of 46 fs which we suggested was due to increase prevalence of excited state fragments. At 254 nm we observed a similar time profile as the previous two-photon experiments with a secondary feature after 100 fs. This experiment ruled out the possibility the previous observation of an extended lifetime for the 255 nm pump wavelength with a two-photon probe was due to the probe step and not dynamics on the A-band. The intensity of the secondary feature was reduced compared to the multiphoton experiment, this time we estimated the secondary feature was due to about 10% of the excited population.

The use of both a multi-photon probe and XUV probe shows the strengths and weakness of each experiment and demonstrates the power of combining the result as we were able to obtain more information by preforming both experiments than with each individually. The UV had higher energy resolution allowing for a shift to lower binding energies to

be observed in the 255 nm pump data. The higher signal levels from the UV probe also meant it was possible to use velocity map imaging (VMI) to record the angular distribution of the photoelectrons. However, the lower energy probe also meant it was only possible to observe the early time dynamics as the wavepacket very quickly moved out of the observation window. The XUV data showed clearly the complex dynamics were not a result of the probing step. The XUV probe also allowed the full dissociation dynamics to be observed which showed the extended lifetime at 254 nm was present throughout the dissociation process. However, the XUV results were limited by XUV flux meaning there was significantly more uncertainty in the fitted lifetimes, and it was not possible to use VMI and an electron time-of-flight spectrometer was used instead. This demonstrates the need for a high flux source of lab based XUV photons, such as the SIGC source developed in chapter 3.

# Bibliography


[1] A. H. Zewail, *Femtochemistry: atomic-scale dynamics of the chemical bond*, J. Phys. Chem. A, **104(24)**:5660, 2000.

[2] T. Suzuki, *Time-resolved photoelectron spectroscopy of non-adiabatic electronic dynamics in gas and liquid phases Time-resolved photoelectron spectroscopy of non-adiabatic electronic dynamics in gas and liquid phases*, Int. Rev. Phys. Chem., **31(2)**:265, 2012.

[3] A. Stolow, A. E. Bragg, D. M. Neumark, *Femtosecond time-resolved photoelectron spectroscopy*, Chem. Rev., **104(4)**:1719, 2004.

[4] B. Eyheraguibel, A. ter Halle, C. Richard, *Photodegradation of bentazon, clopyralid, and triclopyr on model leaves: Importance of a systematic evaluation of pesticide photostability on crops*, J. Agri. Food Chem., **57(5)**:1960, 2009.

[5] M. Mansour, E. Feicht, A. Behechti, *et al.*, *Determination photostability of selected agrochemicals in water and soil*, Chemosphere, **39(4)**:575, 1999.

[6] N. d.N. Rodrigues, N. C. Cole-Filipiak, M. A. Turner, *et al.*, *Substituent position effects on sunscreen photodynamics: A closer look at methyl anthranilate*, Chem. Phys., **515**:596, 2018.

[7] E. L. Holt, V. G. Stavros, *Applications of ultrafast spectroscopy to sunscreen development, from first principles to complex mixtures*, Int. Rev. Phys. Chem., **38(2)**:243, 2019.

[8] R. Pearson, F. J. Lovas, *Microwave spectrum and molecular structure of methylenimine ($ch_2nh$)*, J. Chem. Phys., **66(9)**:4149, 1977.

[9] A. B. Alekseyev, H.-P. Liebermann, R. J. Buenker, *An ab initio study of the $CH_3I$ photodissociation. II. Transition moments and vibrational state control of the $I^*$ quantum yields*, J. Chem. Phys., **126(23)**:234103, 2007.

[10] A. M. Gardner, W. D. Tuttle, P. Groner, *et al.*, *Molecular symmetry group analysis of the low-wavenumber torsions and vibration-torsions in the s1 state and ground state cation of p-xylene: An investigation using resonance-enhanced multiphoton ionization (rempi) and zero-kinetic-energy (zeke) spectroscopy*, J. Chem. Phys., **146(12)**:124308, 2017.

[11] T. Horio, R. Spesyvtsev, T. Suzuki, *Simultaneous generation of sub-20 fs deep and vacuum ultraviolet pulses in a single filamentation cell and application to time-resolved photoelectron imaging*, Opt. Express, **21(19)**:22423, 2013.

[12] E. M. Warne, B. Downes-Ward, J. Woodhouse, *et al.*, *Photodissociation dynamics of $CH_3I$ probed via multiphoton ionisation photoelectron spectroscopy*, Physical Chemistry Chemical Physics, **21(21)**:11142, 2019.

[13] H. Miyasaka, K. Morita, K. Kamada, *et al.*, *Femtosecond-picosecond laser photolysis studies on photoreduction process of excited benzophenone with n,n-dimethylaniline in acetonitrile solution*, Bull. Chem. Soc. Jpn., **63(12)**:3385, 1990.

[14] A. T. J. B. Eppink, D. H. Parker, *Methyl iodide A-band decomposition study by photofragment velocity imaging*, J. Chem. Phys., **109(12)**:4758, 1998.

[15] R. Bruckmeier, C. Wunderlich, H. Figger, *New experimental insight into the ground state potential surface of triatomic hydrogen*, Phys. Rev. Lett., **72(16)**:2550, 1994.

[16] K. Lehamann, G. scoles, B. Pate, *Intramolecular Dynamics from Eigenstate-Resolved Infrared Spectra*, Annu. Rev. Phys. Chem., **45(1)**:241, 1994.

[17] A. D. Smith, H. M. Watts, E. Jager, *et al.*, *Resonant multiphoton ionisation probe of the photodissociation dynamics of ammonia*, Physical Chemistry Chemical Physics, **18(40)**:28150, 2016.

[18] H. Yong, X. Xu, J. M. Ruddock, *et al.*, *Ultrafast X-ray scattering offers a structural view of excited-state charge transfer*, Proceedings of the National Academy of Sciences, **118(19)**, 2021, URL `https://www.pnas.org/content/118/19/e2021714118`.

[19] M. L. Murillo-sánchez, J. González-vázquez, M. E. Corrales, *et al.*, *Femtochemistry under scrutiny : Clocking state-resolved channels in the photodissociation of $CH_3$ I in the A -band Femtochemistry under scrutiny : Clocking state-resolved channels in the photodissociation of $CH_3I$ in the A -band*, J. Chem. Phys., **152**:014304, 2020.

[20] H.-Y. Chen, I.-R. Lee, P.-Y. Cheng, *Gas-phase femtosecond transient absorption spectroscopy*, Rev. Sci. Instr., **77(7)**:076105, 2006.

[21] A. Sharonov, T. Gustavsson, V. Carré, *et al.*, *Cytosine excited state dynamics studied by femtosecond fluorescence upconversion and transient absorption spectroscopy*, Chem. Phys. Lett., **380(1)**:173, 2003.

[22] F. Allum, M. Burt, K. Amini, *et al.*, *Coulomb explosion imaging of $CH_3I$ and $CH_2ClI$ photodissociation dynamics*, J. Chem. Phys., **149(20)**:204313, 2018.

[23] J. Yang, M. Guehr, T. Vecchione, *et al.*, *Femtosecond gas phase electron diffraction with MeV electrons*, Faraday Discuss., **194**:563, 2016.

[24] M. R. Ware, J. M. Glownia, N. Al-Sayyad, *et al.*, *Characterizing dissociative motion in time-resolved x-ray scattering from gas-phase diatomic molecules*, Phys. Rev. A, **100**:033413, 2019.

[25] R. Berera, R. van Grondelle, J. T. Kennis, *Ultrafast transient absorption spectroscopy: Principles and application to photosynthetic systems*, Photosynth. Res., **101**:105, 2009.

[26] B. Doppagne, T. Neuman, R. Soria-Martinez, *et al.*, *Single-molecule tautomerization tracking through space- and time-resolved fluorescence spectroscopy*, Nat. Nanotechnol., **15(3)**:207, 2020.

[27] C. Gooijer, F. Ariese, N. Velthorst, *Fluorescence — high-resolution techniques*, in P. Worsfold, A. Townshend, C. Poole (Editors), *Encyclopedia of Analytical Science (Second Edition)*, (119–128), Elsevier, Oxford, second edition edition, 2005.

[28] J. Yang, X. Zhu, T. J. A. Wolf, *et al.*, *Imaging $CF_3I$ conical intersection and photodissociation dynamics with ultrafast electron diffraction*, Science, **361(6397)**:64, 2018.

[29] Y. Liu, S. L. Horton, J. Yang, *et al.*, *Spectroscopic and Structural Probing of Excited-State Molecular Dynamics with Time-Resolved Photoelectron Spectroscopy and Ultrafast Electron Diffraction*, Phys. Rev. X, **10**:021016, 2020.

[30] J. Kim, K. H. Kim, J. H. Lee, *et al.*, *Ultrafast X-ray diffraction in liquid, solution and gas: present status and future prospects*, Acta Crystallographica Section A, **66(2)**:270, 2010.

[31] F. Temps, `https://www.temps.phc.uni-kiel.de/en`, accessed: 15-05-19.

[32] P. Atkins, J. de Paula, R. Friedman, *Physical chemistry: quanta, matter and change*, oxford university press, 2009.

[33] D. R. Yarkony, *Conical Intersections: Their Description and Consequences*, chapter 2, (41–127), World Scientific Publishing Co. Pte. Ltd, 2004.

[34] A. L. Sobolewski, W. Domcke, *The chemical physics of the photostability of life*, Europhysics News, **37(4)**:20, 2008.

[35] A. D. Smith, E. M. Warne, D. Bellshaw, *et al.*, *Mapping the Complete Reaction Path of a Complex Photochemical Reaction*, Phys. Rev. Lett., **120(18)**:183003, 2018.

[36] R. T. Williams, T. R. Royt, J. C. Rife, *et al.*, *Picosecond time-resolved photoelectron spectroscopy of ZnTe*, J. Vac. Sci. Technol., **21(2)**:509, 1982.

[37] J. B. Pallix, S. D. Colson, *Time-resolved photoelectron studies of the relaxation of the $S_1(^1E'')$ excited state of sym-triazine*, Chem. Phys. Lett., **119(1)**:38 , 1985.

[38] D. Felsmann, K. Moshammer, J. Krüger, *et al.*, *Electron ionization, photoionization and photoelectron/photoion coincidence spectroscopy in mass-spectrometric investigations of a low-pressure ethylene/oxygen flame*, Proceedings of the Combustion Institute, **35(1)**:779, 2015.

[39] J. A. Davies, J. E. LeClaire, R. E. Continetti, *et al.*, *Femtosecond time-resolved photoelectron–photoion coincidence imaging studies of dissociation dynamics*, J. Chem. Phys., **111(1)**:1, 1999.

[40] P. Maierhofer, M. Bainschab, B. Thaler, *et al.*, *Disentangling multichannel photodissociation dynamics in acetone by time-resolved photoelectron–photoion coincidence spectroscopy*, J. Phys. Chem., **120(32)**:6418, 2016.

[41] A. E. Boguslavskiy, O. Schalk, N. Gador, *et al.*, *Excited state non-adiabatic dynamics of the smallest polyene, trans 1,3-butadiene. i. time-resolved photoelectron-photoion coincidence spectroscopy*, J. Chem. Phys., **148(16)**:164302, 2018.

[42] I. Wilkinson, A. E. Boguslavskiy, J. Mikosch, *et al.*, *Excited state dynamics in $so_2$. i. bound state relaxation studied by time-resolved photoelectron-photoion coincidence spectroscopy*, J. Chem. Phys., **140(20)**:204301, 2014.

[43] P. Hockett, E. Ripani, A. Rytwinski, *et al.*, *Probing ultrafast dynamics with time-resolved multi-dimensional coincidence imaging: butadiene*, J. Mod. Opt., **60(17)**:1409, 2013.

[44] M. Tsubouchi, B. J. Whitaker, L. Wang, *et al.*, *Photoelectron Imaging on Time-Dependent Molecular Alignment Created by a Femtosecond Laser Pulse*, Phys. Rev. Lett., **86**:4500, 2001.

[45] A. E. Bragg, R. Wester, A. V. Davis, *et al.*, *Excited-state detachment dynamics and rotational coherences of $C_2^-$ via time-resolved photoelectron imaging*, Chem. Phys. Lett., **376(5)**:767, 2003.

[46] J. Lecointre, G. M. Roberts, D. A. Horke, *et al.*, *Ultrafast relaxation dynamics observed through time-resolved photoelectron angular distributions*, J. Phys. Chem. A., **114(42)**:11216, 2010.

[47] C. Z. Bisgaard, O. J. Clarkin, W. Guorong, *et al.*, *Time-Resolved Molecular Frame Dynamics of Fixed-in-Space $CS_2$ Molecules*, Science, **314(5797)**:278, 2006.

[48] J. L. Hansen, H. Stapelfeldt, D. Dimitrovski, *et al.*, *Time-Resolved Photoelectron Angular Distributions from Strong-Field Ionization of Rotating Naphthalene Molecules*, Phys. Rev. Lett., **106**:073001, 2011.

[49] N. J. Turro, M. B. Zimmt, I. R. Gould, *et al.*, *Triplet energy transfer as a probe of surface diffusion rates: time-resolved diffuse reflectance transient absorption spectroscopy study*, J. Am. Chem. Soc., **107(20)**:5826, 1985.

[50] C. Schriever, S. Lochbrunner, E. Riedle, *et al.*, *Ultrasensitive ultraviolet-visible 20fs absorption spectroscopy of low vapor pressure molecules in the gas phase*, Rev. Sci. Instrum., **79(1)**:013107, 2008.

[51] A. H. Zewail, *"femtosecond transition-state dynamics"*, Faraday Discuss. Chem. Soc., **91**:207, 1991.

[52] M. J. Rosker, M. Dantus, A. H. Zewail, *Femtosecond real-time probing of reactions. I. The technique*, J. Chem. Phys., **89(10)**:6113, 1988.

[53] T. D. Green, K. L. Knappenberger, *Relaxation dynamics of au25l18 nanoclusters studied by femtosecond time-resolved near infrared transient absorption spectroscopy*, Nanoscale, **4**:4111, 2012.

[54] M. Raytchev, E. Pandurski, I. Buchvarov, *et al.*, *Bichromophoric interactions and time-dependent excited state mixing in pyrene derivatives. a femtosecond broadband pump-probe study*, J. Phys. Chem., **107(23)**:4592, 2003.

[55] A. Bhattacherjee, S. R. Leone, *Ultrafast X-ray Transient Absorption Spectroscopy of Gas-Phase Photochemical Reactions: A New Universal Probe of Photoinduced Molecular Dynamics*, Acc. Chem. Res., **51(12)**:3203, 2018.

[56] Y. Pertot, C. Schmidt, M. Matthews, *et al.*, *Time-resolved x-ray absorption spectroscopy with a water window high-harmonic source*, Science, **355(6322)**:264, 2017.

[57] Z.-H. Loh, *Studies of Ultrafast Molecular Dynamics by Femtosecond Extreme Ultraviolet Absorption Spectroscopy*, Chem. Lett., **50(5)**:965, 2021.

[58] Z. VAager, R. Naaman, E. P. Kanter, *Coulomb Explosion Imaging of Small Molecules*, Science, **244(4903)**:426, 1989.

[59] M. Pitzer, M. Kunitski, A. S. Johnson, *et al.*, *Direct Determination of Absolute Molecular Stereochemistry in Gas Phase by Coulomb Explosion Imaging*, Science, **341(6150)**:1096, 2013.

[60] Slater, Craig S. and Blake, Sophie and Brouard, Mark and Lauer, Alexandra and Vallance, Claire and Bohun, C. Sean and Christensen, Lauge and Nielsen, Jens H. and Johansson, Mikael P. and Stapelfeldt, Henrik, *Coulomb-explosion imaging using a pixel-imaging mass-spectrometry camera*, Phys. Rev. A, **91**:053424, 2015.

[61] T. Yatsuhashi, N. Nakashima, *Multiple ionization and coulomb explosion of molecules, molecular complexes, clusters and solid surfaces*, J. of Photochem. Photobiol. C, **34**:52, 2018.

[62] K. Amini, E. Savelyev, F. Braußе, *et al.*, *Photodissociation of aligned ch3i and c6h3f2i molecules probed with time-resolved coulomb explosion imaging by site-selective extreme ultraviolet ionization*, Structural Dynamics, **5(1)**:014301, 2018.

[63] A. Matsuda, M. Fushitani, E. J. Takahashi, *et al.*, *Visualizing hydrogen atoms migrating in acetylene dication by time-resolved three-body and four-body Coulomb explosion imaging*, Phys. Chem. Chem. Phys., **13**:8697, 2011.

[64] J. Kim, K. H. Kim, J. H. Lee, *et al.*, *Ultrafast X-ray diffraction in liquid, solution and gas: present status and future prospects*, Acta Crystallogr A, **66(2)**:270, 2010.

[65] Shen X, Nunes JPF, Yang J, Jobe RK, Li RK, Lin MF, Moore B, Niebuhr M, Weathersby SP, Wolf TJA, Yoneda C, Guehr M, Centurion M, Wang XJ., *Femtosecond gas-phase mega-electron-volt ultrafast electron diffraction*, Struct Dyn., **6**:054305, 2019.

[66] H. Ihee, V. A. Lobastov, U. M. Gomez, *et al.*, *Direct Imaging of Transient Molecular Structures with Ultrafast Diffraction*, Science, **291(5503)**:458, 2001.

[67] E. C. Snively, M. A. K. Othman, M. Kozina, *et al.*, *Femtosecond compression dynamics and timing jitter suppression in a thz-driven electron bunch compressor*, Phys. Rev. Lett., **124**:054801, 2020.

[68] L. Zhao, J. Wu, Z. Wang, *et al.*, *Noninvasive time-sorting in radio frequency-compressed ultrafast electron diffraction*, Struct. Dyna., **8(4)**:044303, 2021.

[69] H. Ihee, B. M. Goodson, R. Srinivasan, *et al.*, *Ultrafast Electron Diffraction and Structural Dynamics: Transient Intermediates in the Elimination Reaction of $C_2F_4I_2$*, J. Phys. Chem. A, **106(16)**:4087, 2002.

[70] H. Yong, A. Moreno Carrascosa, L. Ma, *et al.*, *Determination of excited state molecular structures from time-resolved gas-phase x-ray scattering*, Faraday Discuss., **228**:104, 2021.

[71] B. Stankus, H. Yong, N. Zotev, *et al.*, *Ultrafast x-ray scattering reveals vibrational coherence following rydberg excitation*, Nat. Chem., **11**:716, 2019.

[72] J. M. Glownia, A. Natan, J. P. Cryan, *et al.*, *Self-referenced coherent diffraction x-ray movie of ångstrom- and femtosecond-scale atomic motion*, Phys. Rev. Lett., **117**:153003, 2016.

[73] P. B. Corkum, *Plasma Perspective on Strong-Field Multiphoton Ionization*, Phys. Rev. Lett., **71(13)**:1994, 1993.

[74] M. Lewenstein, P. Balcou, M. Y. Ivanov, *et al.*, *Theory of high-harmonic generation by low-frequency laser fields*, Phys. Rev. A, **49(3)**:2117, 1994.

[75] M. V. Ammosov, N. . Delone, V. P. Krainov, *Tunnel ionization of complex atoms and of atomic ions in an alternating electromagnetic field*, Sov. Phys. JETP, **91(6)**:1191, 1986.

[76] B. H Bransden, C. Joachain, *Physics of Atoms and Molecules*, Prentice Hall, 2nd edition, 2014.

[77] A. D. Smith, *High Energy and High Intensity Probes of Chemical Dynamics*, Ph.D. thesis, University of Southampton, 2017.

[78] G. L. Yudin, M. Y. Ivanov, *Nonadiabatic tunnel ionization: Looking inside a laser cycle*, Phys. Rev. A, **64**:013409, 2001.

[79] D. T. Lloyd, K. O'Keeffe, S. M. Hooker, *Comparison of strong-field ionization models in the wavelength-scaling of high harmonic generation*, Opt. Express, **27(5)**:6925, 2019.

[80] F. A. Ilkov, J. E. Decker, S. L. Chin, *Ionization of atoms in the tunnelling regime with experimental evidence using hg atoms*, J. Phys. B, **25(19)**:4005, 1992.

[81] P. B. Corkum, N. H. Burnett, F. Brunel, *Above-threshold ionization in the long-wavelength limit*, Phys. Rev. Lett., **62**:1259, 1989.

[82] F. Morales, P. Rivière, M. Richter, *et al.*, *High harmonic spectroscopy of electron localization in the hydrogen molecular ion*, J. Phys. B, **47(20)**:204015, 2014.

[83] R. T. Chapman, *Building a Laboratory based XUV Microscope*, Ph.D. thesis, University of Southampton, 2012.

[84] C. V. Vuong, K. B. Dinh, P. Hannaford, *et al.*, *Influence of absorption on phase-matched generation of coherent extreme ultraviolet radiation in a long interaction geometry*, Optik, **127(5)**:2874 , 2016.

[85] P. Balcou, P. Sali'eres, A. L'Huillier, *et al.*, *Generalized phase-matching conditions for high harmonics: The role of field-gradient forces*, Phys. Rev. A, **55(4)**:3204, 1997.

[86] B. K. Dinh, *Phase-Matched High Order Harmonic Generation and Applications*, Ph.D. thesis, Swinburne University of Technology, 2012.

[87] P. Salières, A. L'Huillier, M. Lewenstein, *Coherence Control of High-Order Harmonics*, Phys. Rev. Lett., **74(19)**:3776, 1995.

[88] E. Constant, D. Garzella, P. Breger, *et al.*, *Optimizing High Harmonic Generation in Absorbing Gases: Model and Experiment*, Phys. rev. lett., **82(8)**:1668, 1999.

[89] B. Henke, E. Gullikson, J. Davis, *X-ray interactions: Photoabsorption, scattering, transmission, and reflection at e = 50-30,000 ev, z = 1-92*, At. Data Nucl. Data Tables, **54(2)**:181, 1993.

[90] K. Schiessl, K. L. Ishikawa, E. Persson, *et al.*, *Wavelength dependence of high-harmonic generation from ultrashort pulses*, J. Mod. Opti., **55(16)**:2617, 2008.

[91] A. D. Shiner, C. Trallero-Herrero, N. Kajumba, *et al.*, *Wavelength Scaling of High Harmonic Generation Efficiency*, Phys. Rev. Lett., **103**:073902, 2009.

[92] E. L. Falcão-Filho, C.-J. Lai, K.-H. Hong, *et al.*, *Scaling of high-order harmonic efficiencies with visible wavelength drivers: A route to efficient extreme ultraviolet sources*, Applied Physics Letters, **97(6)**:061107, 2010.

[93] M. Ferray, A. L'Huillier, X. F. Li, *et al.*, *Multiple-harmonic conversion of 1064 nm radiation in rare gases*, J. Phys. B, **21(3)**:L31, 1988.

[94] S. Ghimire, A. D. Dichiara, E. Sistrunk, *et al.*, *Observation of high-order harmonic generation in a bulk crystal*, Nat. Phys., **7(2)**:138, 2011.

[95] S. Ghimire, D. A. Reis, *High-harmonic generation from solids*, Nat. Phys., **15(1)**:10, 2019.

[96] T. T. Luu, Z. Yin, A. Jain, *et al.*, *Extreme–ultraviolet high–harmonic generation in liquids*, Nat. Commun., **9(1)**:1, 2018.

[97] A. Flettner, T. Pfeifer, D. Walter, *et al.*, *High-harmonic generation and plasma radiation from water microdroplets*, Appl. Phys. B, **77(8)**:747, 2003.

[98] R. A. Ganeev, *Strong field-induced frequency conversion of laser radiation in plasma plumes: Recent achievements*, Sci. World J., **2013**, 2013.

[99] NIST, *NIST Chemistry WebBook*, `https://webbook.nist.gov/cgi/inchi?ID=C7440371&Mask=20`, accessed: June 2021.

[100] C. Altucci, R. Velotta, J. P. Marangos, *et al.*, *Dependence upon the molecular and atomic ground state of higher-order harmonic generation in the few-optical-cycle regime*, Phys. Rev. A, **71(1)**, 2005.

[101] B. Shan, X.-M. Tong, Z. Zhao, *et al.*, *High-order harmonic cutoff extension of the $O_2$ molecule due to ionization suppression*, Phys. Rev. A, **66**:061401, 2002.

[102] S. L. Stebbings, E. T. F. Rogers, A. M. de Paula, *et al.*, *Molecular variation of capillary-produced soft x-ray high harmonics*, J. Phys. B, **41(14)**:145602, 2008.

[103] J. Brichta, M. C. H. Wong, J. B. Bertrand, *et al.*, *Comparison and real-time monitoring of high-order harmonic generation in different sources*, Phys. Rev. A, **79(3)**:033404, 2009.

[104] D. S. Steingrube, T. Vockerodt, E. Schulz, *et al.*, *Phase matching of high-order harmonics in a semi-infinite gas cell*, Phys. Rev. A, **80(4)**:1, 2009.

[105] R. Schoenlein, T. Elsaesser, K. Holldack, *et al.*, *Recent advances in ultrafast X-ray sources*, Philos. Trans. R. Soc. A, **377(2145)**:20180384, 2019.

[106] L. Nugent-Glandorf, M. Scheer, D. Samuels, *et al.*, *Ultrafast Time-Resolved Soft X-Ray Photoelectron Spectroscopy of Dissociating $Br_2$*, Phys. Rev. Lett., **87(19)**, 2001.

[107] P. Wernet, M. Odelius, K. Godehusen, *et al.*, *Real-Time Evolution of the Valence Electronic Structure in a Dissociating Molecule*, Phys. Rev. Lett., **103**:013001, 2009.

[108] S.-H. Lee, K.-C. Tang, I.-C. Chen, *et al.*, *Substituent Effects in Molecular Electronic Relaxation Dynamics via Time-Resolved Photoelectron Spectroscopy: $\pi\pi^*$ States in Benzenes*, J. Phys. Chem. A, **106(39)**:8979, 2002.

[109] S. Ullrich, T. Schultz, M. Z. Zgierski, *et al.*, *Direct Observation of Electronic Relaxation Dynamics in Adenine via Time-Resolved Photoelectron Spectroscopy*, J. Am. Chem. Soc., **126(8)**:2262, 2004.

[110] A. Makida, H. Igarashi, T. Fujiwara, *et al.*, *Ultrafast Relaxation Dynamics in trans-1,3-Butadiene Studied by Time-Resolved Photoelectron Spectroscopy with High Harmonic Pulses*, J. Phys. Chem. Lett., **5(10)**:1760, 2014.

[111] S. Adachi, M. Sato, T. Suzuki, *Direct Observation of Ground-State Product Formation in a 1,3-Cyclohexadiene Ring-Opening Reaction*, J. Phys. Chem. Lett., **6(3)**:343, 2015.

[112] R. Iikubo, T. Sekikawa, Y. Harabuchi, *et al.*, *Structural dynamics of photochemical reactions probed by time-resolved photoelectron spectroscopy using high harmonic pulses*, Faraday Discuss., **194**:147, 2016.

[113] T. Geng, J. Ehrmaier, O. Schalk, *et al.*, *Time-Resolved Photoelectron Spectroscopy Studies of Isoxazole and Oxazole*, J. Phys. Chem. A, **124(20)**:3984, 2020.

[114] *Ultrashort Sources I: Fundamentals*, in J.-C. Diels, W. Rudolph (Editors), *Ultrashort Laser Pulse Phenomena (Second Edition)*, chapter 5, (277 – 339), Academic Press, Burlington, second edition edition, 2006.

[115] W. Zhang, W. Kong, G. Wang, *et al.*, *Review of pulse compression gratings for chirped pulse amplification system*, Opt. Eng., **60(2)**:1 , 2021.

[116] J. E. Harvey, R. N. Pfisterer, *Understanding diffraction grating behavior: including conical diffraction and Rayleigh anomalies from transmission gratings*, Opt. Eng., **58(8)**:1 , 2019.

[117] E. M. Warne, *Measuring Molecular Dynamics Using UV and XUV Photoelectron Spectroscopy*, Ph.D. thesis, University of Southampton, 2020.

[118] P. Rudawski, C. M. Heyl, F. Brizuela, *et al.*, *A high-flux high-order harmonic source*, Rev. Sci. Instr., **84(7)**:073103, 2013.

[119] *TOPAS Optical Parametric Amplifiers for Ti:Sapphire Lasers*.

[120] A. T. J. B. Eppink, D. H. Parker, *Velocity map imaging of ions and electrons using electrostatic lenses: Application in photoelectron and photofragment ion imaging of molecular oxygen*, Rev. Sci. Instrum., **68(9)**:3477, 1997.

[121] B. Henke, `http://henke.lbl.gov/optical_constants/`, accessed: 15-05-19.

[122] A. Börzsönyi, Z. Heiner, A. Kovács, *et al.*, *Measurement of pressure dependent nonlinear refractive index of inert gases*, Opt. Express, **18(25)**:25847, 2010.

[123] S. Zahedpour, J. K. Wahlstrand, H. M. Milchberg, *Measurement of the nonlinear refractive index of air constituents at mid-infrared wavelengths*, Opt. Lett., **40(24)**:5794, 2015.

[124] J. A. Grant-Jacob, *Table-top XUV Nanoscope*, Ph.D. thesis, University of Southampton, 2011.

[125] H. Ashkenas, F. S. Sherman, *The Structure and Utilization of Supersonic Free Jets in Low Density Wind Tunnels*, (84), 1965.

[126] K. Kuchitsu (Editor), *Structure of Free Polyatomic Molecules*, Springer, 1998.

[127] A. B. Alekseyev, H.-P. Liebermann, R. J. Buenker, *et al.*, *An ab initio study of the $CH_3I$ photodissociation. I. Potential energy surfaces*, J. Chem. Phys., **126(23)**:234102, 2007.

[128] S. Marggi Poullain, D. V. Chicharro, J. González-Vázquez, *et al.*, *A velocity map imaging study of the photodissociation of the methyl iodide cation*, Phys. Chem. Chem. Phys., **19**:7886, 2017.

[129] R. De Nalda, J. Durá, A. García-Vela, *et al.*, *A detailed experimental and theoretical study of the femtosecond -band photodissociation of $CH_3I$*, J. Chem. Physics, **128(24)**:244309, 2008.

[130] R. S. Mulliken, *Intensities in Molecular Electronic Spectra X. Calculations on Mixed-Halogen, Hydrogen Halide, Alkyl Halide, and Hydroxyl*, J. Chem. Phys, **8(5)**:382, 1940.

[131] A. T. J. B. Eppink, D. H. Parker, *Energy partitioning following photodissociation of methyl iodide in the A band: A velocity mapping study*, J. Chem. Phys., **110(2)**:832, 1999.

[132] L. Rubio-Lago, A. García-Vela, A. Arregui, *et al.*, *The photodissociation of $CH_3I$ in the red edge of the A-band: Comparison between slice imaging experiments and multisurface wave packet calculations*, J. Chem. Phys., **131(17)**:174309, 2009.

[133] M. G. González, J. D. Rodríguez, L. Rubio-Lago, *et al.*, *Slice imaging and wave packet study of the photodissociation of $CH_3I$ in the blue edge of the A-band: evidence of reverse $^3Q_0 \leftarrow {}^1Q_1$ non-adiabatic dynamics*, Phys. Chem. Chem. Phys., **13**:16404 , 2011.

[134] L. G. Karpov, A. M. Pravilov, F. I. Vilesov, *Processes of photodissociation of free alkyl iodide molecules by 254 nm radiation*, Sov. J. Quantum Electron., **7(4)**:457, 1977.

[135] T. F. Hunter, K. S. Kristjansson, *Photoacoustic Measurements of Photofragmententation in $CH_3I$*, Chem. Phys. Lett., **58(2)**:291, 1978.

[136] W. P. Hess, S. J. Kohler, H. K. Haugen, *et al.*, *Application of an InGaAsP diode laser to probe photodissociation dynamics: I* quantum yields from n- and i-$C_3F_7I$ and $CH_3I$ by laser gain vs absorption spectroscopy*, J. Chem. Phys., **84(4)**:2143, 1986.

[137] A. Fahr, A. K. Nayak, M. J. Kurylo, *The ultraviolet absorption cross sections of $CH_3I$ temperature dependent gas and liquid phase measurements*, Chemical Physics, **197(2)**:195, 1995.

[138] R. Ogorzalek Loo, H. Haerri, G. E. Hall, *et al.*, *Methyl rotation, vibration, and alignment from a multiphoton ionization study of the 266 nm photodissociation of methyl iodide*, J. Chem. Phys., **90(8)**:4222, 1989.

[139] S. L. Baughcum, S. R. Leone, *Photofragmentation infrared emission studies of vibrationally excited free radicals $CH_3$ and $CH_2I$*, J. Chem. Phys., **72(12)**:6531, 1980.

[140] G. Van Veen, T. Baller, A. De Vries, *et al.*, *The excitation of the umbrella mode of $CH_3$ and $CD_3$ formed from photodissociation of $CH_3I$ and $CD_3I$ at 248 nm*, Chem. Phys., **87(3)**:405 , 1984.

[141] M. Barry, P. Gorry, *Photofragmentation dynamics of $CH_3I$ at 248 nm*, Mol. Phys., **52(2)**:461, 1984.

[142] M. E. Corrales, V. Loriot, G. Balerdi, *et al.*, *Structural dynamics effects on the ultrafast chemical bond cleavage of a photodissociation reaction*, Phys. Chem. Chem. Phys., **16(19)**:8812, 2014.

[143] A. García-vela, R. de Nalda, J. Durá, *et al.*, *A 4D wave packet study of the $CH_3I$ photodissociation in the A-band. Comparison with femtosecond velocity map imaging experiments*, J. Chem. Phys., **135(15)**:154306, 2011.

[144] A. Gedanken, M. D. Rowe, *Magnetic circular dichroism spectra of the methyl halides. Resolution of the n→ $\sigma^*$ continuum*, Chem. Phys. Lett., **34(1)**:39 , 1975.

[145] Natan, *Mathworks-PolarOnionPeeling*, `https://uk.mathworks.com/matlabcentral/fileexchange/41064-polaronionpeeling`, accessed: May 2018.

[146] G. M. Roberts, J. L. Nixon, J. Lecointre, *et al.*, *Toward real-time charged-particle image reconstruction using polar onion-peeling*, Rev. Sci. Instrum., **80(5)**, 2009.

[147] D. Turner, *Molecular Photoelectron Spectroscopy*, John Wiley and Sons, 1970.

[148] NIST, *NIST Chemistry WebBook*, `https://webbook.nist.gov/cgi/cbook.cgi?ID=C12538726&Mask=800#Electronic-Spec`, accessed: June 2021.

[149] M. E. Corrales, J. González-Vázquez, R. De Nalda, *et al.*, *Coulomb Explosion Imaging for the Visualization of a Conical Intersection*, J. Phys. Chem. Lett., **10(2)**:138, 2019.

[150] S. Eden, P. Limão-Vieira, S. V. Hoffmann, *et al.*, *VUV spectroscopy of $CH_3Cl$ and $CH_3I$*, Chem. Phys., **331(2-3)**:232, 2007.

[151] B. Downes-Ward, J. Warne, Emily M.and Woodhouse, M. A. Parkes, *et al.*, *Photodissociation dynamics of methyl iodide across the A-band probed by femtosecond extreme ultraviolet photoelectron spectroscopy*, J. Phys. B, **54(13)**:134003, 2021.

[152] E. M. Warne, B. Downes-Ward, J. Woodhouse, *et al.*, *Photodissociation dynamics of methyl iodide probed using femtosecond extreme ultraviolet photoelectron spectroscopy*, Phys. chem. chem. phys., **22(44)**:25695, 2020.

[153] S. Marggi Poullain, D. V. Chicharro, J. Gonzalez-Vazquez, *et al.*, *A velocity map imaging study of the photodissociation of the methyl iodide cation*, Phys. Chem. Chem. Phys., **19**:7886, 2017.

[154] A. T. J. B. Eppink, D. H. Parker, *Energy partitioning following photodissociation of methyl iodide in the A band: A velocity mapping study*, J. Chem. Phys., **110(2)**:832, 1999.